ELECTRONIC STRUCTURE OF QUASICRYSTALS STUDIED BY PHOTOEMISSION SPECTROSCOPY

by
Guowei Zhang

Thesis submitted to
the School of Graduate Studies and Research in
partial fulfillment of the requirements for
the degree of Ph.D. in physics

Department of Physics
University of Ottawa
Ottawa, Ontario
Canada

September 1995

ISBN 0-612-15780-6

Canada

UNIVERSITÉ D'OTTAWA
UNIVERSITY OF OTTAWA

ABSTRACT

To investigate the electronic structure of the high-quality quasicrystals, photoemission spectroscopy measurements have been carried out using synchrotron radiation source in the photon-energy range 35-150 eV. The studied quasicrystals are icosahedral $Al_{70}Pd_{20}Mn_{10}$, $Al_{65}Cu_{20}Os_{15}$, and $Al_{65}Cu_{20}Ru_{15}$, and decagonal $Al_{65}Co_{15}Cu_{20}$ and $Al_{70}Co_{15}Ni_{15}$. Resonance photoemission near the transition from the shallow core levels to the *d* valence bands has been employed to show that the feature close to the Fermi level in the valence bands is predominantly due to the *d* electron states in the nearly-half-full subshells (Mn, Fe, Ru, Os). The feature farther from the Fermi level has been identified as being mainly due to the *d* electron states in the full *d* subshells (Pd, Cu). In some cases, the experimental partial densities of states have been obtained by taking advantage of the synchrotron-radiation-based photoemission technique and the large changes in the cross sections. The as-measured valence-band spectra were corrected for the experimental parameters and the background in order to make a meaningful comparison between the spectra. The high energy-resolution ultraviolet photoelectron spectroscopy measurements on icosahedral $Al_{65}Cu_{20}Fe_{7.5}Ru_{7.5}$ prove that there is a pseudogap from the *d* electrons close to the Fermi level. The studied samples were characterized by the X-ray diffraction and the diffraction patterns were indexed based on several indexing schemes. A description of the indexing procedures is presented. The experimental results of this work are related to the theoretical predictions of a pseudogap and spikiness in the density of states. The unusual behavior of the resistivity of the quasicrystals is interpreted in terms of disorder and other relevant theories.

ACKNOWLEDGMENTS

I would like to extend my sincere gratitude to Dr. Z.M. Stadnik, my research supervisor, for providing me the unique study opportunity, for his helpful and patient guidance, and for understanding and encouragement during the course of this work.

I wish to thank Dr. Béla Joós and Mr. Mike Jackson for their understanding and great help with various matters of the study life. I am grateful to Dr. C. Benson, Bei Wah Chan, Hélène Lacasse, and Roger Chagnon for their assistance with the first-year labs. Thanks are extented to the workshops for their cooperations, and to all in the department for their help on countless occasions.

May I also take this opportunity to acknowledge the financial support of the University of Ottawa in the form of Tuition Fee Wavers and Scholarships.

I am thankful to Profs. A.-P. Tsai and A. Inoue of Tohoku University (Japan) for providing me the high-quality samples and thankful to Dr. M.-L Shek of the Brookhaven National Laboratory (USA) for her great assistance in the course of the photoemission spectroscopy measurements.

A special acknowledgment is due to Chris Church for spending a lot of time in correcting my English of the thesis in the hottest summer of Ottawa.

I wish to thank all my friends and relatives for their long-time support and encouragement.

Finally, I would like to thank my wife for her endless support, patience, and enduring love.

Dedicated to my Mom to whom I am eternally grateful.

In loving memory of my Dad who is always there in my heart.

Contents

List of Figures

List of Tables

Chapter 1

INTRODUCTION

1.1 Quasicrystals

Quasicrystals (QC's) are a new form of matter which is distinguished from the other two known forms, crystalline (c) and amorphous. They possess a new type of long-range translational order, called *quasiperiodicity*, and a noncrystallographic orientational order associated with the classically forbidden fivefold (icosahedral), eightfold (octagonal), tenfold (decagonal), and twelvefold (dodecagonal) symmetry axes.[1] The family of QC's consists mainly of icosahedral (i) and decagonal (d) systems. In spite of great experimental and theoretical effort, the atomic structure of these complex materials has not been completely solved yet.[2] The main thrust of the physical studies of QC's has been devoted to finding whether the quasiperiodicity leads to expected new physical properties which are significantly different from those of c- and amorphous materials.

The first few years of studies of QC's revealed that their physical properties are disappointingly similar to those of the corresponding c- or the amorphous counterparts.[1, 3, 4] It was only later realized that the first QC's, which were thermodynamically *metastable*, possessed significant structural disorder, as manifested in the broadening of X-ray and/or

electron diffraction lines.[5] In addition, they contained non-negligible amounts of second phases. These poor quality samples impeded the detection of those properties which were intrinsic to quasiperiodicity. They also led to confusion, especially in the area of magnetism of QC's, where some "unusual" magnetic properties were claimed to have been observed.[6] Some of these properties were later shown[7] to result from the presence of magnetic second phases in the studied *i*-alloys.

1.2 Unusual properties of quasicrystals

A significant development in the studies of both structural and physical properties of QC's occurred at the end of the eighties when the thermodynamically *stable* QC's were discovered.[1, 3, 4, 8, 9] These new QC's possess a high degree of structural perfection comparable to that found in the best periodic alloys.[1, 3, 4, 10] Several unusual physical properties have been found in the most intensively studied *i*-alloys:[3, 4]

- First, their most salient feature, which is completely unexpected for alloys consisting of normal metallic elements, is the very high value of the electrical resistivity (ρ). For example, the low-temperature ρ values can reach about 10000 $\mu\Omega$cm in the Al-Cu-Fe[11-14] and Al-Pd-Mn[15-17] *i*-alloys, about 30000 $\mu\Omega$cm in the Al-Cu-Ru *i*-alloys,[18] and the extraordinary high values of the order of 10^7 $\mu\Omega$cm in the Al-Pd-Re *i*-alloys.[19-23] These ρ values are several order of magnitudes larger than those of the constituent metals and of the amorphous alloys, and are comparable to those of doped semiconductors. The conductivity values corresponding to the above experimental ρ values are smaller than the Mott's "minimum metallic conductivity" of 200 Ω^{-1}cm^{-1} for the metal-insulator transition.[24]

- Second, the temperature coefficient of ρ of these new *i*-alloys[1, 3, 4, 8, 9, 19-23] is generally negative, which is inconsistent with the expected behavior for metals.

- Third, the ρ values are extremely sensitive to the sample composition,[19-23] which is reminiscent of doping effects in semiconductors. Even for the same nominal composition, they can change by more than an order of magnitude for samples produced from the same batch.[19, 20] This means the composition inhomogeneities of a fraction of an at. % can significantly influence the electronic properties of the i-alloys.

- Fourth, the resistivity of these new i-alloys increases as their structural quality improves (by annealing which removes the defects),[3, 4, 19-23] in contrast to the behavior of typical metals.

Other unexpected anomalies in the transport properties of i-alloys[1, 3, 4, 8, 9, 19-23] involve a very low electronic contribution to the specific heat (γ), large and strongly temperature-dependent Hall coefficients and thermoelectric power, and a non-Drude-like optical conductivity. From a magnetic point of view, the stable i-alloys of high structural quality are unusual in that they are diamagnetic[17, 25, 26] in spite of containing significant concentrations of transition-metal (TM) atoms.

QC's of d-symmetry combine two structural characteristics: the atoms are ordered quasiperiodically in planes which are stacked with translational periodicity. They represent thus an intermediate state between i- and c-phases.[5] The first stable d-alloys were discovered in the ternary Al-Co-Cu and Al-Co-Ni systems.[27, 28] Samples of high structural quality can be produced in these two systems, which are therefore among the most intensively studied. Most of the studies involving the d-alloys Al-Co-Cu and Al-Co-Ni are associated with their various structural aspects.[29] A few physical measurements which have been carried out on these two compounds showed that, as expected, the electrical resistivity has metallic characteristics along the periodic direction, and exhibits a non-metallic behavior, similar to that observed in i-alloys, in the quasiperiodic plane.[30-35] Anisotropies in the Hall effect,[34, 36, 37] thermopower,[30] thermal conductivity,[38] and op-

tical conductivity[39] have also been observed. These two compounds were also shown to be diamagnetic over a wide temperature range.[40]

1.3 Current issues of quasicrystals

A fundamental question in the physics of *i*-alloys is on the origin of the unusually high values of ρ. The first suggested interpretation, which is still prevailing, is based upon the Hume-Rothery mechanism.[41] As illustrated in the Appendix, this mechanism implies the existence of a pseudogap in the electronic density of states (DOS) in the vicinity of the Fermi level (E_F).[42] Initially, the Hume-Rothery mechanism was invoked, both from experimental[43, 44] and theoretical arguments,[45] in relation to the problem of stability of QC's. It was later linked[46] to the observed large ρ values through the Einstein equation[24] $1/\rho$=conductivity=$e^2DN(E_F)$ in which D is the electron diffusion coefficient (diffusivity) and $N(E_F)$ designates DOS(E_F). The correlation between the high ρ and the low $N(E_F)$ values was based upon the experimental observation of the very small value of the electronic contribution to γ,[3, 4, 46] which is directly proportional to $N(E_F)$.

The support for the Hume-Rothery mechanism in *i*-alloys comes also from the results of the NMR[47] and optical conductivity experiments[48] which were interpreted in terms of the low $N(E_F)$ or the existence of a pseudogap in the DOS around E_F. The reduced $N(E_F)$ is also consistent with the observed diamagnetism. Furthermore, almost all soft X-ray-emission (SXE), soft X-ray absorption (SXA), photoemission spectroscopy (PES), X-ray photoelectron spectroscopy (XPS), and inverse photoemission spectroscopy (IPES) experiments which, as opposed to the experimental techniques mentioned earlier, probe DOS *directly* at energies in the vicinity of E_F, have been interpreted[5, 49] in terms of the presence of the pseudogap in the DOS around E_F. However, some methodological problems of such an interpretation, which are related to the energy resolution used

and to the lifetime broadening effects, and which will be discussed in Chapter 4, have been indicated.[5] A recent study of the *i*-Al-Cu-Fe film by tunneling microscopy claimed to have detected a deep narrow pseudogap 60 meV wide at E_F.[50] The notion of a structure-induced pseudogap in the DOS around E_F results not only from theory based on the nearly-free-electron approximation[45, 51] but is also supported by the electronic structure calculations for the lowest-order *c*-approximants of *i*-alloys,[52–54] including the approximants containing the TM atoms.[53, 54]

Apart from its seeming simplicity, expressed in the relation $Q = 2k_F$, where Q is the magnitude of the reciprocal lattice vector corresponding to the strongest X-ray reflection and k_F is the radius of the Fermi sphere, the Hume-Rothery mechanism is so appealing because it can explain qualitatively why the stable *i*-alloys have both the highest values of ρ and lowest values of γ. It can also be used to rationalize qualitatively why stable *i*-alloys exist only in a rather narrow composition range (a small change in composition can shift the E_F away from the DOS minimum). However, invoking the Hume-Rothery mechanism to explain the stability and electronic properties of *i*-alloys is open to criticism based on general theoretical grounds and on some experimental facts:

- First, fundamental to this mechanism is the concept of a Brillouin zone. It is not clear, however, what is meant by the Brillouin zone in an *i*-alloy for which one cannot define a unique unit cell.[55]

- Second, the often used procedure in support of this mechanism of verifying whether the equality $Q = 2k_F$ holds for a given *i*-alloy requires the values of the valencies of its constituent elements in order to calculate the value of k_F. These values are unknown *a priori* and have to be assumed. Consequently, the whole procedure is questionable.

- Third, a number of theoretical objections against the apparent correlation between the number of valence electrons per atom and a special structural stability

in c-alloys was presented some time ago.[56] It was concluded[56] that there is in general no special stability associated with the Fermi sphere or surface touching the Brillouin zone faces.

As pointed out by Hafner and Krajčí,[57] although the structure-induced pseudogap at E_F seems to be a *generic* property of QC's, it is not a *specific* property distinguishing the quasiperiodic from the periodic or aperiodic phases because it is also present in some c- and amorphous alloys. This is supported by recent NMR results[47] which show low values of DOS(E_F) in both *i*-alloys and their *c*-approximants. According to some electronic structure calculations done for the lowest-order approximants,[53, 57–60] the specific property of QC's seems to be the spikiness of their DOS, resulting from a large number of non-degenerate flat bands. Such DOS spikiness does not occur in *c*- or amorphous systems.[5]

A possible existence of a pseudogap in the DOS around E_F may be not the only reason of the unusual electronic transport properties of stable QC's. There are three other mechanisms which have been recently proposed in the literature.[5, 61] The first one, which is very qualitative in nature, is based on an internal structural model which assumes the presence of conductive *i*-blocks which are surrounded by an insulating layered-structure network.[62] In this structural model the electrical conduction occurs via tunneling which may explain qualitatively many of the electronic transport characteristics of QC's. The other two mechanisms invoke the concepts of localization and critical states.[61]

The electrical conductivity of stable *i*-alloys in the low temperature range has a characteristic temperature dependence: it is proportional to $T^{1/2}$ for the lowest temperatures and to T at higher temperatures.[1, 3, 4, 8, 9, 15] These temperature dependencies, as well as those of magnetoresistance, are usually explained using quantum interference theories (the electron-electron interaction and weak-localization effects).[1, 3, 4, 8, 9, 15] Such theories, however, were originally developed for highly disordered conductors. Thus their appar-

ent relevance to stable *i*-alloys indicates that these alloys are electrically disordered.[5] This, however, poses a question: how can such electronic disorder be reconciled with the apparent high degree of local atomic order in stable *i*-alloys, as determined by diffraction and electron-microscopy experiments? This question will be discussed in Chapter 4.

1.4 Purpose of the project

The electronic transport measurements reviewed above have made an important contribution to the understanding of the electronic structure of QC's. It should be stressed, however, that these measurements provide *indirect* information on the DOS at one particular energy, i.e. the E_F. To determine the electronic structure of QC's one needs information not only on the DOS(E_F), but also on the DOS below and above E_F. Therefore, studies using spectroscopic techniques which probe DOS *directly* at energies in the vicinity of E_F are very desirable. The techniques such as XPS, PES, and SXE spectroscopy have been employed by other research groups to study the DOS below E_F, whereas the DOS above E_F was probed with IPES and SXA spectroscopy in some QC's.[49, 63–78] These electronic structure studies lead to several conclusions, which will be discussed in detail in Chapter 4 in relation to the present study, and which are briefly summarized below:

- First, the most important finding is the apparent observation in some QC's of the pseudogap at E_F, which is predicted by theory and suggested by the results of electronic transport measurements. However, an unambiguous spectroscopic verification of the existence of such pseudogap for QC's containing the TM elements is very difficult because the experimentally measured intensity in the vicinity of E_F is dominated by the TM $3d$ states, as is well known from similar studies of the structural-induced minimum in the DOS in amorphous alloys.[70]

- Second, chemical shifts of the Al $2p$ lines are either zero or very small with respect to similar c-compounds or pure elements. This disagrees with the theoretical result[6, 80] which predicts large shifts and thus confirms the conclusion of recent theoretical studies[81] of the unreliability of predictions[6, 80] based on calculations performed on small clusters.

- Third, a close structural similarity between the valence-band spectra of QC's and those of the corresponding c-compounds was found.

- Finally, various measured spectral features were ascribed to particular electronic states of s, p, and d character, and some arguments for the hybridization between sp and d states were presented.[5]

The purpose of this research project is to study the electronic structures of the high quality i-alloys $Al_{70}Pd_{20}Mn_{10}$,[10] $Al_{65}Cu_{20}Ru_{15}$,[82] $Al_{65}Cu_{20}Os_{15}$,[5] and d-alloys $Al_{65}Co_{15}$-Cu_{20} and $Al_{70}Co_{15}Ni_{15}$[83] using the synchrotron-radiation-based PES technique. By employing the photon-energy dependence of the photoionization cross section (σ) and the effect of the core-electron resonance, it is possible to identify the origin of the prominent features in the valence bands of the studied alloys. In most cases, it is also possible to separate the overlapping contributions due to the d electrons from different elements. Before the emergence of the synchrotron-radiation-based PES technique, such a separation of contributions of a given symmetry (s, p, d, f) due to a specific element could be only obtained from the SXE technique.[82] High energy-resolution ultraviolet photoelectron spectroscopy (UPS) measurements of the i-alloy $Al_{65}Cu_{20}Fe_{7.5}Ru_{7.5}$ were used[84] to study the shape of the valence band near E_F. Based on the experimental results, attempts were made to understand further the strange behavior of the resistivity in QC's. In addition, X-ray diffraction (XRD) patterns of i-$Al_{70}Pd_{20}Mn_{10}$,[10] i-$Al_{65}Cu_{20}Ru_{15}$,[82] and d-$Al_{65}Co_{15}Cu_{20}$ were indexed using several most-often-used schemes to assure that the samples studied are predominantly single-phase and phasonless QC's.

1.5 Scope of the thesis

This thesis contains the research results part of which has been published during the course of the graduate study.[5, 10, 82, 83, 85, 86] Also the methodologies of the XRD pattern indexing (Chapter 2) and of the PES data analysis (Chapter 3) are important contributions achieved. In writing this thesis, a didactic approach was used by describing the Fibonacci chain and 2D projection method as a gradual introduction to the complex structure of QC's (§2.3-4). The most-often-used indexing schemes are presented and exact matrixes and equations are given to enable the reader to use them in practice or to compare the indexing results from various publications (§2.5-6). The methodology of the data analysis of the PES spectra is described in Chapter 3. Whereas the description of the PES technique and the raw data correction are given in §3.1-2, the way how the physics information is obtained from the PES spectra is addressed in the remaining sections of Chapter 3. As an example, the *d*-alloy $Al_{65}Co_{15}Cu_{20}$ is taken to present in detail the analysis of the PES data in that chapter. After the XRD data indexing of *i*-$Al_{70}Pd_{20}Mn_{10}$ is presented in §4.1, the PES spectra are discussed in the next subsections. Next, the PES results of the *i*-$Al_{65}Cu_{20}Os_{15}$ alloy are given in §4.2. They are representative of the family of *i*-alloys $Al_{65}Cu_{20}Md_{15}$ (Md=Fe, Ru, Os). Finally, the UPS spectra of *i*-alloy $Al_{65}Cu_{20}Fe_{7.5}Ru_{7.5}$ are presented in §4.3 followed by the discussion in §4.4.

Chapter 2

SAMPLE CHARACTERIZATION

2.1 Sample preparation

The procedure of sample preparation is extremely critical to the study of physical properties of QC's. There are two reasons for this. First, almost all QC's can exist only in a very narrow composition range. Second, most physical properties of QC's are extremely sensitive to heat treatment and to composition.

Some QC's are *metastable* in the sense that they can exist only in a certain temperature range and transform into c-phases[87] when heated above a certain temperature. Others are *stable* in the sense that they will exist up to a melting point.[88] The former normally can be produced only in the form of ribbons, whereas the latter can be in the forms of ribbon and ingot.

Ingots are prepared[88] by melting mixtures of pure elemental constituents in an argon atmosphere using an arc furnace. In order to produce a homogeneous ingot, one has to turn over the ingot in the furnace and remelt it for two or three times.

Ribbons are produced[88] using a melt spinning apparatus. In this technique, a piece of as-cast but composition-uniformed ingot is melted in a quartz tube, which is in the

center of a coil carrying a high frequency current. The melted liquid is squeezed and injected onto a spinning wheel. Fig. 2.1 shows such an apparatus which was designed during the course of the project.

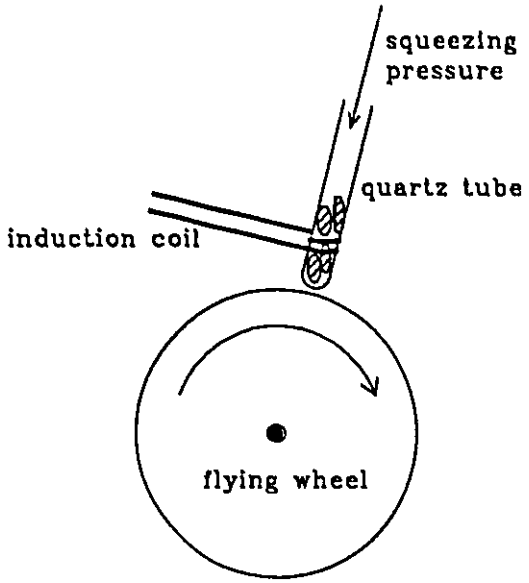

Figure 2.1: **Schematic view of the melt spinning rapid quenching apparatus.**

Many factors have effects on the quality of the ribbons produced:

- A tangent speed of a few tens m/sec is needed in order to solidify the ribbon rapidly. Different compositions may need different speeds;
- For most cases, a vacuum or a certain helium pressure in the experimental chamber is needed to protect ribbons from oxidation;
- The other important parameters are the smoothness of the spinning wheel, the pressure applied to the melted liquid, the size and the shape of the orifice at the bottom of the quartz sample tube, the frequency and the current of the power supply, and the induction of the coil.

Table 2.1 shows all quasicrystalline samples[88] which are studied in this thesis. The samples were kindly provided by Profs. A.-P. Tsai and A. Inoue of Tohoku University, Japan.

Table 2.1: **Summary of quasicrystalline samples studied in this thesis.**

composition	form	heat treatment
i-$Al_{70}Pd_{20}Mn_{10}$	ingot	1123 - 1173 K, 10 h
i-$Al_{65}Cu_{20}Os_{15}$	ingot	1173 K, 48 h
i-$Al_{65}Cu_{20}Ru_{15}$	ingot	1173 K, 48 h
i-$Al_{65}Cu_{20}Fe_{7.5}Ru_{7.5}$	ingot	1173 K, 48 h
d-$Al_{65}Co_{15}Cu_{20}$	ingot	1123 - 1173 K, 48 h
d-$Al_{70}Co_{15}Ni_{15}$	ingot	1123 - 1173 K, 48 h

2.2 X-ray diffraction

2.2.1 Diffractometer

X-ray diffraction measurements on powder samples were performed on a Philips X'Pert scanning diffractometer equipped with a PW3020 vertical goniometer. This goniometer has a 173 mm radius and uses dc motors instead of conventional stepper motors. Θ and 2Θ angles are monitored via two optical encoder disks mounted directly on the drive shaft. This allows a 2Θ accuracy of about 0.003° to be achieved. The diffractometer is also equipped with a variable divergent slit which keeps the illuminated sample area at a constant length of 12.5 mm. A 0.1-mm receiving slit was used in the XRD measurements. With these settings, the instrumental resolution was 0.007 $Å^{-1}$. This resolution was determined from the full width at half maximum of the (111) peak

of a Si standard. Cu$K\alpha$ radiation was employed and the $K\beta$ line was eliminated by using a Kevex PSi2 Peltier cooled Si detector. A value of 1.5405981 Å was taken for the Cu$K\alpha_1$ wavelength throughout all the calculations.[89]

The ingot or ribbon samples were first ground in a silica mortar. Then the fine powder was mixed with methanol and allowed to dry on a low-background sample holder in order to form a thin flat sample. The holder is made from a piece of single crystal Si and gives a small contribution to the background of the XRD spectrum. A sample spinner was used to further reduce the possible preferred sample orientation.

2.2.2 Data fitting and 2Θ correction

For each sample, two spectra were measured. The first spectrum was obtained using only the pure sample. The second one was from a mixture of the quasicrystalline sample and a 10 wt% Si standard reference material 640 b.[90] Peaks of the latter were fitted to a set of Lorentzians.[91] A parabolic background was assumed for each fitted 2Θ segment. Results of the fitting are given in terms of peak positions, widths, heights, and integrated areas.

The 2Θ angles were corrected for the possible instrumental aberration and specimen displacement.[92] First, the difference of the peak positions of the Si standard and that of the Si standard mixed with a specimen was calculated: $\Delta(2\Theta)_{Si}=2\Theta_{Si\_expt}-2\Theta_{Si\_std}$. Next, the difference was fitted to a fourth order polynomial function of $2\Theta_{expt}$, which is referred to as $\Delta(2\Theta)_{Si\_fit}$.[92] Finally, all positions of the i- or d-peaks were corrected according to the equation: $2\Theta_{corr}=2\Theta_{expt}-\Delta(2\Theta)_{Si\_fit}$.

Three Fortran programs[93] were implemented during the course of the study for indexing the i- and d-structures using several indexing schemes described in §2.5 and §2.6. The input data file for the indexing programs needs three columns: the uncorrected positions, widths and heights of all i- or d-peaks. The first line of the input file is for

the five parameters of the $\Delta(2\Theta)_{Si\_fit}$ curve. These parameters can also be entered from the keyboard when running the programs.

2.3 Brief review of diffraction by crystals

A crystal lattice in $3D$ is defined by three fundamental translation vectors $\mathbf{a}_1$, $\mathbf{a}_2$, $\mathbf{a}_3$ such that the atomic arrangement looks the same in every respect when viewed from the point $\mathbf{r}$ and $\mathbf{r}'=\mathbf{r} + m_1\mathbf{a}_1 + m_2\mathbf{a}_2 + m_3\mathbf{a}_3$.[94] These vectors can be either conventional or primitive. A lattice translation operation is defined as the displacement of a crystal by a crystal translation vector

$$\mathbf{T} = m_1\mathbf{a}_1 + m_2\mathbf{a}_2 + m_3\mathbf{a}_3. \tag{2.1}$$

Miller indexes are very useful in describing the crystal structures. These indexes can be determined by the following prescription:[1]

- find the intercepts x, y, z on the coordinate axis for the plane of interest;
- express the intercepts in terms of basic vectors of the unit cell: x/a_1, y/a_2, z/a_3 (these are necessarily rational numbers);
- form the reciprocals a_1/x, a_2/y, a_3/z;
- express as the triplet of the smallest integers hkl, written (hkl), which may denote a single plane or a family of parallel planes.

The distance from the origin to the plane (hkl) lying within the unit cell is the interplanar spacing d_{hkl}.

A reciprocal lattice is defined as

$$\mathbf{G}(n_1, n_2, n_3) = n_1\mathbf{b}_1 + n_2\mathbf{b}_2 + n_3\mathbf{b}_3, \tag{2.2}$$

in which n_1, n_2, n_3 are integers, $\mathbf{b}_1$ is defined as

$$\mathbf{b}_1 = 2\pi \frac{\mathbf{a}_2 \times \mathbf{a}_3}{\mathbf{a}_1 \cdot (\mathbf{a}_2 \times \mathbf{a}_3)}, \tag{2.3}$$

and $\mathbf{b}_2$, $\mathbf{b}_3$ can be obtained by cyclic permutations. The vectors **a** and **b** fulfill the relation

$$\mathbf{a}_i \cdot \mathbf{b}_j = 2\pi \delta_{ij}. \tag{2.4}$$

A nD equal-side orthogonal lattice (i.e., a square when n=2, a cube when n=3, and a hypercube when $n \geq 4$) has the following basis in the physical and reciprocal space

$$\begin{aligned} (\mathbf{a}_1, \mathbf{a}_2, ..., \mathbf{a}_n) &= \mathrm{a}(\mathbf{e}_1, \mathbf{e}_2, ..., \mathbf{e}_n), \\ (\mathbf{b}_1, \mathbf{b}_2, ..., \mathbf{b}_n) &= \frac{2\pi}{\mathrm{a}}(\mathbf{e}_1, \mathbf{e}_2, ..., \mathbf{e}_n). \end{aligned} \tag{2.5}$$

Here $(\mathbf{b}_1, \mathbf{b}_2, ..., \mathbf{b}_n)$ is a set of basis vectors orthogonal to each other. If there is a common factor n for (n_1, n_2, n_3) in Eq. (2.2), i.e. (n_1, n_2, n_3)=$n(hkl)$, then it can be shown that

$$| \mathbf{G}_{n_1 n_2 n_3} | = 2\pi/(d_{hkl}/n), \tag{2.6}$$

$$| \mathbf{G}_{(hkl)} | = 2\pi/(d_{hkl}), \tag{2.7}$$

where d_{hkl} is the interplanar spacing for planes (hkl).

The expansion of the Fourier analysis to a periodic electron density function n(**r**) in a crystal with reciprocal lattice **G** is straightforward

$$n(\mathbf{r}) = \sum_{\mathbf{G}} n_{\mathbf{G}} \exp(i\mathbf{G} \cdot \mathbf{r}). \tag{2.8}$$

This result is invariant under all crystal translation **T**, as defined in Eq. (2.1), that leaves the crystal invariant. Inversion of Eq. (2.8) gives

$$n_{\mathbf{G}} = \frac{1}{V_c} \int_{cell} dV n(\mathbf{r}) \exp(-i\mathbf{G} \cdot \mathbf{r}). \tag{2.9}$$

With these definitions in mind, the diffraction condition can easily be derived. Suppose that the wavevectors of the incoming and outgoing beams are k and k′, respectively. Then the difference of the phase factor between beams scattered from volume elements r apart is $\exp[i(\mathbf{k}-\mathbf{k}')\cdot\mathbf{r}]=\exp[-i\Delta\mathbf{k}\cdot\mathbf{r}]$. The scattering amplitude is defined as

$$F = \int dV n(\mathbf{r}) \exp[i(\mathbf{k}-\mathbf{k}')\cdot\mathbf{r}] \quad (2.10)$$

$$= \int dV n(\mathbf{r}) \exp(-i\Delta\mathbf{k}\cdot\mathbf{r}) \quad (2.11)$$

$$= \sum_{\mathbf{G}} \int dV n_{\mathbf{G}} \exp[i(\mathbf{G}-\Delta\mathbf{k})\cdot\mathbf{r}]. \quad (2.12)$$

When the scattering vector is equal to a reciprocal lattice vector $\Delta\mathbf{k}=\mathbf{G}$, then $F=Vn_{\mathbf{G}}$. If $n_{\mathbf{G}}$ is not equal to zero, a peak will show up at G. A very simple diffraction condition can be written as

$$2d_{hkl}\sin\theta = n\lambda. \quad (2.13)$$

This means that the set of reciprocal lattice vectors G determines all possible X-ray reflections.

When the lattice cell is conventional instead of primitive, some values of $n_{\mathbf{G}}$ in Eq. (2.9) will be equal to zero. The peaks corresponding to zero-amplitude G's would not appear in the diffraction spectra. The set of conditions that determines the allowed and forbidden (hkl)'s are called the rules of extinction. For example, for a face-centered cubic lattice h, k, l must be all odd or all even. Usually there are three kinds of Bravais lattices in cubic system: simple cubic P(a), body-centered cubic I(a), and face-centered cubic F(a). The side length of the conventional cubic cell is a. One can also use the same conventional cubic cell for a face-centered cubic lattice having side of 2a, denoted by F(2a). The extinction rules of the cubic lattices are summarized in Table 2.3.

The structures of condensed matters are mostly investigated via diffraction experiments (electrons, X-rays, or neutrons) which produce intensity distributions related to

Table 2.2: **Extinction rules of the cubic structures.**

Bravais	Miller indexes allowed	reflection examples
F(2a)	h, k, l all integers	(100)
	and all half integers	$(\frac{1}{2}\frac{1}{2}\frac{1}{2})$
P(a)	h, k, l all integers	(100)
I(a)	$h + k + l$ even	(110)
F(a)	h, k, l all odd or even	(111), (204)

the Fourier transform of the structures. Long-range order means[1] a finite number (possibly very large) of Fourier components, with sharp diffraction peaks. c-materials are periodic and therefore must have long-range order. Disordered materials, such as gases, liquids, and amorphous solids, have neither periodicity nor long-range order. However, QC's do not have a periodic structure, but have a perfect orientational long-range order. The next section gives an example which introduces the concept of quasiperiodicity.

2.4 Fibonacci chain and cut-projection method

2.4.1 Fibonacci chain

Non-periodic long-range-ordered structures can be theoretically constructed using any non-random procedure to generate atomic arrangements.[1] A very useful $1D$ example is the so-called Fibonacci chain. It consists of an infinite sequence of two segments: one shorter denoted as S, and another longer denoted as L. One of several ways to obtain the chain is to start with a certain finite sequence, say, L, and then operate with the iterative rule $S \rightarrow L$ and $L \rightarrow LS$.[1] Infinite repetition of the operation gives an infinite sequence of L, S, which is obviously perfectly ordered at a long distance (not randomly

at all). At any point in the chain, the type of segment (S or L) that must be found is uniquely determined by the chosen starting sequence. According to the construction rule, the growing strings in the successive iterations are L, LS, LSL, $LSLLS$, $LSLLSLSL$, $LSLLSLSLLSLLS$..., etc. If the length ratio L/S of the two segments is an irrational number, the sequence has no repetition distance. The canonical Fibonacci chain can be obtained when the irrational number is equal to τ, the so-called golden mean

$$\tau = 2\cos 36^\circ = (1+\sqrt{5})/2 = 1.618034\ldots . \tag{2.14}$$

The sharp peaks of the reflections for the Fibonacci chain can be obtained[1] immediately. However, it is more helpful to calculate the diffraction pattern by means of the cut and projection method, as described in the following section. The ideas of the cut and projection method can help to describe QC's in higher dimensions.

2.4.2 Cut and projection from $2D$ to $1D$

The origin of quasicrystalline structures arises from the fact that their orientation symmetries are not compatible with space groups which are accepted in the relevant physical space.[1] But these forbidden point group symmetries may be accepted by periodic tiling at the cost of increasing dimensionality. The so-called projection and cut procedures are widely used for this purpose and Fibonacci chain is a good starting point.

The following function,[1] for example, is periodic in $2D$

$$\rho(x,y) = \sum_{n,m} \delta(x-na)\delta(y-ma). \tag{2.15}$$

Fig. 2.2 shows the distribution of density points at the vertices of the square lattice. Its Fourier components are distributed at the vectors of a square lattice with the spacing of $2\pi/a$ in reciprocal space as a periodic function[1]

$$\mathbf{F}_{hh'} = \sum_{h,h'} \delta(\mathbf{Q}-\mathbf{Q}_{hh'}), \tag{2.16}$$

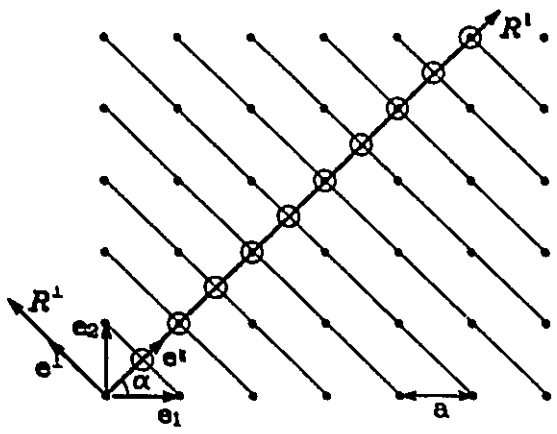

Figure 2.2: **A square lattice of $2D$ (•) projects on a line of $1D$ space as a $1D$ periodic structure (○) as long as the slope of the $1D$ space into the 2D is rational with respect to the lattice rows.**[1]

where $\mathbf{Q}_{hh'}$ is a reciprocal lattice vector. This vector can be presented in an orthogonal coordinate system or projected onto any $1D$ subspace as a straight line. For example, $\mathbf{R}^{\parallel}$ in Fig. 2.2 can be taken as a subspace. A simple geometrical analysis shows that

$$\begin{aligned}\mathbf{Q}_{hh'} &= \frac{2\pi}{a}h\mathbf{e}_1 + \frac{2\pi}{a}h'\mathbf{e}_2 \\ &= \frac{2\pi}{a}(h\cos\alpha + h'\sin\alpha)\mathbf{e}^{\parallel} + \frac{2\pi}{a}(-h\sin\alpha + h'\cos\alpha)\mathbf{e}^{\perp}. \end{aligned} \tag{2.17}$$

An alternative expression of Eq. (2.17) is

$$\mathbf{Q}_{hh'} = \mathbf{Q}^{\parallel}_{hh'} + \mathbf{Q}^{\perp}_{hh'}, \tag{2.18}$$

where

$$\begin{aligned}\mathbf{Q}^{\parallel}_{hh'} &= \hat{P}^{\parallel}\mathbf{Q}_{hh'} \\ &= \left[\hat{P}^{\parallel}(h\mathbf{e}_1 + h'\mathbf{e}_2)\right]\frac{2\pi}{a} \\ &= \left[\hat{P}^{\parallel}(\mathbf{e}_1, \mathbf{e}_2)\right]\begin{pmatrix} h \\ h' \end{pmatrix}\frac{2\pi}{a}\end{aligned}$$

$$= (\mathbf{e}_1, \mathbf{e}_2) \left[D(P^{\parallel}) \begin{pmatrix} h \\ h' \end{pmatrix} \right] \frac{2\pi}{a}, \tag{2.19}$$

$$D(P^{\parallel}) = \begin{pmatrix} \cos^2\alpha & \cos\alpha \sin\alpha \\ \cos\alpha \sin\alpha & \sin^2\alpha \end{pmatrix}. \tag{2.20}$$

Similarly, one has

$$\mathbf{Q}^{\perp}_{hh'} = \hat{P}^{\perp}\mathbf{Q}_{hh'}$$

$$= (\mathbf{e}_1, \mathbf{e}_2) \left[D(P^{\perp}) \begin{pmatrix} h \\ h' \end{pmatrix} \right] \frac{2\pi}{a}, \tag{2.21}$$

$$D(P^{\perp}) = I - D(P^{\parallel})$$

$$= \begin{pmatrix} \sin^2\alpha & -\cos\alpha \sin\alpha \\ -\cos\alpha \sin\alpha & \cos^2\alpha \end{pmatrix}. \tag{2.22}$$

For a case in higher dimensions, a projection operator is more convenient than the geometrical analysis. Once the matrixes of the projection operators $D(P^{\parallel})$ and $D(P^{\perp})$ are known, the calculations of $\mathbf{Q}^{\parallel}_{hh'}$ and $\mathbf{Q}^{\parallel}_{hh'}$ are straightforward.

If $\tan\alpha$ is *rational*, the projected $1D$ structure of the infinite $2D$ lattice is a set of **discrete periodic** sites. If $\tan\alpha$ is *irrational*, the projected $1D$ structure is no longer periodic and is generally of no interest. However, a dramatic result comes about when the projections on $\mathbf{R}^{\parallel}$ are not from the whole lattice (Fig. 2.3), but are restricted to those points of the square lattice which are confined within a strip parallel to $\mathbf{R}^{\parallel}$.[1] This strip has a width of Δ=a($\cos\alpha + \sin\alpha$), and $\cos\alpha/\sin\alpha = \tau$. It turns out that the distribution of segments (L=a$\cos\alpha$, S=a$\sin\alpha$) over $\mathbf{R}^{\parallel}$ obeys now a Fibonacci sequence (Fig. 2.3). Thus the strip/projection scheme provides an easy way to generate a non-periodic, but long-range ordered structure when the high dimensional periodic structure compatible with the required symmetry operation is known.[1]

This scheme simplifies the process of Fourier analysis of the diffraction patterns. The Fourier components of a square lattice are equally intense peaks distributed at

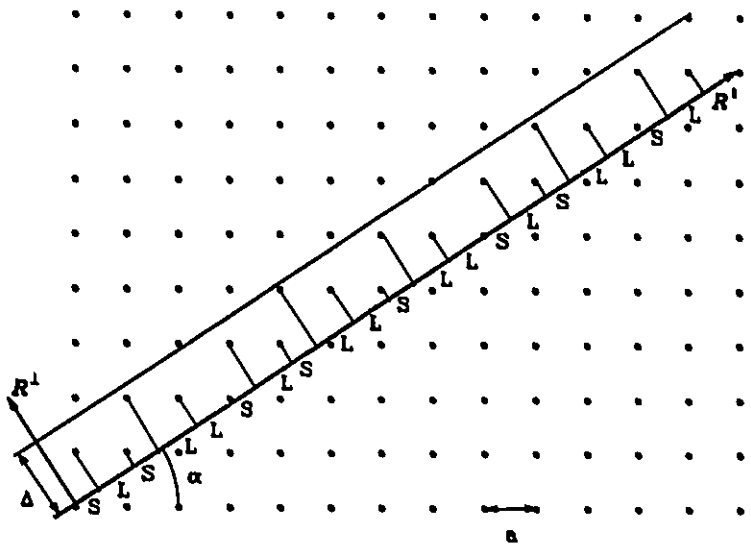

Figure 2.3: **Illustration of the strip/projection method. The slope of $\mathbf{R}^{\parallel}$ is irrational. Projections of the portion of the square lattice inside the trip form a perfectly non-periodic, but long-range ordered structure. With the slope equal to τ, the Fibonacci chain is obtained.**[1]

the vectors $\mathbf{Q}_{hh'}$ of the reciprocal square lattice [Eq. (2.16)]. It can be proven[1] that the Fourier pattern of the strip is the convolution product of the Fourier pattern of the infinite square lattice and the Fourier transform $G(Q^{\perp})$ of a strip window function $W(x^{\perp})$ (Ref. [1])

$$G(Q^{\perp}) \cong \Delta\left[\sin\left(\frac{Q^{\perp}\Delta}{2}\right)\right]\left(\frac{Q^{\perp}\Delta}{2}\right)^{-1}. \tag{2.23}$$

From a view along $\mathbf{R}^{\parallel}$, the total diffraction structure factor of the strip, or that of the Fibonacci chain, is[1]

$$F(Q^{\parallel}) = \sum_{hh'}\delta(Q^{\parallel} - Q^{\parallel}_{hh'})G(Q^{\perp}_{hh'})/a. \tag{2.24}$$

Here $Q^{\parallel}$ stands for the component of a continuous vector variable in the reciprocal space along the strip direction $\mathbf{R}^{\parallel}$. $Q^{\parallel}_{hh'}$ and $Q^{\perp}_{hh'}$ are the components of the discrete reciprocal

periodic lattice in the same space along $\mathbf{R}^{\parallel}$ and $\mathbf{R}^{\perp}$, respectively, and are given by

$$Q^{\parallel}_{hh'} = \frac{2\pi}{a}\frac{1}{(2+\tau)^{1/2}}(h\tau + h') \tag{2.25}$$

and

$$Q^{\perp}_{hh'} = \frac{2\pi}{a}\frac{1}{(2+\tau)^{1/2}}(h'\tau - h). \tag{2.26}$$

This corresponds to a reciprocal lattice vector

$$\begin{aligned} Q_x &= \frac{2\pi}{a}h, \\ Q_y &= \frac{2\pi}{a}h', \end{aligned} \tag{2.27}$$

i.e., from Eq. (2.17),

$$\mathbf{Q}_{hh'} = \frac{2\pi}{a}h\mathbf{e}_1 + \frac{2\pi}{a}h'\mathbf{e}_2 \tag{2.28}$$

$$= Q^{\parallel}_{hh'}\mathbf{e}^{\parallel} + Q^{\perp}_{hh'}\mathbf{e}^{\perp}. \tag{2.29}$$

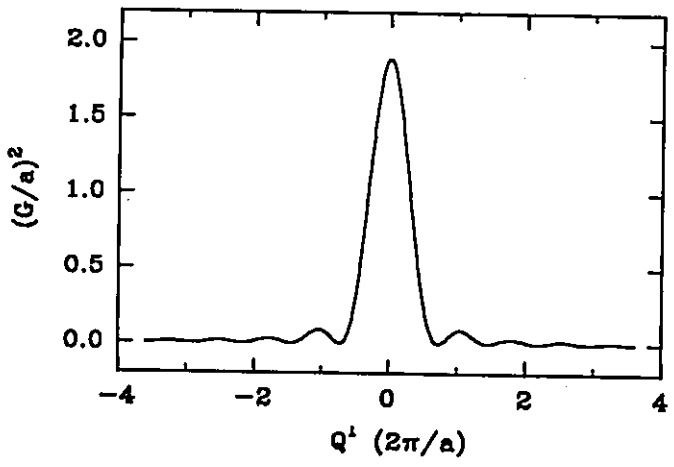

Figure 2.4: **Relative intensity of XRD spots as a function of $Q^{\perp}$ for the Fibonacci chain.**

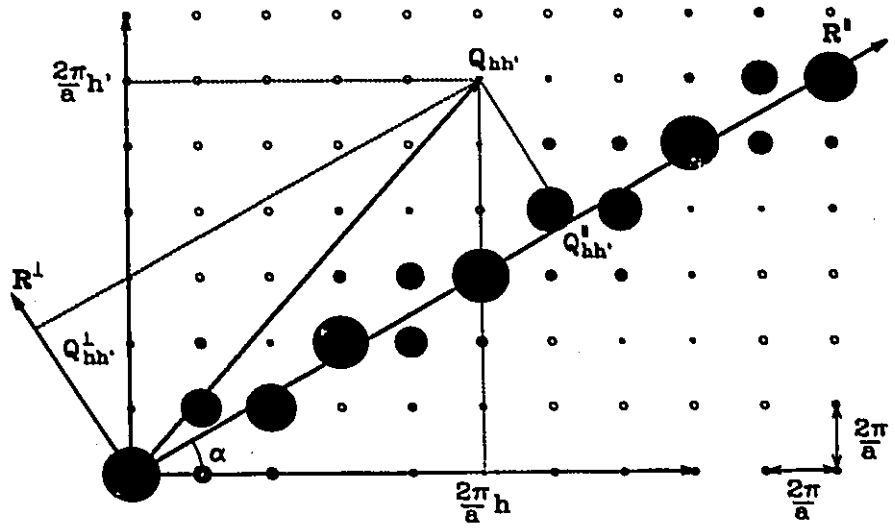

Figure 2.5: **Fourier pattern of the $2D$ strip shown in Fig. 2.3. Positions are determined by $\delta(Q^{\parallel}-Q^{\parallel}_{hh'})$. Diameters of the closed circles are proportional to $[G(Q^{\perp})/a]^2$. Open circles appear wherever $[G(Q^{\perp})/a]^2 \leq 0.5\%$ of the maximum value of $[G(Q^{\perp})/a]^2$.**

It is clear that the positions of the diffraction spots of the Fibonacci chain are exactly the same as those of the $2D$ infinite lattice. These positions are uniformly distributed in the $2D$ reciprocal space and labeled by two integers (h, h'). These spots are sharp in both cases. However, the intensities of the diffraction spots for the Fibonacci chain are modulated by Eq. (2.23). The shape of $[G(Q^{\perp})/a]^2$ which is proportional to the intensities of the XRD spots is shown in Fig. 2.4. When $Q^{\perp}\Delta/2$ is equal to π, $[G(Q^{\perp})/a]^2$=0. This means that only when $|Q^{\perp}|$ is within $2\pi/\Delta=(2+\tau)^{1/2}/(1+\tau)(2\pi/a) \approx 0.7(2\pi/a)$, will those diffraction spots have a significant measurable intensity (Fig. 2.5).

2.5 Icosahedral structure

Two kinds of quasicrystalline structures are studied in the thesis: i- and d-structures. Both i- and d-structures are the $3D$ structures of QC's. The example in §2.4 of the

Fibonacci chain shows that a space in a dimension higher than three is necessary in order to explore the diffraction properties of QC's. It turns out that the i-structure may be described in $6D$ space[95–97] and the d-structure may be analyzed either in $5D$ or $6D$ space.[98, 99]

There are several schemes to describe i-structures. They were proposed respectively by Elser,[95] Bancel et al.,[96] and Cahn et al.[97] It is useful to make a comparison of these schemes in order to enable the reader to make convenient identification of the diffraction patterns from various publications in which one of these schemes is used. The $1D$ example in §2.4 has been presented in such a way that a generation of higher-dimensional constructions is straightforward.

2.5.1 Elser scheme

In the Elser scheme,[95] the i-quasilattice is obtained by projecting a subset of the $6D$ lattice ${}^6\mathcal{R}$, whose unit cell is a hypercube, into a special $3D$ hyperplane ${}^3\mathcal{R}^{\parallel}$. The orientation of this hyperplane with respect to the lattice is determined by the requirement that the projected basis vectors

$$\begin{aligned}(\mathbf{e}_1^{\parallel}, \mathbf{e}_2^{\parallel}, \mathbf{e}_3^{\parallel}, \mathbf{e}_4^{\parallel}, \mathbf{e}_5^{\parallel}, \mathbf{e}_6^{\parallel}) &= \hat{P}^{\parallel}(\mathbf{e}_1, \mathbf{e}_2, \mathbf{e}_3, \mathbf{e}_4, \mathbf{e}_5, \mathbf{e}_6) \\ &= (\mathbf{e}_1, \mathbf{e}_2, \mathbf{e}_3, \mathbf{e}_4, \mathbf{e}_5, \mathbf{e}_6) D(P^{\parallel}) \qquad (2.30)\end{aligned}$$

coincide with the six vertex axes of the icosahedron. This leads to a diffraction pattern having the i-symmetry. The matrix presentation of the projection operator in Eq. (2.30)

is[95]

$$D(P^{\parallel}) = \frac{1}{\sqrt{20}} \begin{pmatrix} \sqrt{5} & 1 & 1 & 1 & 1 & 1 \\ 1 & \sqrt{5} & 1 & -1 & -1 & 1 \\ 1 & 1 & \sqrt{5} & 1 & -1 & -1 \\ 1 & -1 & 1 & \sqrt{5} & 1 & -1 \\ 1 & -1 & -1 & 1 & \sqrt{5} & 1 \\ 1 & 1 & -1 & -1 & 1 & \sqrt{5} \end{pmatrix}. \quad (2.31)$$

It can be proven that this matrix and the matrix representing $P_{\perp}$ have rank three, and therefore each of them can produce only three independent vectors. The vectors $(\mathbf{e}_1^{\parallel}, \mathbf{e}_2^{\parallel}, \mathbf{e}_3^{\parallel}, \mathbf{e}_4^{\parallel}, \mathbf{e}_5^{\parallel}, \mathbf{e}_6^{\parallel})$ are along the six vertex directions of the i-quasilattice (Fig. 2.6). By using Eqs. (2.30) and (2.31), any reciprocal lattice in the $6D$ space can be projected

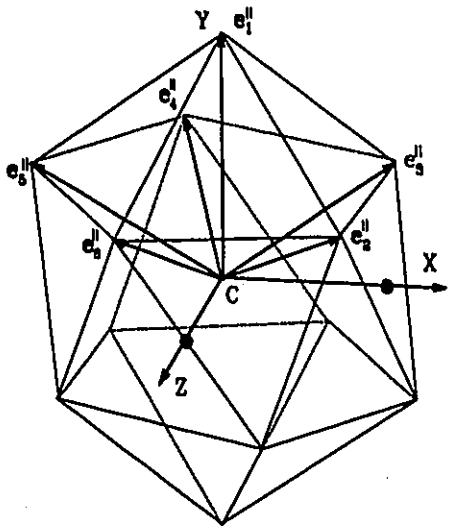

Figure 2.6: **Icosahedron and the projected basis vectors $(\mathbf{e}_1^{\parallel}, \mathbf{e}_2^{\parallel}, \mathbf{e}_3^{\parallel}, \mathbf{e}_4^{\parallel}, \mathbf{e}_5^{\parallel}, \mathbf{e}_6^{\parallel})$ of the icosahedral quasilattice.**

into the $3D$ space

$$\mathbf{Q}^{\parallel}(n_1, n_2, n_3, n_4, n_5, n_6) = \hat{P}^{\parallel}\mathbf{Q}(n_1, n_2, n_3, n_4, n_5, n_6)$$

$$
\begin{aligned}
&= \hat{P}^{\parallel}(n_1\mathbf{e}_1 + n_2\mathbf{e}_2 + n_3\mathbf{e}_3 + n_4\mathbf{e}_4 + n_5\mathbf{e}_5 + n_6\mathbf{e}_6)\frac{2\pi}{a_{6D}} \\
&= \left[\hat{P}^{\parallel}(\mathbf{e}_1, \mathbf{e}_2, \mathbf{e}_3, \mathbf{e}_4, \mathbf{e}_5, \mathbf{e}_6)\right](n_1, n_2, n_3, n_4, n_5, n_6)^T\frac{2\pi}{a_{6D}} \\
&= (\mathbf{e}_1, \mathbf{e}_2, \mathbf{e}_3, \mathbf{e}_4, \mathbf{e}_5, \mathbf{e}_6)\left[D(P^{\parallel})(n_1, n_2, n_3, n_4, n_5, n_6)^T\right]\frac{2\pi}{a_{6D}}.
\end{aligned} \tag{2.32}
$$

The magnitude of $\mathbf{Q}^{\parallel}(n_1, n_2, n_3, n_4, n_5, n_6)$ is $4\pi \sin\theta/\lambda$ and it can be determined from an XRD spectrum. The last line in Eq. (2.32) allows one to calculate

$$
|\mathbf{Q}^{\parallel}| = \frac{2\pi}{a_{6D}}\left\{\sum_{i=1}^{6}\left[\sum_{j=1}^{6} D(P^{\parallel})_{ij}n_j\right]^2\right\}^{1/2}. \tag{2.33}
$$

For example, for the peak (221001) in the Elser scheme, Eqs. (2.33) and (2.31) give

$$
\begin{aligned}
|\mathbf{Q}^{\parallel}(n_1, n_2, n_3, n_4, n_5, n_6)| &= \frac{2\pi}{\sqrt{20}a_{6D}}[(2\sqrt{5}+2+1+1)^2 + (2+2\sqrt{5}+1+1)^2 \\
&\quad +(2+2+\sqrt{5}-1)^2 + (2-2+1-1)^2 \\
&\quad +(2-2-1+1)^2 + (2+2-1+\sqrt{5})^2]^{1/2} \\
&= 3.1495\frac{2\pi}{a_{6D}}.
\end{aligned} \tag{2.34}
$$

For example,[10] from the XRD spectrum of i-$Al_{70}Pd_{20}Mn_{10}$ $|\mathbf{Q}^{\parallel}(221001)|$ was found to be 3.091 Å^{-1}. Using Eq. (2.34) gives a_{6D}=6.402 Å.

2.5.2 Bancel scheme

The Bancel scheme is slightly different than the Elser scheme. If the indexes in the Bancel scheme are $(n_1^B, n_2^B, n_3^B, n_4^B, n_5^B, n_6^B)$, then the corresponding indexes in the Elser scheme are

$$
(n_1^E, n_2^E, n_3^E, n_4^E, n_5^E, n_6^E) = \tau^3(n_1^B, n_5^B, \bar{n}_6^B, n_4^B, \bar{n}_2^B, n_3^B). \tag{2.35}
$$

To calculate $|\mathbf{Q}^{\parallel}|$ corresponding to $(110000)_{Bancel}$ peak, Eq. (2.35) is used to convert the index $(110000)_{Bancel}$ to the index $\tau^3(1000\bar{1}0)_{Elser}$ and then Eq. (2.33) gives the

result which is exactly the same as the result in Eq. (2.34). It can be shown that $\tau^3(100\bar{1}0)_{Elser}$=$(221001)_{Elser}$. This relation is often referred to as an inflation by τ^3.

2.5.3 Cahn scheme

There are three kinds of indexing notations related to the Cahn scheme:

- $(n_1^c, n_2^c, n_3^c, n_4^c, n_5^c, n_6^c)_{Cahn}$ which is equivalent to $(n_1^c, n_2^c, n_5^c, \bar{n}_6^c, n_4^c, n_3^c)_{Elser}$;
- (h/h', k/k', l/l') which is equivalent to $\frac{1}{2}(h+k', l+h', h'-l, k-l', k'-h, k+l')_{Elser}$ or $\frac{1}{2}(h+k', l+h', k+l', k'-h, h'-l, l'-k)_{Cahn}$, and
- N/M system in which $|\mathbf{Q}^{\shortparallel}|$ can be expressed as

$$|\mathbf{Q}^{\shortparallel}| = \left[\frac{N+M\tau}{2(2+\tau)}\right]^{1/2}\left(\frac{2\pi}{a_{6D}}\right). \tag{2.36}$$

N and M of Eq. (2.36) are given by

$$N = 2\sum_{i=1}^{6} n_i^2, \tag{2.37}$$

$$M = (n_2+n_5)^2+(n_1+n_4)^2+(n_3+n_6)^2+2[(n_1-n_4)(n_2+n_5) +(n_3-n_6)(n_1+n_4)+(n_2-n_5)(n_3+n_6)]. \tag{2.38}$$

Let's take the peak $(221001)_{Elser}$ of i-$Al_{70}Pd_{20}Mn_{10}$ as an example.[10] The corresponding indexes of this peak in the Cahn scheme is $(221010)_{Cahn}$. Eqs. (2.37) and (2.38) result in N=20 and M=32 and Eq. (2.36) gives the same result for $|\mathbf{Q}^{\shortparallel}|$ as does Eq. (2.33).

So far three different kinds of i-structures have been observed.[100] They correspond to the $6D$ hypercubic lattices F(2a), P(a), and I(a). The detailed calculations show that N and M obey definite rules for the three lattices. The extinction rules for i-alloys (Table 2.5.3) are similar to those for c-alloys (Table 2.3).

Based on the indexing schemes described above, a Fortran program INDEX.FOR[93] was written to identify the XRD patterns of the i-alloys. One initial i-peak has to

Table 2.3: **Extinction rules of the *i*-alloys.**

Lattice	N	M	$(n_1, n_2, n_3, n_4, n_5, n_6)$
F(2a)	4n	$4m = 4 \cdot INT(N\tau/4)$	any integers
	4n+2	$4m+1 = 4 \cdot INT((N\tau - 1)/4) + 1$	any integers
	4n+3	$m = INT(N\tau)$	all half integers
P(a)	4n	$4m = 4 \cdot INT(N\tau/4)$	any integers
	4n+2	$4m+1 = 4 \cdot INT((N\tau - 1)/4) + 1$	any integers
I(a)	4n	$4m = 4 \cdot INT(N\tau/4)$	$\sum n_i = 2n$

be assigned to the value of $|\mathbf{Q}^{\parallel}|$ (or 2Θ) and the associated index. Then the program calculates the value of lattice constant a, generates all possible peaks, and compares them with the experimental ones. All forms of the indexes in the three schemes are given for each matched i-peak in order to enable the reader to make convenient identification of the i-peaks.

2.6 Decagonal structure

In contrast to the i-structure, the d-structure is periodic in one direction, usually taken along the Z axis, and aperiodic in the XY plane. Two schemes are employed widely to describe the d-structure. They were proposed respectively by Yamamoto et al.[98] and Takeuchi et al.[99] This section outlines the basic ideas associated with these two indexing schemes.

2.6.1 Yamamoto scheme

In the Yamamoto scheme,[98] the d-quasilattice is obtained by projecting a subset of the $5D$ lattice ${}^5R$ into a special $3D$ hyperplane ${}^3R^{\parallel}$. Its orientation relative to the lattice is determined by the requirement that the first four projected basis vectors $(\mathbf{e}_1^{\parallel}, \mathbf{e}_2^{\parallel}, \mathbf{e}_3^{\parallel}, \mathbf{e}_4^{\parallel})$ are in the X-Y plane and have an angle $2i\pi/5$ (i=1, ..., 4) with respect to X direction. The basis vector $\mathbf{e}_5^{\parallel}$ is along Z direction, i.e. along the periodic direction. The five orthogonal unit vectors $(\mathbf{e}_1, \mathbf{e}_2, \mathbf{e}_3, \mathbf{e}_4, \mathbf{e}_5)$ are defined in such a way that $\mathbf{e}_1, \mathbf{e}_2, \mathbf{e}_5$ span the external space $(\mathbf{Q}^{\parallel})$ and are along X, Y, Z direction, whereas $\mathbf{e}_3, \mathbf{e}_4$ span the internal space $(\mathbf{Q}^{\perp})$.

The basic $5D$ lattice vectors of the decagonal structure are defined as

$$(\mathbf{a}_1, \mathbf{a}_2, \mathbf{a}_3, \mathbf{a}_4, \mathbf{a}_5) = (\mathbf{e}_1, \mathbf{e}_2, \mathbf{e}_3, \mathbf{e}_4, \mathbf{e}_5)\tilde{M}a, \tag{2.39}$$

where matrix $\tilde{M}$ is defined as[98]

$$\tilde{M} = \frac{2}{\sqrt{5}} \begin{pmatrix} c_1 - 1 & c_2 - 1 & c_3 - 1 & c_4 - 1 & 0 \\ s_1 & s_2 & s_3 & s_4 & 0 \\ c_2 - 1 & c_4 - 1 & c_1 - 1 & c_3 - 1 & 0 \\ s_2 & s_4 & s_1 & s_3 & 0 \\ 0 & 0 & 0 & 0 & \sqrt{5}c/(2a) \end{pmatrix}. \tag{2.40}$$

Here c_j=cos($2\pi j/5$) and s_j=sin($2\pi j/5$), where j=1, ..., 4. Unlike the i-structure where $\mathbf{a}_i$=$\mathbf{e}_i a$, here one can see that $\mathbf{a}_i$ is not equal to $\mathbf{e}_i a$, and all $\mathbf{a}_i$'s are not orthogonal. Therefore the unit cell of the d-structure in the $5D$ space is not a hypercube.

The reciprocal basis vectors can be defined as[98]

$$(\mathbf{b}_1, \mathbf{b}_2, \mathbf{b}_3, \mathbf{b}_4, \mathbf{b}_5) = (\mathbf{e}_1, \mathbf{e}_2, \mathbf{e}_3, \mathbf{e}_4, \mathbf{e}_5)M^{-1}\frac{2\pi}{a}, \tag{2.41}$$

where matrix M^{-1} is defined as[98]

$$M^{-1} = \frac{1}{\sqrt{5}} \begin{pmatrix} c_1 & c_2 & c_3 & c_4 & 0 \\ s_1 & s_2 & s_3 & s_4 & 0 \\ c_2 & c_4 & c_1 & c_3 & 0 \\ s_2 & s_4 & s_1 & s_3 & 0 \\ 0 & 0 & 0 & 0 & \sqrt{5}a/c \end{pmatrix}. \tag{2.42}$$

It can be proven that $\mathbf{a}_i \cdot \mathbf{b}_j = 2\pi\delta_{ij}$.

The projection matrix for the d-structure is similar to that in Eq. (2.31) and is given by[98]

$$D(P^{\parallel}) = \frac{1}{\sqrt{5}} \begin{pmatrix} c_1 & c_2 & c_3 & c_4 & 0 \\ s_1 & s_2 & s_3 & s_4 & 0 \\ 0 & 0 & 0 & 0 & 0 \\ 0 & 0 & 0 & 0 & 0 \\ 0 & 0 & 0 & 0 & \sqrt{5}a/c \end{pmatrix}. \tag{2.43}$$

The following equation is used to calculate the parallel component of $\mathbf{Q}$ for the d-structure

$$\begin{aligned} \mathbf{Q}^{\parallel}(n_1, n_2, n_3, n_4, n_5) &= \hat{P}^{\parallel}(n_1\mathbf{e}_1 + n_2\mathbf{e}_2 + n_3\mathbf{e}_3 + n_4\mathbf{e}_4 + n_5\mathbf{e}_5)\frac{2\pi}{a} \\ &= (\mathbf{e}_1, \mathbf{e}_2, \mathbf{e}_3, \mathbf{e}_4, \mathbf{e}_5)\left[D(P^{\parallel})(n_1, n_2, n_3, n_4, n_5)^T\right]\frac{2\pi}{a} \\ &= \left[(n_1c_1 + n_2c_2 + n_3c_3 + n_4c_4)\frac{2\pi}{\sqrt{5}a}\right]\mathbf{e}_1 \\ &\quad + \left[(n_1s_1 + n_2s_2 + n_3s_3 + n_4s_4)\frac{2\pi}{\sqrt{5}a}\right]\mathbf{e}_2 \\ &\quad + \left[n_5\frac{2\pi}{c}\right]\mathbf{e}_5 \\ &\equiv Q_x^{\parallel}\mathbf{e}_1 + Q_y^{\parallel}\mathbf{e}_2 + Q_z^{\parallel}\mathbf{e}_5, \end{aligned} \tag{2.44}$$

$$Q^{\parallel} = |\mathbf{Q}^{\parallel}| = \left(Q_x^{\parallel\,2} + Q_y^{\parallel\,2} + Q_z^{\parallel\,2}\right)^{1/2}. \tag{2.45}$$

For example,[101] two peaks are assigned to the indexes (0,3,5,3,1) and (2,8,10,5,0), and have values of $Q^{\parallel}$ respectively 3.064 Å^{-1} and 5.080 Å^{-1}. The above equations give

$$\begin{aligned} \frac{370.9}{a^2} + \frac{39.48}{c^2} &= 3.064^2 \\ \frac{1342}{a^2} + 0 &= 5.080^2. \end{aligned}$$

Solving these two equations gives a=7.211 Å and c=4.184 Å.

2.6.2 Takeuchi scheme

In the Takeuchi scheme,[99] five reciprocal vectors $\mathbf{b}_i^{\parallel}$ (i=1, ..., 5) are arranged so that they make an angle of $2\pi/5$ between the adjacent ones in a plane perpendicular to the vector $\mathbf{b}_6^{\parallel}$. For the first five vectors, $|\mathbf{b}_i^{\parallel}|$ is taken to be equal to $2\pi/a$, whereas the $|\mathbf{b}_6^{\parallel}|$ is equal to $2\pi/c$. Therefore, one can make use of equations similar to Eqs. (2.44) and (2.45) to calculate $Q^{\parallel}$.

For the two schemes described above, two Fortran programs D1INDEX.FOR and D2INDEX.FOR[93] were written for indexing the XRD patterns of d-structures. In order to find out lattice constants a and c, the values of $Q^{\parallel}$ and the corresponding indexes have to be assigned to two chosen peaks.

Fig. 2.7 shows the XRD spectrum of the d-alloy $Al_{65}Co_{15}Cu_{20}$. The $Q^{\parallel}$ values of the peaks (00112) and (08 13 81) are respectively 2.038 and 0.875 Å^{-1}. Indexing the spectrum gives a=7.182 Å and c=4.166 Å.

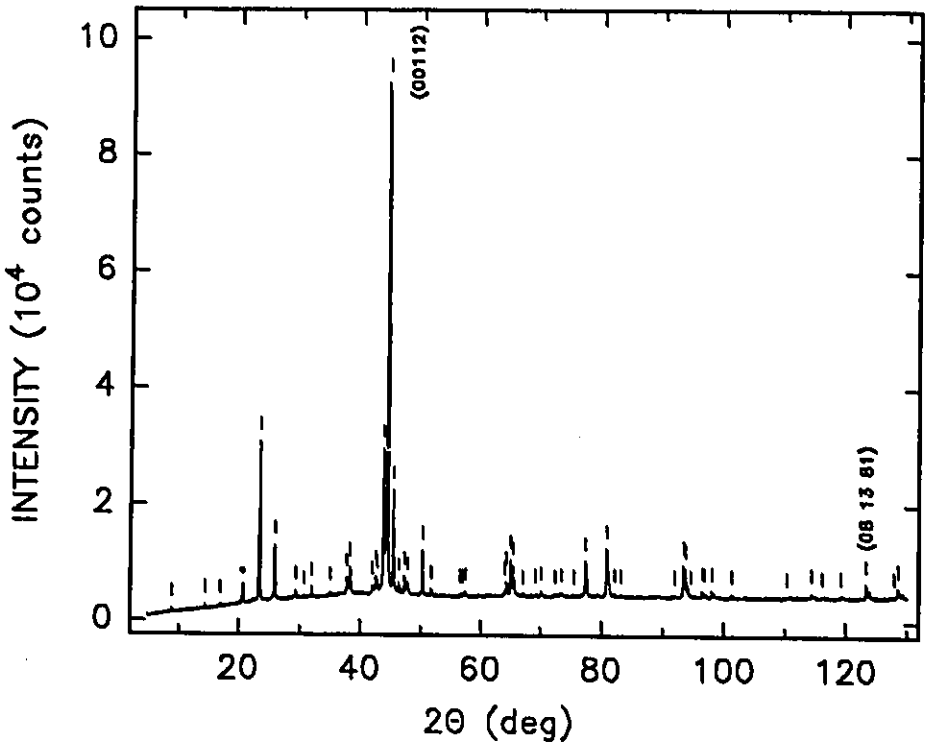

Figure 2.7: **XRD spectrum of the d-alloy $Al_{65}Co_{15}Cu_{20}$. The vertical lines above the Bragg peaks correspond to the positions calculated for the Cu$K\alpha_1$ radiation.**

2.7 Summary

This chapter can be summarized by noting that whereas the atomic structures of QC's in physical space are still being investigated, several models in $5D$ and $6D$ spaces are well developed for indexing the XRD patterns. Three Fortran programs were written in the course of the study for indexing the i- and d-structures using the often-used schemes. Detailed descriptions, equations, and matrixes appearing in this chapter are expected to be helpful for readers who are interested in indexing QC's or making comparisons of the indexing results from various publications.

Chapter 3

PHOTOEMISSION SPECTROSCOPY

In this chapter, the first section gives an introduction to the PES technique. The second section deals with the raw data correction. The remaining sections explain the photoemission from different physics perspectives, such as resonance, DOS and partial DOS (PDOS), pseudogap, spikiness, and core level shift. The PES spectra of *d*-alloy $Al_{65}Co_{15}Cu_{20}$ were taken[83] as examples in order to illustrate the process of analysis of the PES spectra.

3.1 Photoemission spectroscopy technique

Photoemission can be summarized as a photon-in and electron-out[102] experiment (Fig. 3.1). A monochromatic photon beam in the UV or X-ray range impinges on a sample and induces the emission of the photoelectrons. Then the photoelectrons are collected and analyzed by an electron energy analyzer. The typical operation mode of a PES experiment is an *energy distribution curve* (EDC) mode. The EDC spectrum

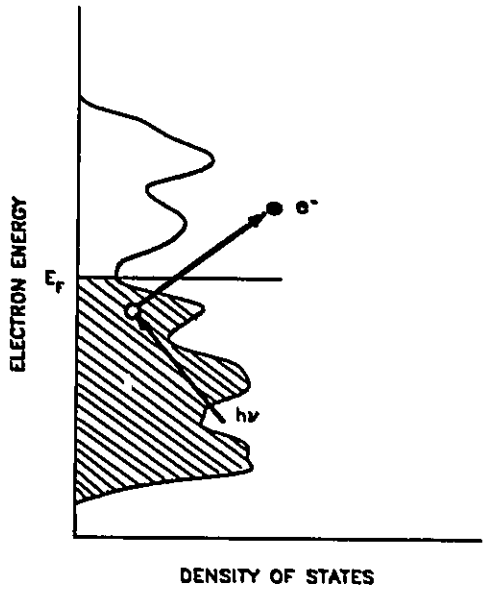

Figure 3.1: **Photoemission spectroscopy in a bird's eye view.**

represents the photoelectron intensity as a function of photoelectron energy. It is obvious that a PES spectrum must reflect the population of the electronic states of the sample.[102] Intuitively, when a photon of energy $h\nu$ is absorbed, its energy is transferred to an electron (Fig. 3.1) which "jumps" from its initial state at binding energy (E_B) to an excited state above the vacuum level, with kinetic energy[102]

$$E_K = h\nu + E_B - \phi, \tag{3.1}$$

where ϕ is the work function of the sample. Because of the energy conservation relation in Eq. (3.1), it may be expected that the distribution of the excited photoelectrons will reproduce the structures of the distribution of occupied states, i.e., the occupied density of states.[102] The PES spectrum of the Cu metal (from Fig. 12 in Ref. [83]) in Fig. 3.2 confirms this intuitive picture. One can easily identify the narrow and completely filled Cu $3d$ band at around 3 eV below the E_F, and a wide, partially occupied conduction band of s character. This kind of information is extremely important and can not be

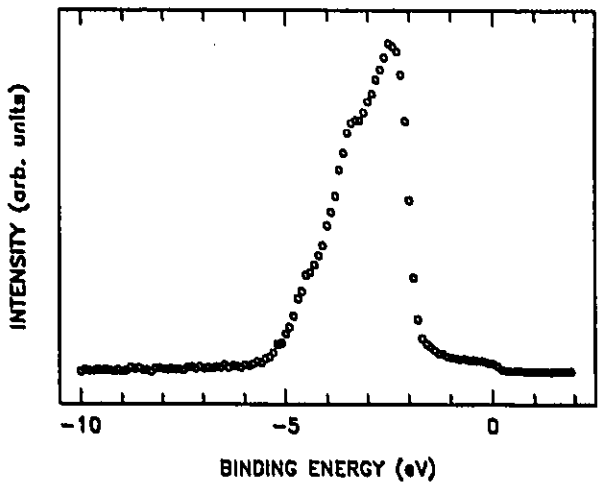

Figure 3.2: PES spectrum of Cu metal. The data were complied from Fig. 12 in Ref. [83].

obtained in such a direct way by any other technique.[102]

When measuring photoelectrons which are excited with a continuously tunable light source, which is possible by using synchrotron radiation, one has the option of varying either the E_K window of the electron analyzer and keeping the $h\nu$ fixed, or of varying $h\nu$ and setting E_K to a fixed value. There are further possibilities for combined variations of $h\nu$ and E_K.[103] Two of them were employed in this project since the synchrotron radiation source was used to collect most of PES spectra. There is a need for guidelines for the interpretation of the spectra obtained in these different modes. For this purpose, the result of a simplified one-electron density of states model[103] is described below.

The number of photoelectrons excited to a final-state energy characterized by E_K is given by[103]

$$N(E_K, h\nu) \propto \int d^3\mathbf{k} M_{if}(\mathbf{k}) \delta[E_f(\mathbf{k}) - E_i(\mathbf{k}) - h\nu] \delta[E_f(\mathbf{k}) - E_K]. \qquad (3.2)$$

The escape probability through the surface has been assumed to be independent of all variables.[103] The indexes i and f represent the initial and final states with energies E_i and E_f, respectively. Here E_i is equal to E_B in this thesis and E_f is equal to $(E_K +$

ϕ). $M_{if}(\mathbf{k})$ is the matrix element for dipole transitions between these states at the point $\mathbf{k}$ in the first Brillouin zone.[103] Under the simplifying assumption that $M_{if}(\mathbf{k})$ is also constant throughout the Brillouin zone and further that one deals with flat initial-state bands or has a breakdown of the k-selection rule, one can rewrite Eq. (3.2)[103]

$$N(E_K, h\nu) \propto M \cdot \rho_i(E_k - h\nu) \cdot \rho_f(E_K), \tag{3.3}$$

where ρ_i and ρ_f are initial- and final-state densities of the states, respectively. On the one hand, the k-selection rule, which allows only for direct transitions, will reduce the number of states contributing to ρ_i and ρ_f in Eq. (3.3). On the other hand, one can also make use of the k-selection rule to obtain more detailed information by using the so-called angle-resolved PES spectra measurements.

The three types of spectroscopies which may be employed can be interpreted depending on how the parameters E_K and $h\nu$ are varied[103] in Eq. (3.3):

- EDC spectroscopy, variation of E_K for a constant $h\nu$ gives joint information on ρ_i and ρ_f,
- CIS (Constant Initial-State) spectroscopy, synchronous variation of E_K and $h\nu$ such that $E_K - h\nu = E_B - \phi$=constant gives ρ_f, and
- CFS (Constant Final-State) spectroscopy, variation of $h\nu$ gives ρ_i.

The first two types of spectroscopies were studied extensively during the course of this research. Examples of EDC and CIS spectra will be presented in the following sections of this chapter and throughout the next chapter.

Most of the PES spectra were collected at room temperature on beamline U14A at the National Synchrotron Light Source at the Brookhaven National Laboratory. High energy-resolution UPS data obtained recently at the University of Nechâtel will be also presented.[84]

For the synchrotron-radiation-based spectra, $h\nu$ values between 35 and 150 eV were selected with a plane grating monochromator. The normal to the sample was at an angle 45° to both the photon beam and the axis of a PHI 15-255 precision electron-energy analyzer. The resulting overall resolution was about 0.4 eV. The samples were cleaned in the experimental vacuum chamber either by gentle mechanical abrasion *in situ* using an alumina scraper or by Ar sputtering. The surface cleanliness of the samples was frequently verified by monitoring the appearance of the oxide features in the PES spectra of the Al 2*p* core-level lines and/or of the valence bands.[74] The ambient pressure in the experimental chamber was in the high 10^{-11} Torr range. All the spectra presented here were obtained from at least two different regions of the samples studied, and were indistinguishable within the resolution of the experiment. The position of the Fermi level was determined with an accuracy of 50 meV by measuring the Fermi edge of an adjacent Al foil electrically connected to the samples.

For the UPS spectra, a He lamp was used as radiation light (He I: 21.1 eV, He II: 40.8 eV). The samples could be cooled down to about 13 K. They were cleaned by scraping *in situ*. The position of the Fermi level was determined with accuracy better than 1 meV by measuring the Fermi edge of Ag evaporated onto the studied sample. The resolution of an experiment was obtained from the fitting of the Fermi edge region of the Ag valence band to a linearly decreasing intensity multiplied by the Fermi-Dirac distribution function and convoluted with a Gaussian (the FWHM of the Gaussian defines the energy resolution). Resolutions better than 50 meV could easily be achieved. Fig. 3.3 shows a part of UPS spectrum around the Fermi edge for Ag evaporated on a sample of *i*-Zn-Mg-Y measured at a temperature of 13 K.[84] The solid line is a fit using the procedure mentioned above. The fit gives the energy resolution of 5.2±0.2 meV.

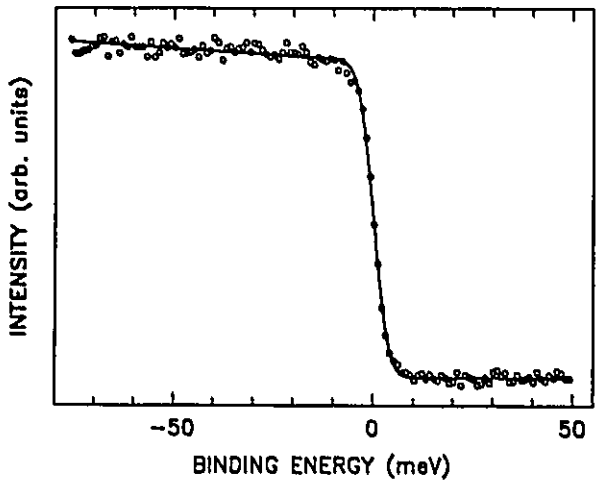

Figure 3.3: **The Fermi edge region of the valence band for Ag evaporated onto a sample of *i*-Zn-Mg-Y measured at T=13 K.[84] The solid line is the fit, as described in the text, which gives the energy resolution of 5.2±0.2 meV.**

3.2 Raw data correction

In order to meaningfully compare the intensities of the synchrotron-radiation-based PES spectra of a given sample, several corrections have to be taken into account.[83] First, all PES spectra presented here were corrected for the energy dependence of the electron transmission of the electron-energy analyzer. It was assumed that the transmission of the analyzer is inversely proportional to the kinetic energy of the electrons.[104] Next, the PES spectra were normalized to the time-dependent photon flux. The secondary-electron contribution was then subtracted by using the Shirley method.[105] In this method, the secondary-electron background intensity at each binding energy is assumed to be proportional to the total integrated signal at lower binding energies.

The first two corrections slightly modify the shape of the raw spectrum. The background subtraction causes the largest change (Fig. 3.4). These corrected spectra can be compared not only with respect to their shape but also in terms of their intensities.

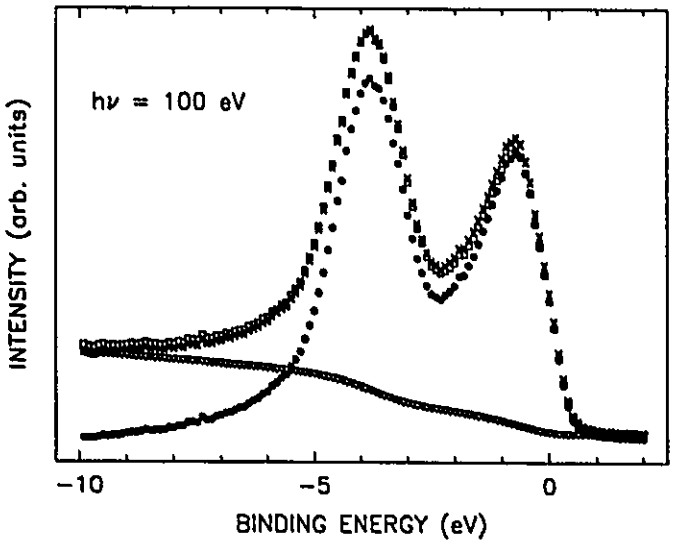

Figure 3.4: **Effect of various corrections on the valence-band spectrum of d-$Al_{65}Co_{15}Cu_{20}$ measured at $h\nu$=100 eV. (□) - the as-measured spectrum, (×) - the analyzer- and flux-corrected as-measured spectrum which was scaled to the most intense peak of the as-measured spectrum, (▽) - the secondary-electron contribution to the analyzer- and flux-corrected spectrum, (•) - the resultant spectrum after subtraction of the secondary-electron contribution.**

One has to be careful of the influence of photons with multiples of the selected energy. This is the case when using a synchrotron radiation source with a grating monochromator, especially when working at relatively low $h\nu$ values with a given refocussing mirror. The grating diffraction equation is $d(\sin a - \sin b)=n\lambda=n(hc)/(h\nu)$,[106] where d is the grating groove spacing, a and b are the incidence and diffraction angles with respect to the grating normal. All the three parameters are the same for the multiples of the selected $h\nu$. It turns out that the output beam is a mixture of photons with the first-order energy $h\nu$, second-order energy $2h\nu$, and so on. At the beamline U14A, the $h\nu$ ranges of interest are: 14-86 eV for the refocussing mirror 4 (P4), and 30-170 eV for the mirror 3 (P3).[106]

Suppose a beam of photons with $h\nu$=70 eV is selected using P3 to measure a valence band of an Al-based material. The interesting range of E_B for a valence band is from

-10 eV to $+3$ eV (Fig. 3.2). The corresponding range of E_K would be from 55 eV to 68 eV [see Eq. (3.1) and assume ϕ=5 eV]. The 140 eV-energy photons also are transmitted as the second-order diffraction. This $h\nu$ is high enough to excite the Al $2p$ electrons whose E_B=-72.6 eV. As a result, a peak appears around E_K=62.4 eV. In other words, the spectral intensity in the valence band at E_K=62.4 eV, i.e. E_B=-2.6 eV, results from the valence band excited by the 70-eV photons and from the Al $2p$ core level excited by the 140-eV photons. However, the P4 does not cause this problem because of its low flux at 140 eV.[106]

3.3 Photoemission resonance

Resonance photoemission is a particularly useful technique in determining the origin of atom-specific features in a valence band.[107] It is based on an enhancement of the σ of an outer-shell-electron as the excitation energy exceeds the threshold of an inner excitation. For TM atoms the resonance takes place at excitation energies near the $3p$ threshold. For example, the Co $3p \rightarrow 3d$ transition is expected to occur at $h\nu \approx 59$ eV.[108] For a TM atom with a ground state configuration of $3d^n$, resonance photoemission involves two processes.[83] The first process is the direct excitation from the occupied valence band, and can be expressed as

$$3p^6 3d^n + h\nu \rightarrow 3p^6 3d^{n-1} \epsilon_f, \tag{3.4}$$

where ϵ_f labels the state of a photoelectron to be detected. The other process involves a $3p$ electron being excited into an unoccupied $3d$ state, which then decays through an autoionization process. During the second process one $3d$ electron falls back to fill the $3p$ hole, thus transferring all its energy to a second electron which is emitted from the atom. This process can be described as

$$3p^6 3d^n + h\nu \rightarrow 3p^5 3d^{n+1} \rightarrow 3p^6 3d^{n-1} \epsilon_f. \tag{3.5}$$

Since the final state in Eq. (3.4) is identical to that in Eq. (3.5), there must be a quantum interference between the two processes. Thus, when $h\nu$ is swept through the Co $3p \rightarrow 3d$ threshold, the TM $3d$-derived features resonate, i.e., they are enhanced or suppressed.

The line shape $I(h\nu)$ of the resonance described by Eqs. (3.4) and (3.5) can be characterized by the Fano profile[107]

$$I(h\nu) = I_0(h\nu)\frac{(\epsilon + q)^2}{1 + \epsilon^2} + I_{nr}(h\nu), \tag{3.6}$$

where $I_0(h\nu)$ is the nonresonant Co $3d$ emission, $I_{nr}(h\nu)$ is a noninterfering background contribution, q is Fano's asymmetry parameter, and $\epsilon = 2(h\nu - E_R)/\Gamma$ is the reduced energy expressed in terms of the resonant energy (E_R), and FWHM (Γ). A linear background $I_{nr}(h\nu)$ was assumed during the fitting throughout the project.

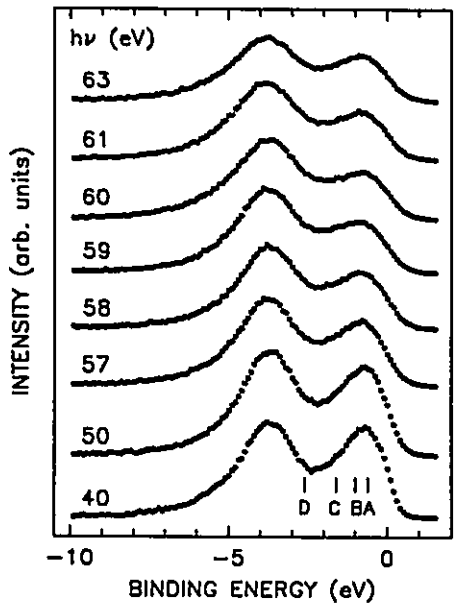

Figure 3.5: **Valence bands of d-$Al_{65}Co_{15}Cu_{20}$ measured for different $h\nu$ values around the Co $3p \rightarrow 3d$ transition. A, B, C, and D identify positions for which CIS spectra were measured (Fig. 3.7).**[83]

It can be seen in Fig. 3.5 that,[83] as $h\nu$ increases, the relative intensity of the peak at $E_B \approx -0.7$ eV with respect to the peak at $E_B \approx -3.7$ eV decreases first, reaches its

minimum at $h\nu$=60 eV, and then starts to increase for higher values of $h\nu$. Since in the vicinity of the Co $3p \rightarrow 3d$ transition the changes of σ with $h\nu$ are very small, the suppression of the −0.7 eV feature at $h\nu$=60 eV indicates that it is mainly of the Co $3d$ character.

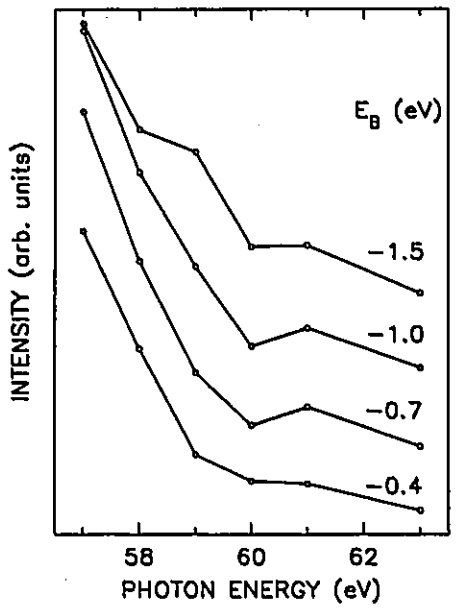

Figure 3.6: **CIS spectra for the indicated E_B values. The spectra were calculated from the PES spectra in Fig. 3.5, as described in the text. The solid lines are guides for the eye.**[83]

A resonance photoemission experiment can be performed in the CIS mode.[107] The CIS spectra represent the dependence of the photoemission intensity on $h\nu$ for selected valence-band positions identified by their initial energy (E_B). These spectra can show more clearly the photoemission intensity variations due to resonance. A CIS spectrum can be obtained by two different methods.

The first method involves generating the CIS spectra directly from the valence-band spectra measured for different $h\nu$. Such CIS spectra can be obtained from the valence bands in Fig. 3.5 by plotting the intensity at a given E_B versus $h\nu$ (Fig. 3.6). The

CIS intensity was calculated as an average of five PES intensity values around a given E_B in order to diminish possible CIS intensity fluctuations. One can see (Fig. 3.6) that the resonance occurs for $h\nu$ values around 60 eV and that it is strongest for the E_B values between -0.7 and -1.0 eV. This corresponds to the peak position of one of the two features in Fig. 3.5. It confirms that the peak in Fig. 3.5 close to E_F is predominantly of the Co $3d$ character. The generated CIS spectra (Fig. 3.6) consist of a small number of the experimental points (limited by the number of the PES valence band spectra at different $h\nu$ values). Therefore these spectra do not lend themselves to a more quantitative analysis.

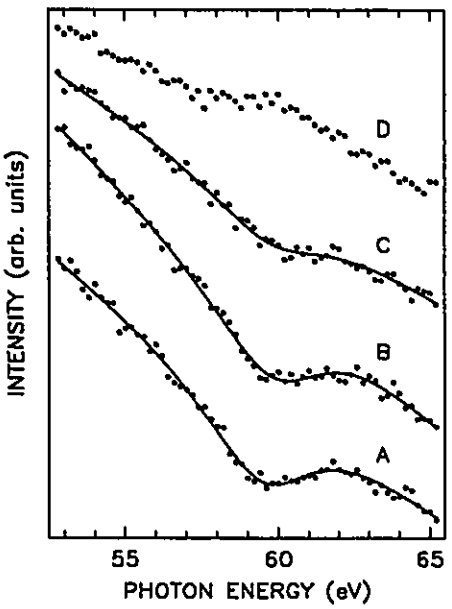

Figure 3.7: **CIS spectra measured for the valence band positions A, B, C, and D in Fig. 3.5, which are identified here by the same letters. The solid line is a fit to a Fano profile and a linear background [Eq. (3.6)] with parameters given in Table 3.1.**[83]

The CIS spectra can be also measured by a synchronous scanning of the $h\nu$ and E_K. Such spectra for the E_B values corresponding to the positions denoted by A, B, C, and D in Fig. 3.5 are shown in Fig. 3.7. One can clearly see a minimum for $h\nu$ around 60

eV. The parameters obtained from the fit using Eq. 3.6 are given in Table 3.1.

Table 3.1: **Parameters obtained by fitting the CIS spectra in Fig. 3.7 to the Fano line shape [Eq. (3.6)] for the E_B values corresponding to the positions A, B, and C indicated in Fig. 3.5.**

Label	E_B (eV)	I_0	E_R (eV)	q	Γ (eV)
A	−0.6	86(3)	59.7(2)	0.22(7)	4.6(3)
B	−1.0	84(4)	60.2(2)	0.31(9)	4.7(3)
C	−1.6	43(4)	60.0(5)	0.17(2)	4.7(6)

Even though a good fit of the CIS spectra was obtained (Fig. 3.7), the fitted parameters are correlated and therefore caution is required in their physical interpretation. The E_R values (Table 3.1) are close to the corresponding E_B of the Co 3p core level.[108] A relatively broad character of the resonance is reflected in the large value of Γ. The strongest resonance occurs between E_B=−0.6 eV and E_B=−1.0 eV and it extends up to E_B=−1.6 eV. The fact that the resonance takes place in a rather broad E_B region can be interpreted as evidence of hybridization between the Co 3d and Al sp and/or Cu 3d states. It is concluded that the peaks at E_B=−0.7 and −3.7 eV in the valence band of d-$Al_{65}Co_{15}Cu_{20}$ (Fig. 3.5) are respectively due to the Co 3d and Cu 3d states.

3.4 Partial density of states

It is now widely accepted that PES valence bands measured at $h\nu$>40 eV represent the initial DOS weighted by frequency-dependent dipole matrix elements and by the $\sigma(h\nu)$ values of various s, p, d, and f states.[109] To a good approximation, it can be

assumed that the matrix elements do not change significantly over the width of the valence bands. Thus the measured PES valence bands, when corrected for experimental factors and for inelastically scattered electrons, are proportional to the DOS modulated by the σ values.

Before synchrotron radiation became available as a tunable excitation source, the *partial* spectral weights of a given state of a given element in an alloy were determined almost exclusively using the SXE technique. The use of synchrotron-radiation-based PES allows one also to determine PDOS for some orbitals.[110]

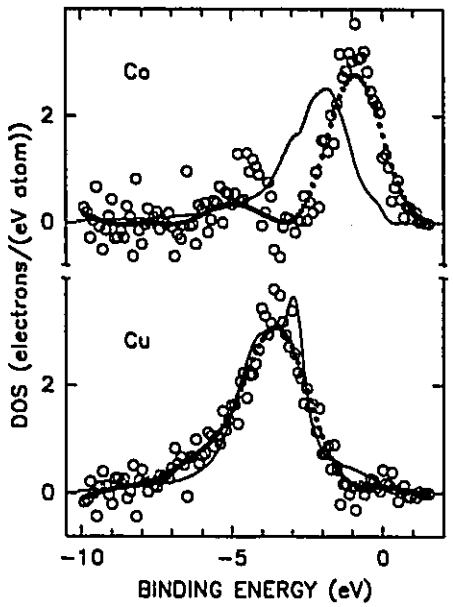

Figure 3.8: **PDOS's of the Co and Cu 3*d* states in *d*-$Al_{65}Co_{15}Cu_{20}$ (o) obtained from the $h\nu$=60 eV and 63 eV valence bands in Fig. 3.5, and later smoothed (•). The broadened theoretical DOS (solid line) is from Ref. [111], as described in the text.**

By taking the difference between the on-resonance ($h\nu$=63 eV) and off-resonance ($h\nu$=60 eV) valence bands in Fig. 3.5 and scaling to the heights of the peaks, one obtains the PDOS's of the Co 3*d* and Cu 3*d* character respectively (open circles in Fig. 3.8). As the difference spectra had a large scatter, they were smoothed (closed circles in Fig. 3.8)

to allow a better comparison with the theoretical PDOS's of the Co and Cu 3d states.[111]

The electronic structure of the hypothetical approximant $Al_{60}Co_{14}Cu_{30}$ of a *d*-alloy Al-Co-Cu has been calculated in a recent study.[111] The theoretical DOS, which was kindly provided by Prof. T. Fujiwara, exhibits a well pronounced pseudogap at E_F.[111] In order to make a meaningful comparison between the theoretical and experimental PDOS's, the former has to be appropriately broadened to account for the lifetime broadening effects inherent to the PES technique and for the finite resolution of a PES experiment. The theoretical Co 3*d* and Cu 3*d* DOS were first multiplied by the Fermi-Dirac function at room temperature, then convoluted with a Lorentzian to account for the lifetime broadening, and finally convoluted with a Gaussian to account for the instrumental broadening. The Lorentzian FWHM was taken in the form $\Gamma_L^0(|E_B| - E_F)^2$ (Ref. [112]) which is predicted by Fermi liquid theory.[113] The Γ_L^0 parameter, which fixes the scale of the broadening, was chosen to be 0.02 eV^{-1} since for this value one obtains a good agreement between the theoretical and experimental widths of the Cu 3*d* DOS. The Gaussian FWHM was 0.4 eV. As can be seen from Fig. 3.8, there is a striking disagreement between the theoretical and experimental Co 3*d* DOS.

3.5 Minimum of density of states at the Fermi level

In order to compare the theoretical valence-band spectrum of the approximant of the *d*-alloy Al-Co-Cu with an experimental spectrum of the *d*-alloy $Al_{65}Co_{15}Cu_{20}$ at $h\nu$=100 eV, the theoretical PDOS's of the Al, Co, and Cu for different angular momenta[111] were first multiplied by the corresponding σ values[114] and normalized for the numbers of the electrons in the valence band.[115] Their sum (Fig. 3.9), which differs only slightly from the total theoretical DOS of an approximant of the *d*-alloy,[111] represents the theoretical PES valence band which would be expected in a hypothetical PES experiment with an infinitely high energy resolution and no lifetime broadening effects. A distinct and wide

pseudogap at E_F (Fig. 3.9) is predicted.[111]

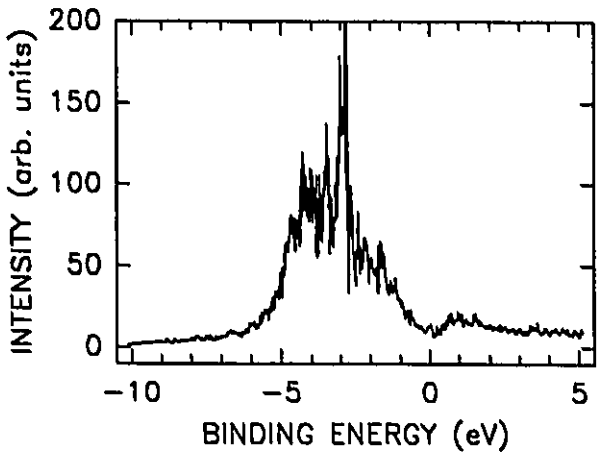

Figure 3.9: **Theoretical $h\nu$=100 eV PES valence band of a d-Al-Co-Cu alloy which was obtained by summing the theoretical PDOS's of the Al, Co, and Cu associated with different angular momenta from Ref. [111] weighted by the corresponding σ values from Ref. [114] and by the composition and the number of electrons.**[115]

The theoretical PES valence band in Fig. 3.9 was next broadened in the same way as described in §3.4 and compared with the valence band of d-$Al_{65}Co_{15}Cu_{20}$ measured at $h\nu$=100 eV (Fig. 3.10). A wide pseudogap at E_F predicted by theory[111] is clearly not present in the experimental valence band (Fig. 3.10). Furthermore, even by allowing for the difference in composition between the approximant $Al_{66}Co_{14}Cu_{30}$ and d-$Al_{65}Co_{15}Cu_{20}$, the theoretical Co 3d spectral weight is much smaller than the weight observed experimentally (Fig. 3.11).

It is useful to compare the valence bands of d-alloys d-$Al_{65}Co_{15}Cu_{20}$ and $Al_{70}Co_{15}Ni_{15}$ with the valence bands of their constituent elements (Fig. 3.11). It can be noticed that there is a clear shift of the Cu 3d spectral weight in d-$Al_{65}Co_{15}Cu_{20}$ away from E_F as compared with the corresponding spectral weight in pure Cu (Fig. 3.11). Such a shift is expected to result in a decrease of the Cu 3d contribution to the DOS(E_F). A similar shift is not observed for the Co and Ni 3d spectral weights (Fig. 3.11). Consequently,

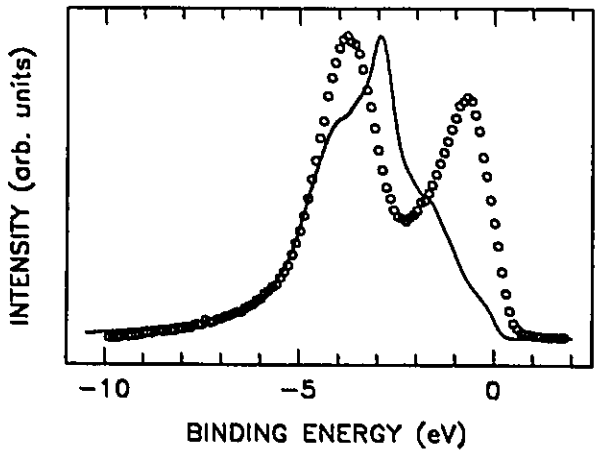

Figure 3.10: **Comparison between the valence band of d-$Al_{65}Co_{15}Cu_{20}$ measured at $h\nu$=100 eV (o) and the broadened theoretical PES valence band (solid line) from Fig. 3.9, as described in the text.**

one can anticipate a non-negligible contribution of the Co and Ni 3d-like states to the DOS(E_F) for the d-$Al_{65}Co_{15}Cu_{20}$ and $Al_{70}Co_{15}Ni_{15}$ alloys.

The Al sp states are expected to spread throughout the valence bands of d-alloys $Al_{65}Co_{15}Cu_{20}$ and $Al_{70}Co_{15}Ni_{15}$. However, this cannot be detected clearly in the measured spectra due to the small σ values of Al s and p orbitals.[114] These states contribute to a broad spectral weight below E_B=−6 eV, where the contributions from the Co, Cu, and Ni 3d-derived states are relatively small. This spectral weight could be also caused by surface oxidation.[74] This possibility, however, can be excluded as the surface cleanliness was carefully monitored during the PES experiments.

It can be concluded that the PES data presented here are conclusive evidence for the lack of a pseudogap at E_F in the two d-alloys of high structural quality. This can be interpreted as evidence that the Hume-Rothery mechanism does not play an important role in the stability and transport properties of d-alloys. This finding agrees with the suggestion based on the results of the recent optical conductivity[39] and the plane-wave model[118] studies, and is at variance with the interpretation of the electronic transport

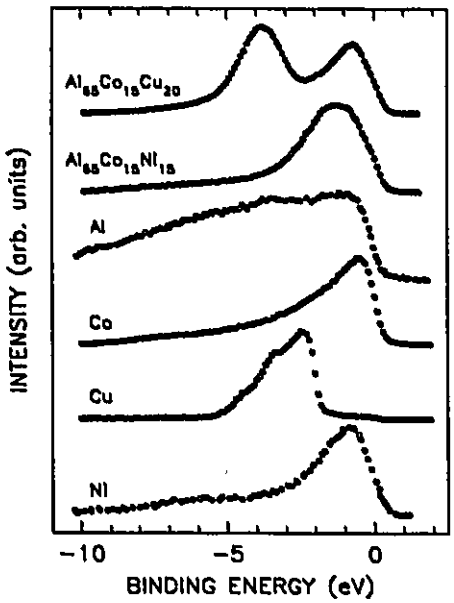

Figure 3.11: **Comparison of valence bands of d-alloys $Al_{65}Co_{15}Cu_{20}$ and $Al_{70}Co_{15}Ni_{15}$ with the valence bands of Al (Fig. 2 in Ref. [116]), Co, Cu (the raw PES spectrum was kindly provided by T.-U. Nahm and S.-J. Oh; the secondary electron contribution was subtracted from the original spectrum), and Ni (Fig. 4a in Ref. [117]; the secondary-electron contribution was subtracted from the original spectrum) metals. All valence bands were measured at $h\nu$=100 eV except for the valence band of the Al metal which was measured with Mg $K\alpha$ radiation (1253.6 eV). The spectra were normalized to give a constant height between the maximum and minimum recorded count.**

data[34, 35, 37, 40] and the prediction based on the energy-band calculations.[111]

The lack of a pseudogap at E_F in d-alloys means that there is a fundamental difference between their electronic structure and that of i-alloys in which this pseudogap seems to exist.[1, 3, 4, 8, 9, 49, 52, 53] Therefore, one has to consider other unconventional mechanisms to account for the unusual physical properties of d-alloys.

3.6 Fine structure of density of states

The notion of a structure-induced pseudogap is believed to be a *generic* property of QC's. It is theoretically predicted for both *i*-alloys[52, 53] and *d*-alloys.[111] But this prediction seems to be realized only in *i*-alloys.[1, 3, 4, 8, 9, 49] It is not, however, a *specific* property distinguishing QC's from the periodic or aperiodic phases because such a pseudogap was shown to be also present in some amorphous[119] or c-materials.[120, 121] A property which, according to some electronic structure calculations,[52, 53, 111] is specific only to QC's is the fine structure (spikiness) of their DOS (Fig. 3.9) resulting from a large number of non-degenerate flat bands.

Although the spikiness is predicted to be attenuated[111] in the *d*-Al-Co-Cu alloys in comparison to the *i*-alloys by the effect of the periodic direction, it is still clearly visible, especially in the vicinity of the Cu 3*d* peak (Fig. 3.9).[111] The width of a spiky peak is predicted[53, 111] to be of the order of 0.01-0.02 eV. The valence bands of *d*-alloys $Al_{65}Co_{15}Cu_{20}$ and $Al_{70}Co_{15}Ni_{15}$ presented here show no evidence for the presence of such spikes. These spikes have also not been detected directly in other spectroscopic measurements of QC's.[5, 10, 49, 74]

There are several possible explanations of the failure to detect these spikes in experiment (provided that they indeed exist). Assuming a hypothetical case of a PES experiment with no lifetime broadening, an energy resolution better than about 0.1 eV is required (left panel of Fig. 3.12) to detect the spikes. In a real PES experiment, lifetime broadening effects are present (§3.4) and they smear out even further (especially far from E_F) the fine features in the DOS (right panel of Fig. 3.12). It can be concluded that the predicted[111] DOS spikiness can be observed with the PES experiments of the highest energy resolution ($\leq$20 meV), and *only in the vicinity* of E_F.

The most recent high-resolution UPS experiments,[84] which are discussed in the next chapter, do not show any evidence for the spikiness. SXE spectroscopy is not suitable for

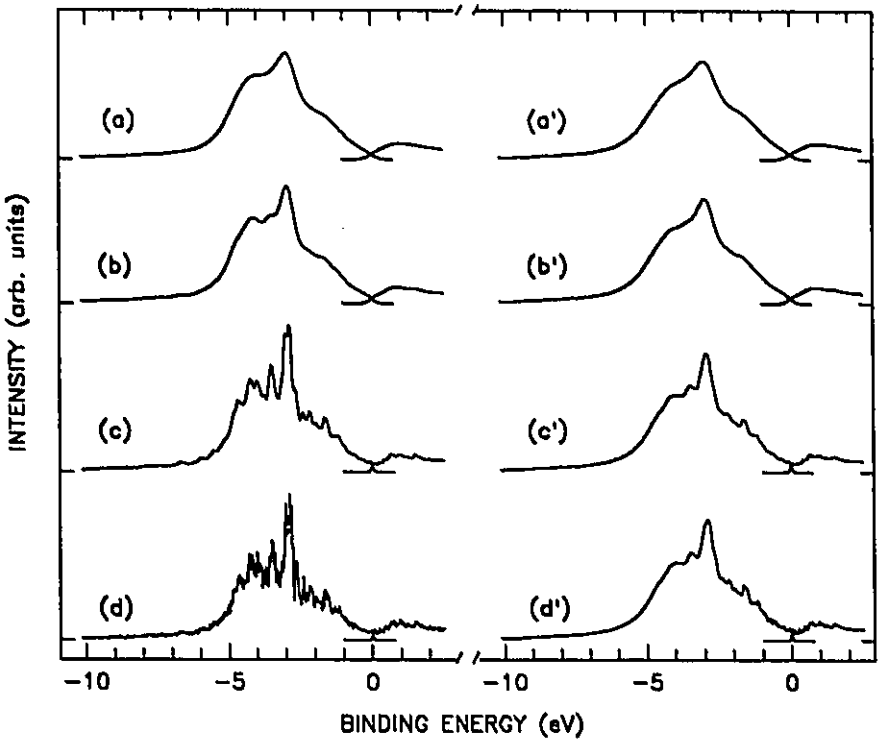

Figure 3.12: **Left panel: Theoretical PES spectrum from Fig. 3.9 multiplied by the Fermi-Dirac distribution function at room temperature and convoluted with a Gaussian of the FWHM equal to (a) 0.6, (b) 0.4, (c) 0.1, and (d) 0.02 eV. Right panel: Theoretical PES spectrum from Fig. 3.9 multiplied by the Fermi-Dirac distribution function at room temperature and convoluted with a Lorentzian of the FWHM equal to $\Gamma_L^0(|E_B| - E_F)^2$, where Γ_L^0=0.02 eV^{-1}, and with a Gaussian of the FWHM equal to (a') 0.6, (b') 0.4, (c') 0.1, and (d') 0.02 eV.**

detecting such spikes because of the severe broadening effects[5] around the E_F inherent to this technique.

3.7 Core level shift

The core level line shape can be best expressed by the Doniach-Šunjić profile[122, 123]

$$I(E) = \frac{\Gamma(1-\alpha)\cos\{\pi\alpha/2 + (1-\alpha)\arctan[(E-E_0)/(\Gamma/2)]\}}{[(E-E_0)^2 + (\Gamma^2/4)]^{(1-\alpha)/2}}, \qquad (3.7)$$

where Γ denotes the gamma function, α is the asymmetry parameter, Γ is the FWHM of the corresponding Lorentzian function which takes into account the finite hole-state lifetime effect, E_0 is the peak position, and E is the energy which may be kinetic or binding energy. When α=0, a Lorentzian is obtained. Similarly to the case of a valence band, the line shape should be convoluted with a Gaussian function in order to take into account the finite instrumental resolution. The spectrum resulting from Eq. (3.7) is shown in Fig. 3.13

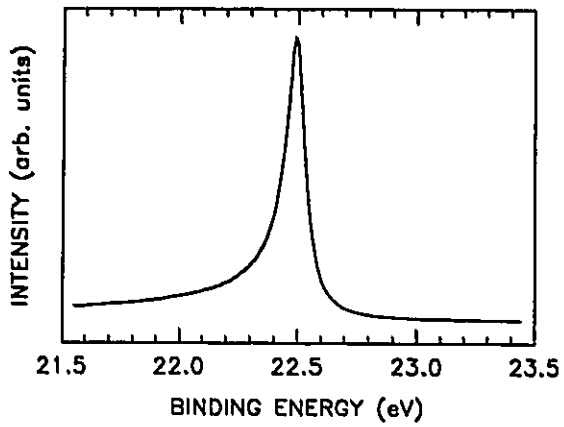

Figure 3.13: **Doniach-Šunjić line shape with α=0.2, Γ=0.04 eV, and E_0=22.5 eV.**

The Al $2p$ core-level lines in Al metal and in d-alloys $Al_{65}Co_{15}Cu_{20}$ and $Al_{70}Co_{15}Ni_{15}$ are compared in Fig. 3.14. One can notice that the Al $2p_{1/2}$ and $2p_{3/2}$ lines are separated in the Al metal (inset of Fig. 3.14), but they overlap in the d-alloys. The separation of the Al $2p_{1/2}$ and $2p_{3/2}$ lines in the Al metal determined from a fit using the two Doniach-Šunjić profiles [Eq. (3.7)] convoluted with a Gaussian (inset of Fig. 3.14) is 0.41(1) eV. This is in good agreement with the value of 0.42 eV reported in the literature.[124]

The Gaussian FWHM obtained from the fit was 0.418(7) eV. This value, together with the observation of the Al $2p_{1/2}$ and $2p_{3/2}$ components in the Al metal, confirms that the overall resolution of the recorded PES spectra is about 0.4 eV. The main result

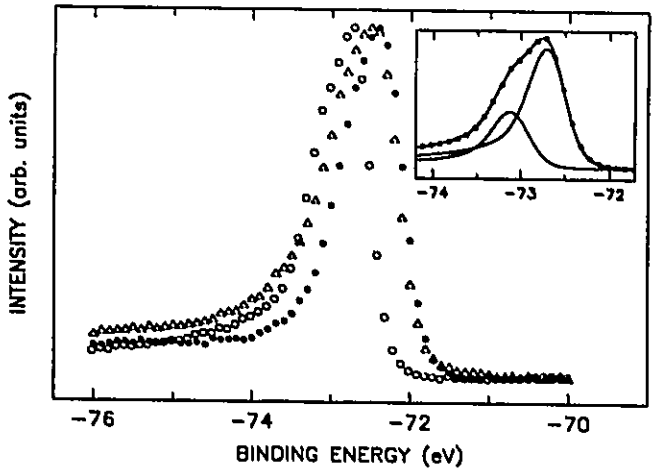

Figure 3.14: **Al $2p$ photoemission lines of the Al metal (o) and d-alloys $Al_{65}Co_{15}Cu_{20}$ (•), and $Al_{70}Co_{15}Ni_{15}$ (△) measured at $h\nu$=100 eV. The lines were normalized to give a constant height between the maximum and minimum recorded count. The inset shows the fit (solid line) of the Al $2p$ line of the Al metal with two Doniach-Šunjić profiles [Eq. (3.7)] corresponding to Al $2p_{1/2}$ and $2p_{3/2}$ core levels, which are also shown, convoluted with a Gaussian.**

obtained from Fig. 3.14 is the observation of the shift of E_B of the Al $2p$ line in the d-alloys $Al_{65}Co_{15}Cu_{20}$ and $Al_{70}Co_{15}Ni_{15}$ respectively by 0.36(3) and 0.30(3) eV towards lower $|E_B|$ values with respect to Al metal.

There are only a few reports of shifts of the core-level lines in QC's with respect to pure elements and/or to other c-alloys. Ederer et al.[64] reported the chemical shifts of 0.2 eV between the Al-Mn alloys of different crystal structures and pure Al, and of less than 0.1 eV between the Al-Mn alloys of c- and i-structure. Matsubara et al.[68] found a 0.4 eV shift of the Al $2p$ and Li $1s$ lines towards higher $|E_B|$ values in i-$Al_{55}Li_{35.8}Cu_{9.2}$ with respect to the Frank-Kasper c-alloy $Al_{54}Li_{36.8}Cu_{9.2}$. The shift of $|E_B|$ of the Al $2p$ line in i-$Al_{70}Pd_{20}Mn_{10}$ with respect to a pure Al metal was 0.27(10) eV (§4.1 and Ref. [10]). The values of the observed shifts are small and are comparable to those observed in c-alloys.[125] The interpretation of the shift of E_B is complicated by the fact that it consists of contributions due to chemical, configuration, and relaxation shifts.[126] These

contributions are difficult to evaluate theoretically even for simple binary alloys.[126]

3.8 Summary

This chapter introduces the PES technique both in the theoretical and experimental aspects. Based on Eq. (3.3), §3.1 presents a simple one-electron model which gives a clear picture of the PES operation modes: EDC, CIS and CFS. §3.2 explains the raw data corrections and indicates that one has to be aware of the influence of the higher-order-energy photons when using the synchrotron radiation source. PES resonance can be described by Eq. (3.6) and has been proven to be a useful method to explore the electronic structures of the solids. By using the synchrotron radiation source, PDOS's of d- and f-electrons can be determined from the spectra measured at different $h\nu$ values. When comparing a theoretical spectrum with an experimental one, lifetime broadening and instrumental resolution broadening have to be taken into account by convoluting the theoretical spectrum with Lorentzian and Gaussian functions. A pseudogap is one of the most important issues of QC's because it is connected to the mechanisms of the stability and the high ρ in QC's. The predicted spikiness has not been detected in the high-resolution UPS measurements.[84] Whereas the PES spectra of d-alloys $Al_{65}Co_{15}Cu_{20}$ and $Al_{70}Co_{15}Ni_{15}$ are taken as examples in this chapter for describing the theory and the technique of PES, the spectra of other important QC's are discussed in the next chapter.

Chapter 4

RESULTS AND DISCUSSION

The first two sections of this chapter present the studies of the *i*-alloys $Al_{70}Pd_{20}Mn_{10}$[10] and $Al_{65}Cu_{20}Os_{15}$.[5] The topics discussed here are the XRD pattern indexing and the PES spectra. §4.3 describes the UPS spectra of *i*-$Al_{65}Cu_{20}Fe_{7.5}Ru_{7.5}$ measured with the ultrahigh energy resolution.[84] The last section compares the PES and UPS results of the spectra for *i*-alloys $Al_{65}Cu_{20}Md_{15}$ (Md=Os, Ru, Fe, and $Fe_{0.5}Ru_{0.5}$)[5, 74, 82, 84] and discusses the pseudogap, spikiness, and the resistivity behavior of the QC's.

4.1 *i*-Alloy $Al_{70}Pd_{20}Mn_{10}$

The stable *i*-alloy $Al_{70}Pd_{20}Mn_{10}$ was found in 1990.[127] It differs from other stable *i*-phases in that the samples are free of atomic disorder and phason strains even in the rapidly solidified state.[128] Furthermore, this phase exists in a wide composition range.[10] Structural studies with different techniques show that this phase forms in a perfect *i*-state.[101, 129–131] Therefore, this system is ideal for studies of its possible unusual physical properties.[10]

4.1.1 X-ray diffraction pattern

The XRD spectrum of the studied sample measured in the 2Θ range 6°-123° (Fig. 4.1) shows the presence of the many Bragg lines, the weaker of which are usually not observed in the spectra obtained with a scintillation detector. This increased sensitivity for the weak lines is due to the solid-state detector which has a higher counting efficiency (due to the elimination of a monochromator in the diffracted beam) and lower background count rate as compared to a conventional scintillation detector.

For clarity, only some of the detected i-peaks in Fig. 4.1 are labeled with integers. The vertical lines above all detected i-peaks correspond to the positions calculated for the Cu$K\alpha_1$ radiation. Notice the splitting of diffraction peaks for large 2Θ values due to $K\alpha_2$ radiation. The symbols (o) and ($_\nabla$) indicate the peak positions corresponding to the strongest peaks of the hexagonal Al_3Pd_2 and decagonal Al_4Mn second phases, respectively. The inset of Fig. 4.1 shows a part of the spectrum with low-intensity peaks.

The positions of all the detected Bragg lines corresponding to Cu$K\alpha_1$ radiation in terms of the angle $2\Theta_1$ and the wave number $Q_{expt}=4\pi \sin\Theta_1/\lambda$, as well as their relative intensities INT (normalized to a maximum of 100.0 for all detected i-peaks) and the Lorentzian full width at half maximum (FWHM) Γ_Q, were determined from the profile fitting using the procedure described by Schreiner and Jenkins.[91] The parameters for 61 detected i-peaks, whose positions are indicated by the vertical lines in Fig. 4.1, are presented in Table 4.1. Since there are several schemes employed to index the i-lines, the indexes obtained from the most often used schemes[95-97] (§2.4 and §2.5) are presented here in order to enable the reader to make convenient identification of the i-lines. The i-peaks are labeled with consecutive integers in column 1. These integers correspond to the vertical lines in Fig. 4.1. Q_{calc} in $Å^{-1}$ is the calculated Q value by taking the line number 17 as the reference line. I1 and I2 are the indexes (N/M) and (h/h', k/k', l/l') based on the indexing scheme of Cahn et al.[97] I3 and I4 are the in-

dexes corresponding to the indexing schemes of Elser[95] and Bancel et al.,[96] respectively. The symbol $n_1n_2n_3n_4n_5n_6/2$ in the I3 and I4 schemes is an abbreviation for the index $(n_1/2)(n_2/2)(n_3/3)(n_4/2)(n_5/2)(n_6/2)$. The fcc superlattice lines are those for which N=4n+3 in the I1 scheme and which have the indexes in the form $n_1n_2n_3n_4n_5n_6/2$ in the I4 scheme.

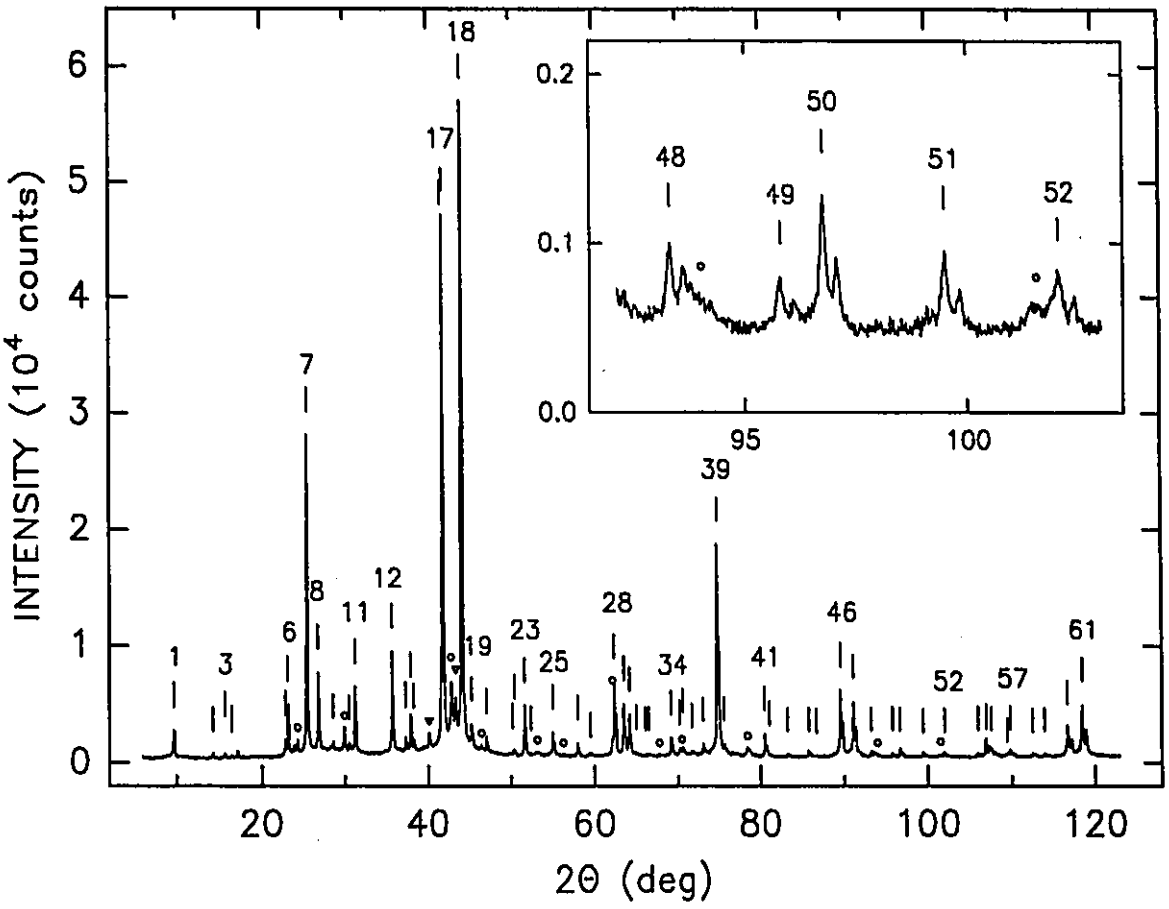

Figure 4.1: **XRD spectrum of *i*-alloy $Al_{70}Pd_{20}Mn_{10}$. The details are described in the text. The inset shows a part of the spectrum with low-intensity peaks.**[10]

Most of the observed Bragg lines can be indexed to the *i*-structure. It is noticeable that even the peaks with an intensity as small as 0.2% of the maximum intensity could

be detected and indexed to the i-structure. There is an excellent agreement between the observed Q_{expt} and theoretical Q_{calc} positions of the peaks (Table 4.1). Out of the 61 detected i-peaks, 60 are at the positions within ± 0.001 Å^{-1} and only one (peak number 53) within ± 0.002 Å^{-1} of the values calculated for the six-dimensional face-centered i-lattice. The peak widths (Table 4.1) are found to be limited by the instrumental resolution. The presence of the superlattice lines (Fig. 4.1 and Table 4.1), for which N in the N/M index[97] is equal to 4n+3 (the strongest superlattice line is the line number 7)[100], confirms[129, 132] that i-$Al_{70}Pd_{20}Mn_{10}$ has the six-dimensional face-centered-cubic Bravais lattice. The value of the six-dimensional cubic lattice constant a_{6D}=6.461 Å is in a good agreement with values in the literature.[129, 132]

All other weak nonicosahedral Bragg peaks in Fig. 4.1, except three, are identified with the peaks due to the presence of a small amount of the hexagonal Al_3Pd_2 (JCPDS file 6-0654) and decagonal Al_4Mn (JCPDS file 40-1080) alloys as the second phases. The presence of these alloys in the Al-Pd-Mn phase diagram has been observed earlier with electron microscopy techniques by Beeli et al. and Audier et al.[131] It is thus concluded that the studied sample is predominantly a single phase i-alloy.

Table 4.1: **Parameters characterizing the XRD pattern in Fig. 4.1, as described in the text.**[10]

No.	$2\Theta_1$	Q_{expt}	Q_{calc}	Γ_Q	INT	$I1$	$I2$	$I3$	$I4$
1	9.692	0.689	0.688	0.006	3.0	2/1	011000	100000	$21\bar{1}\bar{1}\bar{1}1$
2	14.269	1.013	1.013	0.010	0.6	3/3	101100	$11111\bar{1}$ /2	$33\bar{1}\bar{3}11$ /2
3	15.688	1.113	1.113	0.009	0.5	3/4	011100	111111 /2	$311\bar{1}\bar{1}\bar{1}$ /2
4	16.503	1.171	1.170	0.010	0.3	4/4	000200	110000	$2200\bar{1}1$
5	22.818	1.614	1.614	0.008	1.6	7/8	112100	$31111\bar{1}$ /2	$53\bar{1}\bar{1}33$ /2
6	23.172	1.638	1.639	0.007	6.9	6/9	011200	111000	110001
7	25.494	1.800	1.800	0.009	42.1	7/11	111200	311111 /2	$1111\bar{1}1$ /2
8	26.840	1.893	1.893	0.008	10.5	8/12	002200	111100	$1110\bar{1}0$
9	28.596	2.014	2.014	0.006	1.1	10/13	122100	111110	$2210\bar{1}0$
10	30.514	2.146	2.147	0.015	0.9	11/15	101300	$3311\bar{1}1$ /2	$53\bar{1}\bar{1}\bar{1}3$ /2
11	31.225	2.195	2.196	0.009	8.9	11/16	011300	331111 /2	$3311\bar{1}3$ /2
12	35.749	2.504	2.504	0.009	13.7	14/21	102300	211100	$2100\bar{1}1$
13	37.359	2.612	2.612	0.009	1.8	15/23	121300	333111 /2	$3311\bar{1}1$ /2
14	37.949	2.652	2.652	0.007	5.6	15/24	112300	$3331\bar{1}1$ /2	111111 /2
15	38.312	2.677	2.677	0.008	1.6	16/24	222200	211110	$210\bar{1}\bar{1}1$
16	41.636	2.899	2.899	0.008	4.9	19/28	013300	333311 /2	$531\bar{3}\bar{1}1$ /2
17	41.845	2.913	2.913	0.007	76.7	18/29	122300	211111	100000
18	44.107	3.063	3.063	0.007	100.0	20/32	002400	221001	110000
19	45.269	3.139	3.139	0.006	3.1	22/33	012410	221101	$2210\bar{1}1$
20	47.090	3.258	3.259	0.006	2.6	23/36	132300	533111 /2	$331\bar{1}\bar{1}1$ /2
21	50.227	3.462	3.462	0.006	0.6	27/40	103410	$53331\bar{1}$ /2	$551\bar{1}\bar{1}3$ /2
22	50.402	3.473	3.474	0.007	0.7	26/41	013400	222100	111101
23	51.641	3.553	3.553	0.007	8.3	27/43	113400	533311 /2	$311\bar{1}\bar{1}1$ /2
24	52.403	3.601	3.600	0.003	0.3	28/44	222400	311111	210001
25	55.034	3.769	3.768	0.009	3.6	31/48	112500	$5531\bar{1}1$ /2	$53\bar{1}\bar{1}\bar{1}1$ /2
26	58.025	3.956	3.956	0.009	1.7	34/53	122500	321111	220001
27	59.564	4.052	4.052	0.009	0.3	35/56	013500	553113 /2	$3111\bar{1}1$ /2
28	62.420	4.227	4.227	0.007	10.9	38/61	233400	322101	111000
29	63.492	4.292	4.292	0.007	8.6	39/63	123500	$5551\bar{1}1$ /2	$11111\bar{1}$ /2
30	64.149	4.331	4.331	0.007	6.4	40/64	242400	322111	111100

31	65.035	4.385	4.386	0.004	0.3	42/65	104500	322200	310$\bar{1}\bar{1}$1
32	66.091	4.448	4.448	0.006	0.2	43/67	333400	733331 /2	5311$\bar{1}$3 /2
33	66.498	4.472	4.472	0.008	0.2	43/68	114500	5553$\bar{1}$1 /2	3331$\bar{1}$1 /2
34	69.197	4.632	4.631	0.008	2.9	46/73	013600	332001	2110$\bar{1}$0
35	70.209	4.691	4.691	0.007	1.1	47/75	113600	753113 /2	331$\bar{1}\bar{1}\bar{1}$ /2
36	70.587	4.713	4.713	0.013	1.0	47/76	233500	733333 /2	111$\bar{1}$1$\bar{1}$ /2
37	71.702	4.777	4.777	0.012	0.4	50/77	213600	332111	320002
38	73.071	4.856	4.856	0.008	1.4	51/80	134500	7551$\bar{1}$1 /2	531$\bar{1}\bar{1}$3 /2
39	74.828	4.956	4.956	0.008	32.9	52/84	004600	332002	101000
40	75.654	5.002	5.003	0.005	0.9	54/85	253400	422111	221101
41	80.535	5.272	5.273	0.007	3.1	59/95	343500	755313 /2	311111 /2
42	81.144	5.305	5.305	0.003	0.3	60/96	224600	422211	210$\bar{1}$00
43	83.281	5.420	5.420	0.008	0.5	63/100	253500	755333 /2	5311$\bar{1}$1 /2
44	85.802	5.553	5.552	0.009	0.8	66/105	104700	432002	2111$\bar{1}$1
45	86.759	5.602	5.602	0.006	0.2	67/107	014701	775113 /2	3331$\bar{1}\bar{1}$ /2
46	89.614	5.748	5.748	0.008	10.6	70/113	124700	432112	110010
47	91.157	5.826	5.826	0.007	8.5	72/116	244600	433101	200000
48	93.282	5.931	5.931	0.007	0.8	75/120	015700	955313 /2	511$\bar{1}\bar{1}$1 /2
49	95.797	6.052	6.052	0.010	0.5	78/125	344601	433201	211001
50	96.751	6.097	6.098	0.008	1.4	79/127	125700	955333 /2	331$\bar{1}$11 /2
51	99.492	6.225	6.226	0.009	0.7	83/132	334700	975113 /2	531113 /2
52	102.036	6.341	6.341	0.009	0.5	86/137	364500	443101	310001
53	106.015	6.515	6.513	0.012	0.5	90/145	015800	522222	111110
54	106.975	6.556	6.556	0.009	2.7	91/147	115800	975115 /2	311$\bar{1}$1$\bar{1}$ /2
55	107.589	6.582	6.582	0.009	1.2	92/148	115801	443102	211000
56	109.452	6.659	6.659	0.016	0.4	95/151	355600	977311 /2	5331$\bar{3}\bar{1}$ /2
57	109.836	6.675	6.675	0.009	0.7	95/152	125810	9773$\bar{1}$1 /2	531$\bar{1}\bar{1}\bar{1}$ /2
58	112.517	6.783	6.783	0.008	0.5	98/157	225801	533211	221000
59	113.949	6.839	6.839	0.005	0.4	99/160	354700	977313 /2	31111$\bar{1}$ /2
60	116.714	6.944	6.944	0.008	4.6	102/165	235800	4441$\bar{1}$1	101010
61	118.464	7.009	7.008	0.008	7.8	104/168	464600	533212	111010

4.1.2 Resonant photoemission

To establish the main features in a valence band due to the Mn $3d$ states, the resonant photoemission effect can be employed.[107] For a transition metal (TM) the resonance occurs at excitation energies near the $3p$ threshold, which for the Mn $3p \rightarrow 3d$ transition occurs at about 47 eV. Resonance photoemission for Mn-containing alloys involves two processes:

$$3p^6 3d^5 + h\nu \rightarrow 3p^6 3d^4 \epsilon_f, \tag{4.1}$$

and

$$3p^6 3d^5 + h\nu \rightarrow 3p^5 3d^6 \rightarrow 3p^6 3d^4 \epsilon_f. \tag{4.2}$$

As a result, the Mn $3d$-derived features are enhanced or suppressed as the $h\nu$ is swept

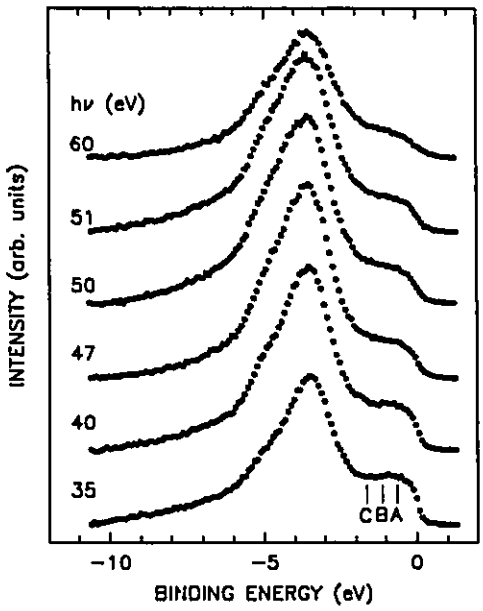

Figure 4.2: **Valence-band spectra of i-$Al_{70}Pd_{20}Mn_{10}$ for different $h\nu$ values around the Mn $3p \rightarrow 3d$ transition. A, B, and C identify positions for which CIS spectra were measured (Fig. 4.3).**

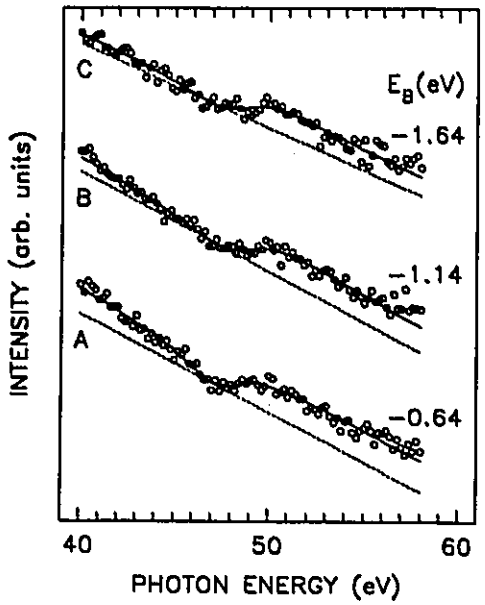

Figure 4.3: **CIS spectra for the valence-band positions A, B, and C in Fig. 4.2 that are identified here by the same letters and by their corresponding E_B values. The solid line is a fit to the Fano profile [Eq. (3.6)] and a linear background (shown by a dashed line), as described in the text. The parameters are given in Table 4.2.**

through the $3p$-$3d$ threshold. It can be seen in Fig. 4.2 that, as the $h\nu$ increases, the intensity of the E_B=−1.0 eV feature is slightly suppressed at $h\nu$=47 eV. This indicates that this feature may be predominantly due to the Mn $3d$-derived states.

The CIS spectra for the E_B values corresponding to the positions denoted by A, B, and C in Fig. 4.2 are shown in Fig. 4.3. One can clearly see the presence of resonance for $h\nu$ values around 47 eV. A linear background was assumed in the fit (dashed line in Fig. 4.3). The fitted parameters (Table 4.2) are strongly correlated and therefore caution is required in their physical interpretation. The strongest resonance occurs for E_B=−0.64 eV, but it is also present for other two E_B values, i.e., in the region of the valence band farther away from the E_F. The fact that the resonance takes place in a rather broad valence-band region can be interpreted as evidence of hybridization between

the Mn 3*d* and the Al *sp* and Pd 4*d* states. These seem to be consistent with the trend

Table 4.2: **Parameters obtained by fitting the CIS spectra in Fig. 4.3 to the Fano profile [Eq. (3.6)] for the E_B values corresponding to the positions A, B, and C indicated in Fig. 4.2.**

Label	E_B (eV)	I_0	E_R (eV)	q	Γ (eV)
A	−0.64	22.5(1.8)	47.5(3)	0.24(10)	3.7(6)
B	−1.14	15.8(1.8)	48.5(3)	0.60(12)	4.5(8)
C	−1.64	11.5(2.5)	48.6(5)	0.72(21)	4.0(1.2)

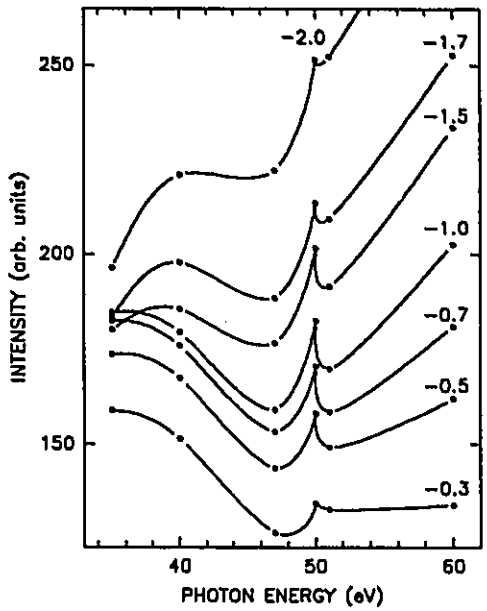

Figure 4.4: **CIS spectra for the indicated E_B values which were calculated from the PES spectra of Fig. 4.2 and corrected by the curve (*c*) from Fig. 4.5, as described in the text. The solid lines are guides for the eye.**

of q, which diminishes with E_B (Table 4.2). This trend, combined with the fact that a Fano line shape for small q values shows a more pronounced dip at $h\nu$ values just below the resonance maximum (antiresonance),[107] and with the results of a theoretical

model which predicts[133] that the d^{n-1} atomic-like final states in TM compounds tends to exhibit Fano-like resonance whereas the d^nL (L designates a ligand hole) final states corresponding to hybridized states show a more pronounced antiresonance behavior, seems to support the idea of hybridization between the Mn 3*d* and the Al *sp* and the Pd 4*d* states.

Fig. 4.4 shows the CIS spectra generated directly from the valence bands in Fig. 4.2 by plotting the height at a given E_B value versus the $h\nu$. The height was calculated as an average of five height values around a given E_B in order to remove the possible height fluctuations. To correct the CIS spectra for the effect of the $h\nu$ dependence of

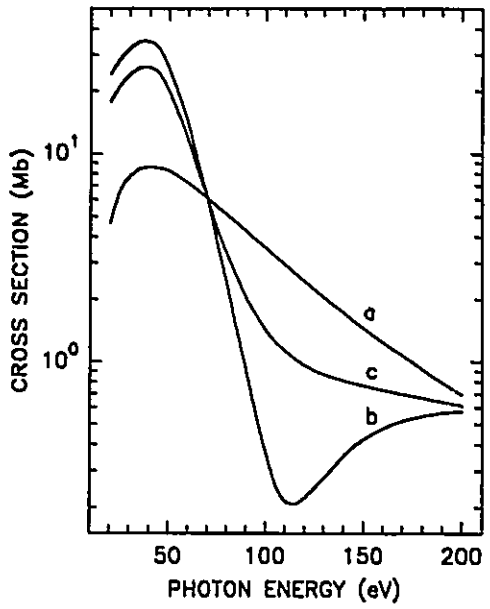

Figure 4.5: **Atomic subshell σ as a function of $h\nu$ for Mn 3*d* (*a*) and Pd 4*d* (*b*) orbitals. Data are compiled from Ref. [114]. Curve (*c*) is the weighted average of curve (*a*) and (*b*) with the weights corresponding to the Mn and Pd concentrations in $Al_{70}Pd_{20}Mn_{10}$. Note the logarithmic scale on the ordinate axis.**

the effective σ, they were divided by a weighted-sum of $\sigma_{Pd(4d)}$ and $\sigma_{Mn(3d)}$ [curve (*c*) in Fig. 4.5]. Fig. 4.4 shows clearly the presence of resonance at an energy corresponding

to the Mn $3p \rightarrow 3d$ transition. The occurrence of the strongest resonance for $E_B = -1.0$ eV is interpreted as evidence that the feature in the valence band at $E_B = -1.0$ eV is predominantly due to the Mn $3d$-derived states. The fact that the resonance takes place for a wide E_B range indicates that the Mn $3d$ and the Al sp and Pd $4d$ states are hybridized.

4.1.3 PES spectra of i-$Al_{70}Pd_{20}Mn_{10}$ near the Cooper minimum

The features in the valence bands due to the $4d$ and/or $5d$ states in alloys containing the $4d$ and/or $5d$ elements can be identified by taking advantage of the so-called Cooper minimum effect[134] which is the occurrence of a clear minimum in the σ for particular

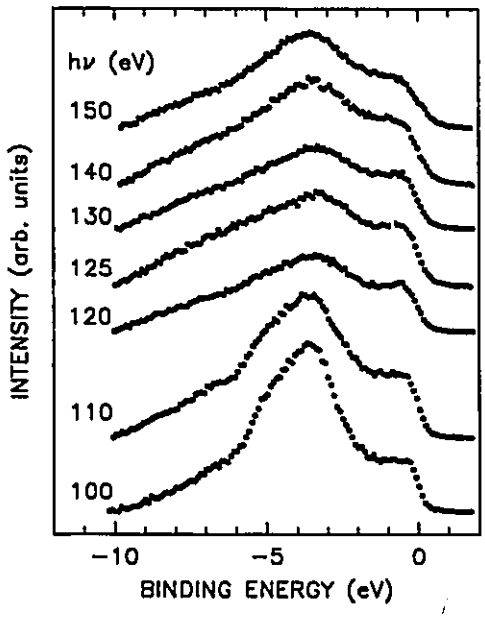

Figure 4.6: **Valence-band spectra of i-$Al_{70}Pd_{20}Mn_{10}$ for different $h\nu$ values in the vicinity of the Pd $4d$ Cooper minimum.**

orbitals. This effect results from the presence of a node or nodes in the radial part of the

$4d$ and $5d$ (but not $3d$) atomic wave functions.[10] The Cooper minimum in the $\sigma_{Pd(4d)}$ was calculated to be at $h\nu$=115 eV for pure Pd[114] [curve (b) in Fig. 4.5], but occurs in Pd alloys at $h\nu\approx$130 eV.[134, 135] While the curve (a) in Fig. 4.5 decreases slowly, the curve (b) drops down dramatically and reaches a minimum, i.e., the Cooper minimum, at $h\nu$=115 eV. One can thus expect a strong suppression of the contribution of the Pd $4d$ character to the valence band of i-$Al_{70}Pd_{20}Mn_{10}$ for the values of $h\nu$ close to 130 eV.

Fig. 4.6 shows that as $h\nu$ increases from below the Cooper minimum, the relative contribution of the E_B=−3.6 eV feature with respect to the E_B=−1.0 eV feature first decreases, reaches a minimum at $h\nu\approx$130 eV, and then starts to increase. Note that the Cooper minimum effect is much more dramatic (Fig. 4.6) than the Mn $3p\rightarrow3d$ photoemission resonance effect (Fig. 4.2). It is thus concluded that the E_B=−3.6 eV

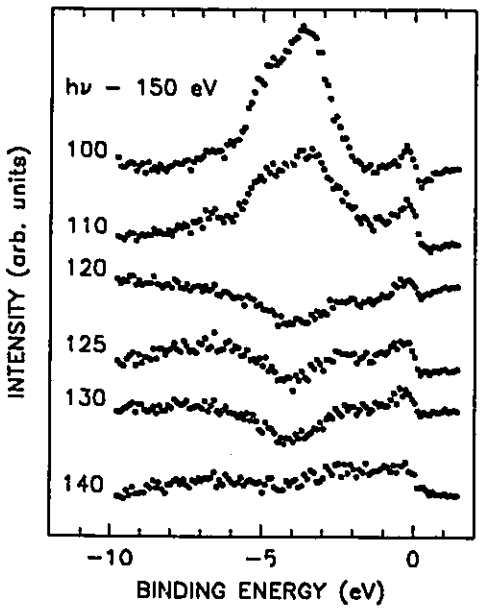

Figure 4.7: **Difference spectra obtained from the PES spectra in Fig. 4.6 by subtracting from them the spectrum measured at $h\nu$=150 eV. The number on the left side of each difference spectrum indicates the $h\nu$ value of the spectrum from which the $h\nu$=150 eV spectrum was subtracted.**

feature is predominantly due to the Pd $4d$-derived states.

The Cooper minimum effect can be demonstrated further by presenting the PES spectra of Fig. 4.6 as difference spectra (Fig. 4.7). There is a dramatic change of the difference intensities of the broad feature around −3.6 eV, which must be caused by the Cooper minimum effect (Fig. 4.7). The Mn 3*d* feature around −1.0 eV is better separated from the suppressed Pd 4*d* feature. The 3*d* character in the difference spectra (Fig. 4.7) spreads throughout the valence-band range. It decreases slowly as $h\nu$ increases because of the slow decrease in the $\sigma_{Mn(3d)}$ with the increase of $h\nu$ [curve (*a*) in Fig. 4.5]. Therefore, it can be concluded that the position of the peak maximum of the Mn 3*d*-derived states is at E_B=−1.0 eV with an uncertainty of 0.3 eV and that these states extend deep below E_F due to the hybridization with the Al *sp* and/or Pd 4*d* states.

4.1.4 Partial density of states

In order to determine the experimental Mn 3*d* and Pd 4*d* PDOS's, the PES spectra measured for $h\nu$ values close to the Pd 4*d* Cooper minimum[10] were used since these spectra exhibit the strongest variation in intensity (Fig. 4.2) caused by the large change in the $\sigma_{Pd(4d)}$.[86, 114] By taking the difference between the $h\nu$=100 and 120 eV valence bands, which have been scaled either to the height of the Pd 4*d* or to the height of the Mn 3*d* peak, one obtains the PDOS's of the Mn 3*d* and Pd 4*d* character, respectively.[86] Since the difference spectra have some scatter, they were smoothed to allow a better comparison with the theory (Fig. 4.8). It should be stressed that, apart from the expected minor differences, the same shapes for the experimental Mn 3*d* and Pd 4*d* PDOS's are obtained from the valence bands measured for other $h\nu$ values close to the Cooper minimum. However, the above subtraction method may lead to some artifacts for $|E_B| \geq 5$ eV. This is mainly due to the uncertainties associated with the correction of the raw PES data for the secondary-electron background which sharply increases in this region.[10]

A comparison between these PDOS's and those measured with the SXE technique

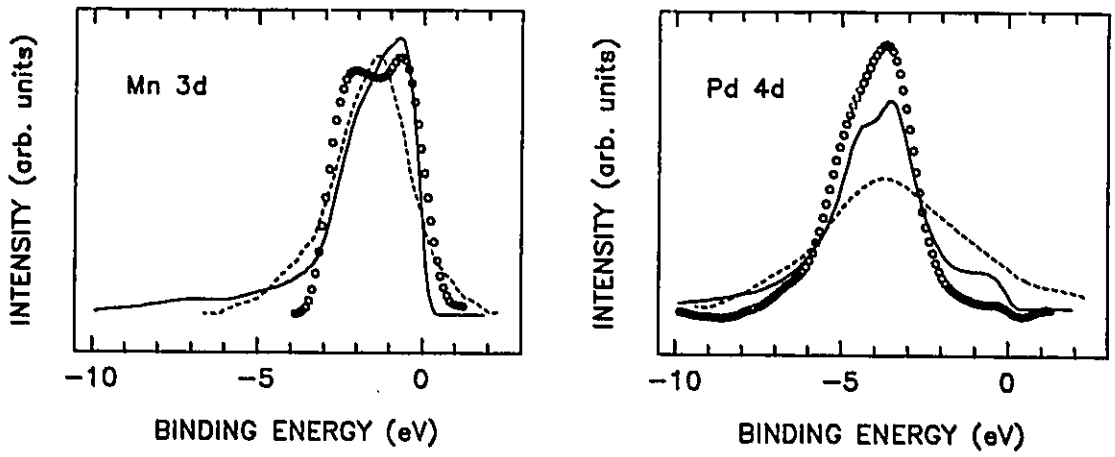

Figure 4.8: **Comparison of the PDOS's for the Mn 3*d* (left panel) and Pd 4*d* (right panel) in the *i*-Al-Pd-Mn alloys obtained from the PES spectra (open circles)[86] and from the SXE measurements (dashed line)[72, 73] with the corresponding broadened theoretical results (solid line)[54], as described in the text. All spectra for a given element were normalized to give an area equal to the number of the *d* electrons (5 for Mn 3*d* and 10 for Pd 4*d*).[86]**

is also shown in Fig. 4.8. The former exhibit more structure than the later. This is perhaps not surprising in view of the lifetime broadening effects. These effects are much more severe in the SXE technique than in the PES method.[136]

In a recent study[54] the electronic structure of several rational approximants of the *i*-Al-Pd-Mn phase was calculated. In order to make a meaningful comparison between the theoretical and experimental PDOS's, the former were appropriately broadened using the procedure described in §3.4. The Lorentzian FWHM was taken in the form of $\Gamma_L^0(|E_B| - E_F)^2$ (Ref. [112]) with Γ_L^0=0.02 eV^{-1} and the Gaussian FWHM was set to 0.4 eV. A reasonable agreement is obtained between such broadened theoretical PDOS's and the corresponding experimental ones derived from the PES spectra (Fig. 4.8). In particular, the humps at the left sides of the main theoretical Mn 3*d* and Pd 4*d* peaks are also observed in the experimental PDOS's.

In order to compare the theoretical total DOS calculated for the 8/5 approximant

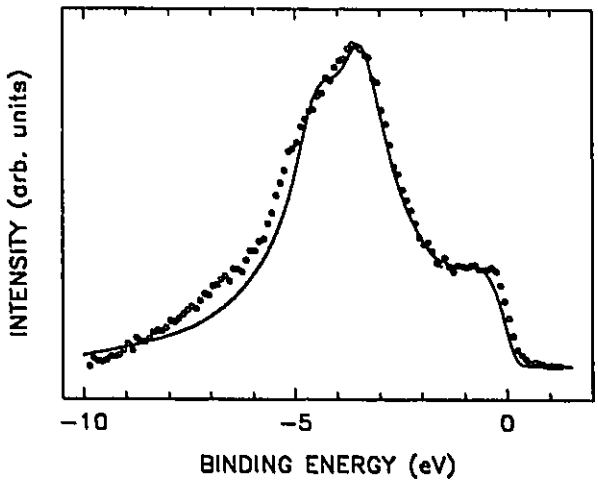

Figure 4.9: **Comparison of the valence band of the i-$Al_{70}Pd_{20}Mn_{10}$ alloy measured at $h\nu$=100 eV (open circles)[10] with the broadened theoretical DOS for the 8/5 approximant of the i-Al-Pd-Mn alloy (solid line),[84] as described in the text.**

of the i-Al-Pd-Mn alloy[84] with the valence band of i-$Al_{70}Pd_{20}Mn_{10}$ measured[10] at a given $h\nu$, the theoretical Al, Pd, and Mn PDOS's have to be first multiplied[5, 82] by the corresponding σ values at that $h\nu$. Since these σ values in the studied alloy are expected to differ from their atomic values, the ratio of the σ values corresponding to the Mn $3d$ and Pd $4d$ orbitals had to be varied to get the best agreement between theory and experiment.[86] The sum of the products of the theoretical PDOS's and the corresponding σ values was broadened in the same way as described before. A good agreement was obtained (Fig. 4.9) between the valence band measured at $h\nu$=100 eV and the broadened theoretical DOS. It is thus concluded that the main features of the theoretical Mn $3d$ and Pd $4d$ PDOS's and of the total DOS calculated for the 8/5 approximant of the i-$Al_{70}Pd_{20}Mn_{10}$ alloy are observed in the corresponding experimental PES spectra.

4.1.5 Spikiness and pseudogap at E_F

The theoretical calculations mentioned above[54] predict the existence of a structure-induced pseudogap in the DOS around E_F for the higher-order approximants of the i-alloy $Al_{70}Pd_{20}Mn_{10}$. Furthermore, the DOS is predicted to have a fine structure in the form of many spiked peaks (Fig. 4.10). Neither the minimum of the DOS(E_F) nor the DOS spikiness have been observed in the PES spectra within the resolution of the experiment.[86] There can be several reasons for this. First, as discussed in §3.6, a much better resolution than the one used (0.4 eV) is needed to investigate the possible existence of the predicted DOS(E_F) minimum and the DOS spikiness. Second, there is

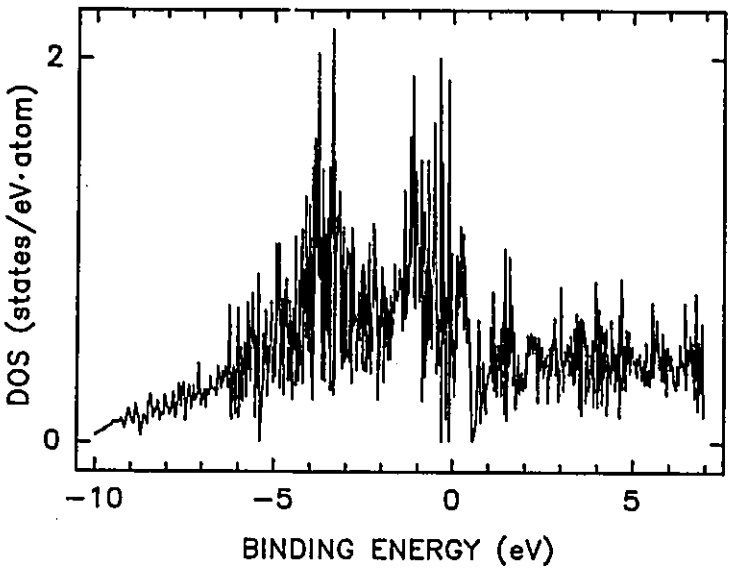

Figure 4.10: **Theoretical DOS for the 1/1 approximant of the i-Al-Pd-Mn alloy (model M2 in Ref. [54]).**

some degree of chemical and topological disorder even in the QC's which are regarded as perfect from the structure point of view.[5, 82] Chemical disorder is associated with the fact that all known stable QC's are ternary alloys.[5, 82] Topological disorder results from the very nature of quasiperiodicity which implies that no two crystallographic

sites of a given atom are exactly the same. These two types of disorder, which are clearly observed with the experimental local probes,[5, 82] may significantly influence the electronic properties of QC's. In particular, they may smear out the DOS spikiness and the DOS(E_F) minimum. A further discussion of disorder is presented in §4.4.5. And finally, the theoretical calculations may have to be improved, for example, by including more atoms in the calculations.

4.1.6 Al 2p core level shift

The Al 2p core level lines in Al metal and in i-$Al_{70}Pd_{20}Mn_{10}$ are compared in Fig. 4.11. It can be noticed that the Al $2p_{1/2}$ and $2p_{3/2}$ are separated in the Al metal (inset of

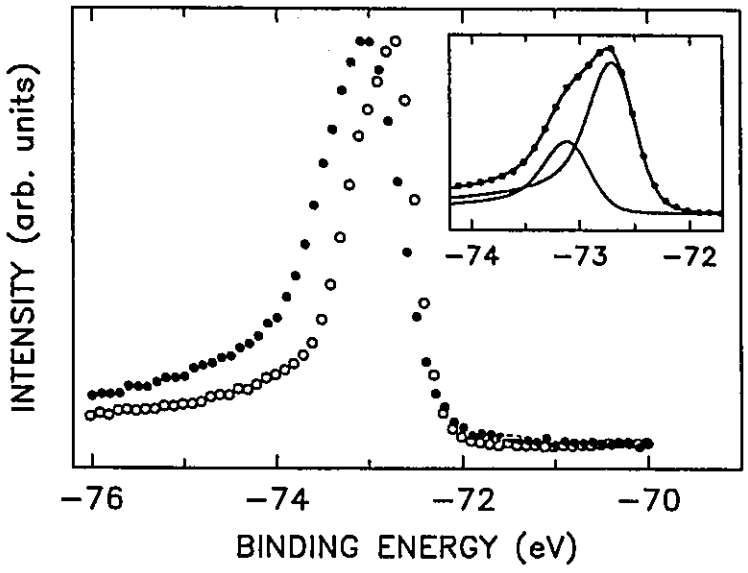

Figure 4.11: **Al 2p PES spectra of the Al metal (○) and i-$Al_{70}Pd_{20}Mn_{10}$ alloy (●). The spectra were normalized to give a constant height between the maximum and minimum recorded count. The inset shows the fit of the Al 2p spectrum of the Al metal with two Doniach-Šunjić profiles[122] [Eq. (3.7)] corresponding to Al $2p_{1/2}$ and $2p_{3/2}$ core levels.**

Fig. 4.11), but they overlap in the i-$Al_{70}Pd_{20}Mn_{10}$ alloy. The separation of the Al

$2p_{1/2}$ and $2p_{3/2}$ components in the Al metal found from the fit with two Doniach-Šunjić profiles[122] [Eq. (3.7)] is 0.41(1) eV, which is in a good agreement with the value of 0.42 eV reported in the literature.[124] The observation of the Al $2p_{1/2}$ and $2p_{3/2}$ lines in the Al metal confirms that the overall energy resolution of the recorded PES spectra is 0.4 eV. The main result obtained from Fig. 4.11 is the observation of the E_B shift in i-$Al_{70}Pd_{20}Mn_{10}$ by 0.21 eV towards higher $|E_B|$ values with respect to Al metal. The interpretation of the E_B shift is complicated by the fact that it consists of contributions due to chemical, configuration, and relaxation shift.[126] These contributions are difficult to evaluate theoretically even for simple binary alloys.

4.2 *i*-Alloy $Al_{65}Cu_{20}Os_{15}$

Os, Ru, and Fe metals have 5*d*, 4*d*, and 3*d* electrons, respectively. These electrons contribute to a common feature in the valence bands of the *i*-alloys $Al_{65}Cu_{20}Md_{15}$ which is located close to the E_F. The PES spectra of these *i*-phases[5, 74, 82, 84] have common characteristics which were discussed before. In this section *i*-$Al_{65}Cu_{20}Os_{15}$ is taken as an example to present the PES data for the *i*-alloys $Al_{65}Cu_{20}Md_{15}$.

4.2.1 Resonance photoemission

To determine the main features in a valence band due to the Os 5*d* states, the resonant photoemission can be employed (§3.3).[107, 137] For an Os metal one would expect the stronger $5p \rightarrow 5d$ transition to occur at about 44.5 eV ($5p_{3/2} \rightarrow 5d$) and the weaker $4f \rightarrow 5d$ transition to take place at about 50.7 eV ($4f_{7/2} \rightarrow 5d$).[108] The Os 5*d*-derived features should be enhanced or suppressed[137] as the $h\nu$ is swept through the 5*p*-5*d* and 4*f*-5*d* thresholds. It can be seen in Fig. 4.12 that, as the $h\nu$ increases, the relative intensity of the peak at about E_B=−1.5 eV with respect to the peak at about E_B=−3.7 eV decreases first and reaches a minimum at $h\nu$=44.5 eV. Then it increases slightly between $h\nu$=50 and 60 eV. This corresponds to the stronger $5p \rightarrow 5d$ resonance (the $4f \rightarrow 5d$ resonance is too weak to be observed in the measured valence bands) and thus indicates that the peak at about E_B=−1.5 eV is predominantly due to the Os 5*d*-derived states.

It should be noted that the $5p \rightarrow 5d$ and $4f \rightarrow 5d$ resonances occur in the region where there is a strong decrease of $\sigma_{Os(5d)}$ (Fig. 4.13), and consequently the decrease of the relative intensity of the peak at E_B=−1.5 eV is due not only to the stronger $5p \rightarrow 5d$ resonance, but also due to the decrease of $\sigma_{Os(5d)}$. Nevertheless the decrease of the relative intensity of the E_B=−1.5 eV peak when going from $h\nu$=40 to 44.5 eV (Fig. 4.12) is stronger than expected only from the σ changes (Fig. 4.13), and supports the conclusion

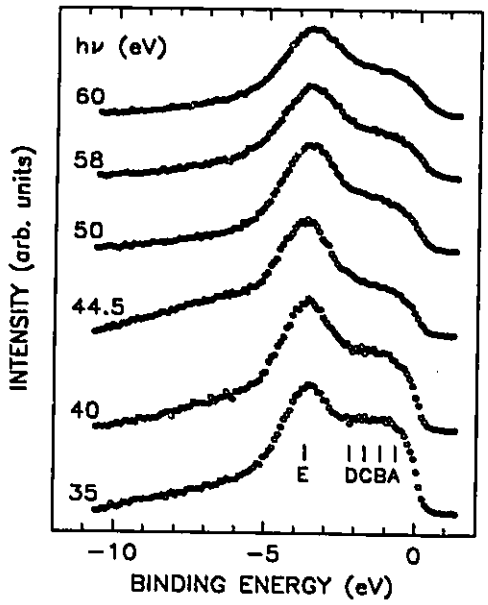

Figure 4.12: **Valence-band spectra of i-$Al_{65}Cu_{20}Os_{15}$ for different $h\nu$ values around the $5p\rightarrow 5d$ and $4f\rightarrow 5d$ transitions. A, B, C, D, and E identify the E_B values for which CIS spectra were measured (Fig. 4.14).**

that the intensity change is mainly due to the Os $5p\rightarrow 5d$ resonance, and thus the feature at E_B=−1.5 eV is predominantly due to Os $5d$-derived states.

It is worth indicating here that the σ values presented in Fig. 4.13 are the *atomic* values[114] and are expected to be different in elemental metals and their alloys. In fact, it is well established experimentally that,[134] due to the solid-state effects, σ values in metallic systems differ significantly from the atomic values.[114] Nevertheless, the trends in the $\sigma(h\nu)$ are similar in metallic systems[134] to those in the corresponding atomic systems.[114] Therefore, in view of the lack of calculations of the σ values in the metallic alloys, the calculated atomic σ values are very useful in interpreting the PES data.

As discussed in §3.3, CIS spectra show more clearly the resonant photoemission intensity variation. The CIS spectra of i-$Al_{65}Cu_{20}Os_{15}$ for the E_B values corresponding to the positions denoted by A, B, C, D, and E in Fig. 4.12 are shown in Fig. 4.14. One

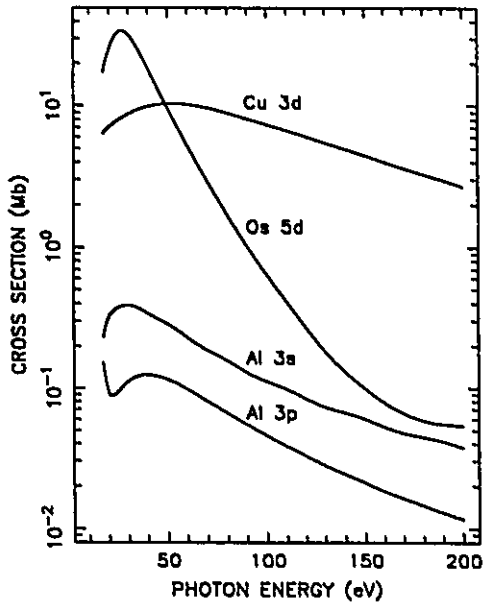

Figure 4.13: **Atomic subshell σ as a function of $h\nu$ for Cu $3d$, Os $5d$, Al $3s$, and Al $3p$ orbitals.[114] Note the logarithmic scale on the ordinate axis.**

can see an intensity minimum for $h\nu$ values around 44 eV, and another weak one around 51 eV. These spectra were fitted to two Fano profiles [Eq. (3.6)] in order to account for the two $5p \rightarrow 5d$ and $4f \rightarrow 5d$ transitions mentioned above. A linear background I_{nr} was assumed in the fit. The parameters from the fit are given in Table 4.3. As expected, the nonresonant emission parameters corresponding to the two transitions fulfill the inequality $I_0^{3/2} > I_0^{7/2}$ (Table 4.3). The resonance energies $E_R^{3/2}$ and $E_R^{7/2}$ (Table 4.3) are close to the corresponding core-level values for an Os metal. The broad character of the resonance is reflected in the large values of $\Gamma^{3/2}$ and $\Gamma^{7/2}$ (Table 4.3). The strongest resonance occurs for $E_B = -1.7$ eV and the weaker resonances can be also observed both below and above the $E_B = -1.7$ eV value. The fact that the resonances take place in a rather broad valence-band region can be interpreted as evidence of hybridization between the Os $5d$ and the Al sp and/or Cu $3d$ states.

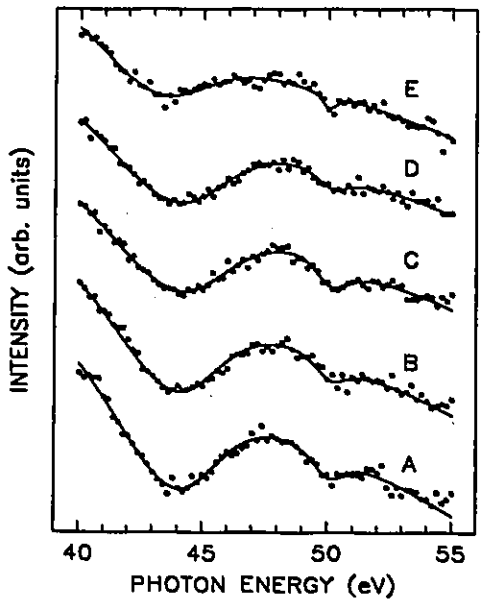

Figure 4.14: **CIS spectra measured for the valence-band positions A, B, C, D, and E in Fig. 4.12, which are identified here by the same letters. The solid line is a fit to two Fano profiles [Eq. (3.6)] and a linear background, as described in the text. The parameters are given in Table 4.3.**

Table 4.3: **Parameters obtained by fitting the CIS spectra in Fig. 4.14 for the E_B values corresponding to the positions A, B, C, D, and E indicated in Fig. 4.12, to two Fano profiles [Eq. (3.6)] associated with the Os $5p_{3/2}\rightarrow 5d$ and $4f_{7/2}\rightarrow 5d$ transitions. The parameters with the superscripts 3/2 and 7/2 refer respectively to the Os $5p_{3/2}\rightarrow 5d$ and $4f_{7/2}\rightarrow 5d$ transitions.**

Label	E_B (eV)	$I_0^{3/2}$	$I_0^{7/2}$	$E_R^{3/2}$ (eV)	$E_R^{7/2}$ (eV)	$q^{3/2}$	$q^{7/2}$	$\Gamma^{3/2}$ (eV)	$\Gamma^{7/2}$ (eV)
A	−0.67	155(11)	36(5)	44.3(2)	50.1(2)	0.24(6)	0.01(17)	6.0(5)	1.8(4)
B	−1.17	188(18)	40(8)	44.3(2)	50.0(3)	0.24(6)	−0.12(20)	6.1(7)	1.8(6)
C	−1.67	193(19)	52(8)	44.6(3)	50.0(2)	0.29(8)	−0.20(15)	7.2(8)	1.8(4)
D	−2.17	187(19)	37(6)	44.4(2)	50.0(6)	0.27(6)	−0.16 (8)	7.1(8)	1.9(5)
E	−3.67	136(19)	30(7)	43.4(9)	50.0(2)	0.14(7)	0.01(20)	6.2(9)	0.7(3)

4.2.2 PES spectra of i-$Al_{65}Cu_{20}Os_{15}$ near the Cooper minimum

The features in a valence-band spectrum originating from the $4d$ or $5d$ states can be identified by making use of the Cooper minimum effect.[134] The Cooper minimum in the $\sigma_{Os(5d)}$ is at about $h\nu$=200 eV (Fig. 4.13).[114] However, its position and depth are expected to be changed in alloys due to the solid-state effects.[134] Usually, the shift is about 30 eV towards higher $h\nu$ values and the minimum is shallower[134] than predicted by atomic calculations.[114] Since the decrease in the $\sigma_{Os(5d)}$ in the 50-200 eV $h\nu$ range is expected to be about two orders of magnitude (Fig. 4.13), one can anticipate a strong suppression of the contribution of the Os $5d$ character to the valence band of i-$Al_{65}Cu_{20}Os_{15}$ for $h\nu$ values close to the Cooper minimum.

Figure 4.15 shows that the relative contribution of the feature at $E_B \approx -1.5$ eV (from

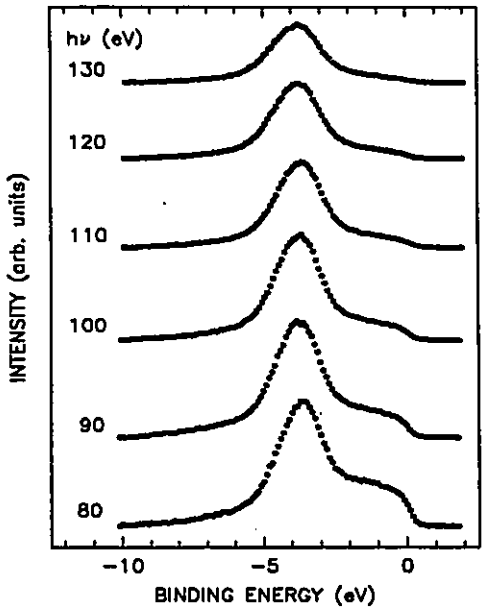

Figure 4.15: **Valence-band spectra of i-$Al_{65}Cu_{20}Os_{15}$ for different $h\nu$ values around the Cooper minimum of $\sigma_{Os(5d)}$.**

Os 5*d*-derived states) with respect to the feature at $E_B \approx -3.7$ eV decreases steadily as $h\nu$ increases from 80 eV. At $h\nu$=130 eV, it is almost completely suppressed. In other words, since $\sigma_{Cu(3d)}$ decreases much slower with the increase of $h\nu$ than does the $\sigma_{Os(5d)}$, and since $\sigma_{Cu(3d)}$ for $h\nu$=130 eV is expected to be almost two orders of magnitude larger than $\sigma_{Os(5d)}$ (Fig. 4.13), the $h\nu$=130 eV valence band (Fig. 4.15) must be almost entirely due to the Cu 3*d* emission. It is worth noting that the Cooper minimum effect is much more dramatic (Fig. 4.14) than the Os 5*p*→5*d* photoemission resonance effect (Fig. 4.12).

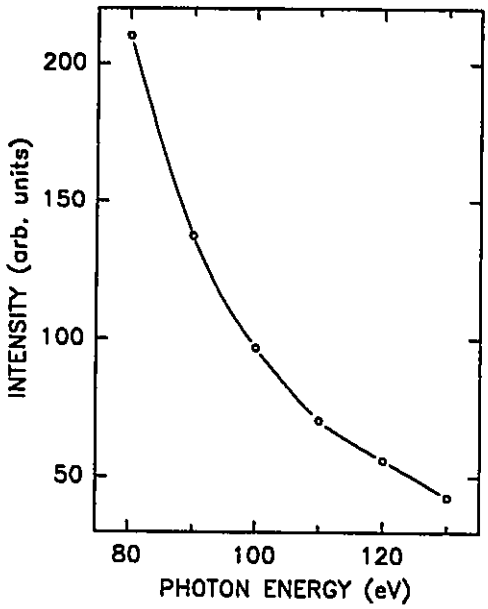

Figure 4.16: **Photoemission intensity at E_B=−1.5 eV as a function of $h\nu$ obtained from the spectra in Fig. 4.15, as described in the text. The solid line is a guide for the eye.**

To show the effect of the Cooper minimum in a more quantitative way, a plot of the photoemission intensity at E_B=−1.5 eV as a function of $h\nu$ is presented in Fig. 4.16. This intensity was obtained as an average of 11 intensity values around E_B=−1.5 eV. One can see clearly a strong decrease of the photoemission intensity with increasing $h\nu$. However, this decrease is not one order of magnitude, as expected from Fig. 4.13, but by about

the factor of five. As mentioned above, this is caused by the solid-state effects.[10, 134] However, the trend in the $\upsilon_{Os(5d)}$ dependence on $h\nu$ in the studied alloy (Fig. 4.16) is similar to that based on the atomic calculations (Fig. 4.13). The contribution due to the Cu 3*d*-like states is well separated at $h\nu$=130 eV from that originating from the Os 5*d*-like states (Fig. 4.15) and has its peak at E_B=−3.7 eV. The weak and broad spectral weight around E_B=−6 eV (Figs. 4.12 and 4.15) can be ascribed to the Al *sp*-derived states, based on the results of SXE studies of Al-based *i*-alloys.[49]

Under the assumption that the dipole matrix elements [Eq. (3.2)] are constant over the width of the valence band, the measured PES valence bands, when properly corrected for the experimental factors and for inelastically scattered electrons, are generally proportional to the DOS modulated by the σ values. In the particular case of the *i*-$Al_{65}Cu_{20}Os_{15}$, the valence bands measured for $h\nu$ values which are outside the $5p \rightarrow 5d$ resonance and for which $\sigma_{Cu(3d)} \approx \sigma_{Os(5d)}$, are expected to well represent the total DOS of the *d* character. Since $\sigma_{Cu(3d)} \approx \sigma_{Os(5d)}$ occurs at around $h\nu$=50 eV (Fig. 4.12), the vicinity of that $h\nu$ value should represent well the total d-derived DOS in the studied alloy. Additional arguments in support of this statement will be given below.

4.2.3 Partial density of states

The analysis presented above made it possible to unambiguously ascribe the two main features in the valence bands of *i*-$Al_{65}Cu_{20}Os_{15}$ to the Os 5*d*- and Cu 3*d*-derived states. To determine the experimental electronic structure associated with the occupied states of an alloy, it is also necessary to establish partial spectral weights due to *s*, *p*, *d*, and *f* electrons of a given element in the alloy. These partial weights are generally proportional to the PDOS associated with a given state of that element, as was discussed above. Before the advent of synchrotron radiation as a tunable excitation source, such PDOS was determined almost exclusively using the SXE technique.[5] The use of synchrotron-

radiation-based PES technique allows one also to determine the PDOS for some orbitals, as is demonstrated below.

The PES valence-band spectra represent mainly the DOS of d and f character because of their large σ values relative to the values associated with the s and p orbitals (Fig. 4.13).[114] Thus, to a first approximation, the contribution to the valence band of i-$Al_{65}Cu_{20}Os_{15}$ from sp states can be neglected. The valence-band intensity $I(h\nu, E_B)$ of i-$Al_{65}Cu_{20}Os_{15}$ can be represented by[5, 135]

$$I(h\nu, E_B) = C(h\nu)[\sigma_{Cu}(h\nu)D_{Cu}(E_B)/Z_{Cu} + \sigma_{Os}(h\nu)D_{Os}(E_B)/Z_{Os}], \quad (4.3)$$

where D_{Cu} and D_{Os} are the Cu $3d$ and Os $5d$ PDOS's, respectively. The PDOS is assumed[5] to fulfill the normalization condition

$$\Sigma D_i(E_B)\Delta(E_B) = N_i Z_i, \quad (4.4)$$

where N_i and Z_i are respectively the concentration and the number of d electrons of the i-th element. Here it is assumed that one has N_{Cu}=20, N_{Os}=15, Z_{Cu}=10, and Z_{Os}=6. The instrumental factor is represented by $C(h\nu)$. In principle, this factor should be independent of $h\nu$ if the corrections to the as-measured valence bands, which are described in §3.2, could be done ideally and if one could know precisely the values of $\sigma_{Cu(3d)}$ and $\sigma_{Os(5d)}$ in the studied alloy. Since in practice this cannot be achieved, the factor $C(h\nu)$ has a weak dependence on $h\nu$.

In order to assess the reliability and the reproducibility of the Os $5d$ and Cu $3d$ PDOS's in i-$Al_{65}Cu_{20}Os_{15}$ which were obtained from the PES spectra, two approaches were used. In the first approach, a difference spectrum was obtained by direct subtraction of the $h\nu$=90 eV spectrum from the $h\nu$=80 eV spectrum in Fig. 4.15 (triangles in Fig. 4.17). It presents the Os $5d$ PDOS because the small change of $\sigma_{Cu(3d)}$ in the $h\nu$ range 80-90 eV (Fig. 4.13) assures that the Cu $3d$ contribution effectively cancels out in the difference spectrum. Note that the direct subtraction is equivalent to the assumption

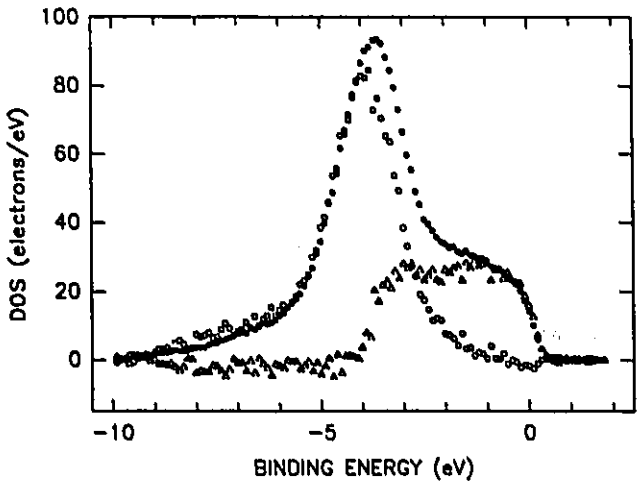

Figure 4.17: **Difference between the $h\nu$=80 and 90 eV spectra from Fig. 4.15 obtained by a direct subtraction (△), and by a subtraction following the scaling to the Os 5*d* features of the two spectra (○), as described in the text. They represent respectively the Os 5*d* and Cu 3*d* PDOS's. The sum (•) of the difference spectra represents the total DOS of the *d* character in *i*-$Al_{65}Cu_{20}Os_{15}$.**[5]

that $C(h\nu)$ and $\sigma_{Cu}(h\nu)$ are independent of $h\nu$ which, as indicated above, is justified to a first approximation. Next, the difference between the same valence-band spectra was calculated as $I(90\text{ eV}) - h_{Os} I(80\text{ eV})$ by scaling the $h\nu$=80 eV spectrum with the factor h_{Os}=0.61 to match the height of its Os 5*d* feature to that of the $h\nu$=90 eV spectrum (open circles in Fig. 4.17); this is a graphical attempt to account for the differences between the $\sigma_{Os}(h\nu)$ values at $h\nu$=80 and 90 eV. This procedure assures that the Os 5*d* contribution cancels out in the difference spectrum which thus represents the Cu 3*d* PDOS. The total *d*-derived DOS is shown by the filled circles in Fig. 4.17. All the three DOS plots in Fig. 4.17 fulfill the normalization condition in Eq. (4.4). Applying this method to other valence bands in the vicinity of the Os 5*d* Cooper minimum leads to essentially the same Os 5*d* and Cu 3*d* PDOS's as those shown in Fig. 4.17.

The second approach of obtaining the Cu 3*d* and Os 5*d* PDOS's from the measured valence bands is based on Eq. (4.3) for two different $h\nu$ values. The factors $C(h\nu)$

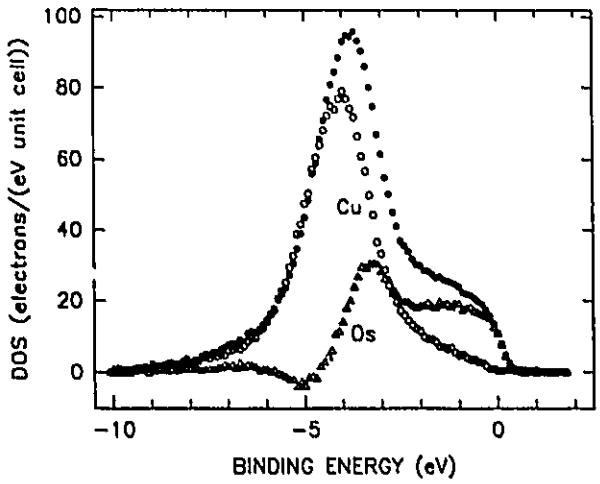

Figure 4.18: **PDOS's of the Os 5*d*-derived states (△) and Cu 3*d*-derived states (○) obtained from the $h\nu$=80 and 130 eV spectra in Fig. 4.15 and by using Eq. (4.3), as described in the text. Their sum (•) represents the total DOS of the *d* character in *i*-$Al_{65}Cu_{20}Os_{15}$.**

corresponding to theses values are then determined from the total integrated intensity of the experimental valence bands, the normalization condition of Eq. (4.4), and the values of $\sigma_{Cu}(h\nu)$ and $\sigma_{Os}(h\nu)$. Because of the expected shift of the Cooper minimum by about 30 eV towards higher $h\nu$ values in the studied alloy, which was mentioned earlier, the modified $\sigma_{Os}(h\nu)$ values corresponding to the atomic values $\sigma_{Os}(h\nu - 30)$ were used.[5, 114] The Cu 3*d* and Os 5*d* PDOS's obtained in this way by using the $h\nu$=80 and 130 eV valence bands in Fig. 4.15, as well as their sum, are shown in Fig. 4.18. It should be stressed that essentially the same results as those in Fig. 4.18 are obtained for other pairs of the measured valence bands. As can be seen by comparing Figs. 4.17 and 4.18, the Cu 3*d* and Os 5*d* PDOS's obtained by the two methods are very similar. This gives us confidence in their reliability.

By using Eq. (4.3), one should be able to reproduce the experimental valence bands measured for all $h\nu$ values provided that the Cu 3*d* and Os 5*d* PDOS's in Fig. 4.18 are a good measure of the true Cu 3*d* and Os 5*d* DOS's in *i*-$Al_{65}Cu_{20}Os_{15}$ and provided that

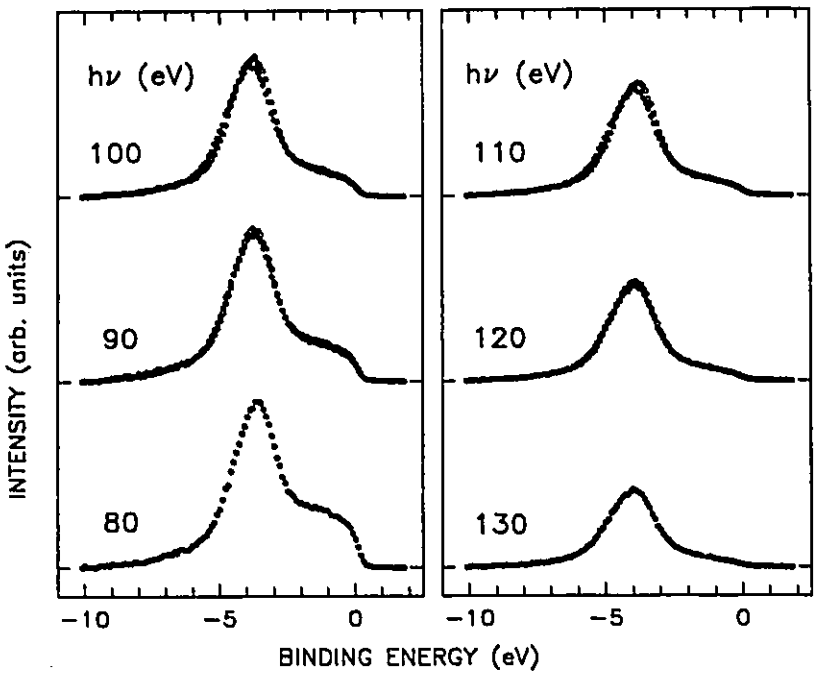

Figure 4.19: **Comparison of the valence bands generated from Eq. (4.3) by using the empirical Cu 3*d* and Os 5*d* PDOS's from Fig. 4.18 (•) with the experimental valence bands from Fig. 4.15 (○).**

the $\sigma_{Cu}(h\nu)$ and $\sigma_{Os}(h\nu)$ values used are accurate enough. The reproduced valence bands calculated for all $h\nu$ values are compared with the corresponding experimental valence bands in Fig. 4.19. Obviously, a perfect agreement (Fig. 4.19) between the experimental and the generated valence bands occurs at $h\nu$=80 and 130 eV. This is because these two experimental valence bands were used to determine the Cu 3*d* and Os 5*d* PDOS's in Fig. 4.18. Keeping in mind the simplicity of the model expressed by Eq. (4.3), there is a good agreement between the predictions of the model and the experimental data (Fig. 4.19).

4.3 UPS data of i-$Al_{65}Cu_{20}Fe_{7.5}Ru_{7.5}$

Based on the arguments presented before, high energy-resolution (<0.1 eV) spectroscopic experiments are indispensable for the direct and unambiguous detection of the theoretically-predicted pseudogap around E_F and the spikiness of the DOS in QC's.[5, 10, 82] This section presents the recent high energy-resolution UPS results on the i-alloy $Al_{65}Cu_{20}Fe_{7.5}Ru_{7.5}$.[84]

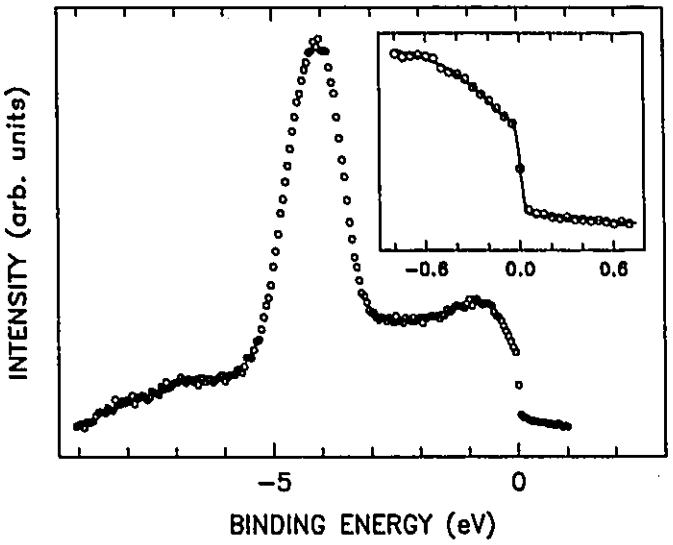

Figure 4.20: **High resolution valence band of i-$Al_{65}Cu_{20}Fe_{7.5}Ru_{7.5}$ measured at $h\nu$=40.8 eV and at 14.5 K. The raw data[84] were corrected for the secondary-electron background. The inset shows the fit to a Lorentzian-type pseudogap in the vicinity of E_F, as described in the text.**

Fig. 4.20 shows the UPS valence-band spectrum of the i-$Al_{65}Cu_{20}Fe_{7.5}Ru_{7.5}$ alloy measured at $h\nu$=40.8 eV and at temperature 14.5 K. Two broad features can be observed. Based on the results of the studies on the i-alloys $Al_{65}Cu_{20}Fe_{15}$[74] and $Al_{65}Cu_{20}Ru_{15}$,[82] the first one at $E_B \approx = -0.8$ eV must be due to the Fe $3d$- and Ru $4d$-derived states, whereas the second one must be due to the Cu $3d$-derived states. Three observations are apparent from Fig. 4.20. First, there is a strong intensity decrease towards E_F which

starts at E_B=−0.8 eV. This decrease can be interpreted as being due to the presence of a pseudogap in the vicinity of E_F. A more quantitative interpretation is given below. Second, an abrupt intensity decrease occurs at around E_B=0 eV, which is obviously due to the Fermi edge cut-off. The presence of a clear Fermi edge constitutes a convincing proof that the system is metallic. The fit of the leading Fermi edge gives a Gaussian FWHM of 55(1) meV as the instrumental resolution. Third, there is no evidence for the existence of the spikes which should clearly be seen for the energy resolution used in the experiment, as discussed in §3.6.

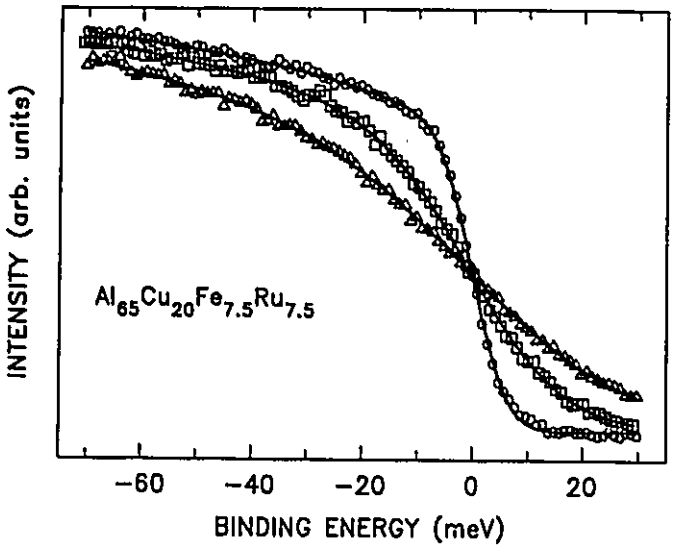

Figure 4.21: **UPS valence bands of i-$Al_{65}Cu_{20}Fe_{7.5}Ru_{7.5}$ measured at $h\nu$=21.2 eV and at temperatures 14.5 K (○), 80 K (□) and 160 K (△). The solid lines are the fits to a linearly decreasing intensity multiplied by the Fermi-Dirac function at the corresponding temperature and convoluted with a Gaussian.**

One can reproduce the observed structure of the valence band close to E_F (inset of Fig. 4.20) by using a simple model.[67] This model assumes that the normal DOS, i.e., the DOS at 0 K, would be a linear function around E_F if there is no gap. This normal DOS is then multiplied by a Lorentzian dip centered at E_F with the FWHM, Γ_L, and

the gap depth C with respect to the normal DOS to account for the pseudogap gap, and convoluted with a Gaussian to account for the instrumental resolution. One can obtain a relatively good fit (inset in Fig.4.20) for Γ_L=0.33 eV and C=45%. It should be pointed out that these fitted parameters are not unique. This is because the choice of the fitted range, and therefore of the linear function, is rather arbitrary, as is the Lorentzian gap form which may not be necessarily centered at the E_F. Nevertheless, the high energy-resolution spectrum shows that the valence band has a gap close to E_F. The significant intensity of the DOS(E_F) demonstrates that this system is metallic.

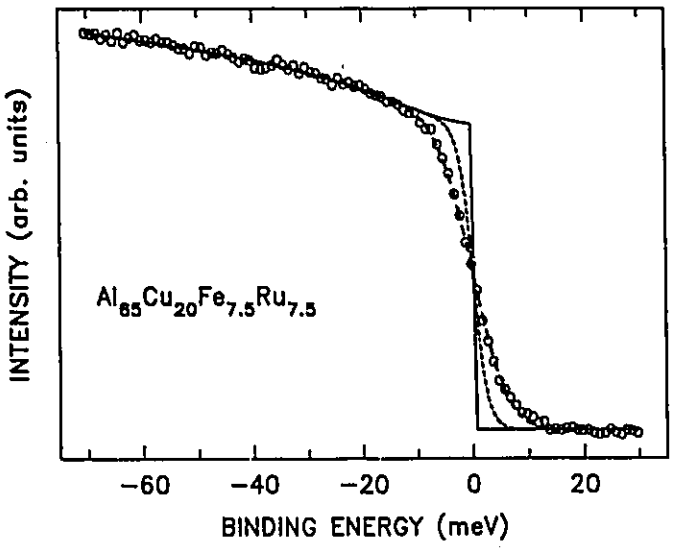

Figure 4.22: **UPS valence band of i-$Al_{65}Cu_{20}Fe_{7.5}Ru_{7.5}$ measured at $h\nu$=21.2 eV and at temperature 14.5 K with the fitted theoretical spectra. The solid line and the broken line are the "real" spectra at T=0 and 14.5 K respectively at an infinity resolution, as described in the text.**

The valence bands of i-$Al_{65}Cu_{20}Fe_{7.5}Ru_{7.5}$ measured at $h\nu$=21.2 eV and at different temperatures are presented in Fig. 4.21. The temperature evolution of the leading edge of these bands follows the temperature evolution of the Fermi-Dirac function. This additionally confirms the metallic character of the i-$Al_{65}Cu_{20}Fe_{7.5}Ru_{7.5}$ alloy.

The spectrum measured at 14.5 K is shown in Fig. 4.22 with two "theoretical" curves,

in addition to the spectrum fitted curve. The solid and the broken lines represent the "real" spectra which would have been obtained by carrying out the measurements at T=0 and 14.5 K, respectively, and with an infinitely high resolution. The fit of this spectrum gives 10 meV (Gaussian FWHM) for the instrumental resolution. Similar results were also obtained for i-$Al_{65}Cu_{20}Fe_{15}$ and other stable i- and d-alloys, except for the i-Al-Pd-Re system.[61] For the i-Al-Pd-Re system, no well-defined Fermi edge was observed and there is also a very low intensity at E_F (Fig. 6 of Ref. [61]). This shows that the i-Al-Pd-Re system is nonmetallic. The UPS spectra (Figs. 4.21 and 4.22 in this work and Figs. 3-6 in Ref. [61]) clearly show that no spikes can be observed, and that all the i-systems other than i-Al-Pd-Re are metallic.

In conclusion, the high resolution UPS measurements[61, 84] provide a direct experimental proof that there is a wide pseudogap in the vicinity of E_F. This gap must be partially responsible for the observed high values of ρ.[61] All known QC's, except for i-Al-Pd-Re, are metallic as evidenced by a clearly developed Fermi edge.[61] No spikes could be detected in all PES spectra measured so far.

4.4 Discussion

4.4.1 PES spectra of i-$Al_{70}Pd_{20}Mn_{10}$ and related c-alloys

The result for the peak positions of the Pd 4d-derived states at -3.6 eV and Mn 3d-derived states at -1.3 eV agrees well with the values of -3.5 eV and -1.0 eV, respectively, obtained in a recent SXE study[72, 73] of i-$Al_{71}Pd_{19}Mn_{10}$ (Fig. 4.8). However, the Mn 3d-states are spread wider (Fig. 4.8) than suggested by the SXE result.[73] SXE studies of i-$Al_{71}Pd_{19}Mn_{10}$[72, 73] and i-$Al_{70}Pd_{21}Mn_9$[138] show the existence of the peak in the intensity associated with the Al s states and the large intensity associated with the Al p states at $E_B \approx -6$ eV. Therefore the weak spectral weight below $E_B = -6$ eV

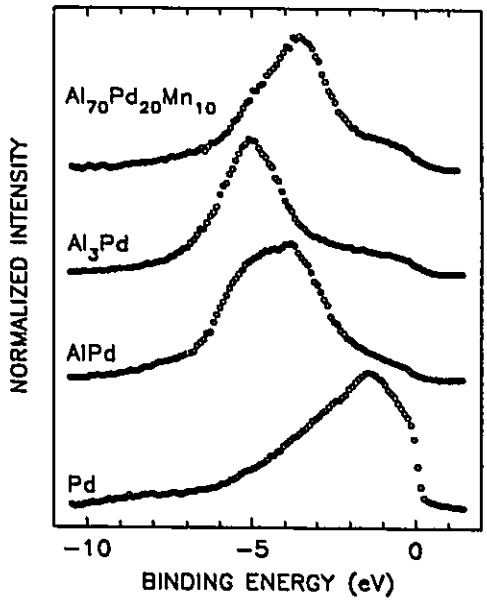

Figure 4.23: **Comparison of the PES valence band of i-$Al_{70}Pd_{20}Mn_{10}$ measured at $h\nu$=60 eV with that of a Pd metal measured also at $h\nu$=60 eV (the raw PES spectrum of Pd metal was kindly provided by Nahm and Oh; the secondary-electron contribution was subtracted from the original spectrum) and with the XPS valence bands of Al_3Pd and AlPd c-alloys from Fig. 12 of Ref. [139] (the secondary-electron contribution was subtracted from the original spectra). The spectra were normalized to give a constant height between the maximum and minimum recorded count.**

observed in the valence band of the studied sample (Figs. 4.2 and 4.6) can be ascribed to the Al sp-derived states.

It is well established from the XPS and UPS experiments that in pure Pd[140] and Mn[141] there is a high DOS(E_F). Depending on the $h\nu$ range used, the observed broad peak in the Pd valence band lies in the range from -1.3 to -2.3 eV (Fig. 4.23).[140] For pure Mn, two features at $E_B \approx -0.5$ to -1.0 and -3.0 eV are present in the valence band.[141] The presence of the Pd 4d-derived peak at $E_B = -3.6$ eV in the valence band of i-$Al_{70}Pd_{20}Mn_{10}$ as compared to the corresponding peak in a pure Pd metal (Fig. 4.23), clearly indicates the shift of the Pd 4d-derived states in the i-alloy away from E_F. This shift should lead to the decrease in the Pd contribution to the DOS(E_F). Such a shift is

also observed in the valence bands of c-Al_3Pd and c-AlPd alloys (Fig. 4.23) and it clearly leads to a decrease in the Pd $4d$ contribution to the DOS(E_F) (Fig. 4.23). A similar shift of the Mn $3d$-derived states cannot be seen in the recorded spectra (Figs. 4.2, 4.6 and 4.7).

The depression of intensity as the E_B approaches E_F observed in the PES[67, 74] and SXE[69, 70, 73, 138, 142] spectra of the QC's containing TM elements has been interpreted as evidence for the opening of a theoretically predicted[45, 57–59, 143, 144] pseudogap at E_F. It should be kept in mind, however, that there are at least two effects which lead to the intensity decrease as the E_B approaches E_F. The first one is a simple Fermi cut-off, which would be especially important for the QC's with TM elements whose d states significantly contribute to the measured intensity around E_F. In the case of the studied i-$Al_{70}Pd_{20}Mn_{10}$, the Mn $3d$-derived states must contribute to the measured intensity at E_F because of the closeness of the feature due to the Mn $3d$ states to the E_F. The second effect leading to the decrease of intensity as the E_B approaches E_F could be associated with the opening of a pseudogap at E_F. It can only be concluded from the medium resolution PES studies that the PES spectra are indicative of a possible opening of a pseudogap at E_F in i-$Al_{70}Pd_{20}Mn_{10}$. Its existence is proven by the high resolution UPS results.[84]

4.4.2 Valence bands of the studied i-alloys

When the valence band of the i-$Al_{65}Cu_{20}Os_{15}$ is compared with those of other thermodynamically stable i-alloys, $Al_{65}Cu_{20}Ru_{15}$,[82] $Al_{65}Cu_{20}Fe_{15}$,[74] and $Al_{70}Pd_{20}Mn_{10}$,[10] two common characteristics stand out (Fig. 4.24). First, the Cu $3d$- and Pd $4d$-derived features are pushed away from E_F in comparison to their locations in pure Cu and Pd metals, whereas the features associated with the Os $5d$-, Ru $4d$-, Fe $3d$-, and Mn $3d$-derived states remain close to E_F. Thus one would expect a relatively small contri-

bution to the DOS at E_F from the Cu $3d$- and Pd $4d$-like states and a non-negligible, although also small, contribution due to the Os $5d$-, Ru $4d$-, Fe $3d$-, and Mn $3d$-like states (Fig. 4.24). It should be pointed out that this arrangement of the two features seems reasonable in that Cu and Pd have a full subshell, whereas Os, Ru, Fe, and Mn have a nearly-half-full subshell of the d electrons. This favors the hybridization between the Al sp, TM s electrons and the d electrons in the nearly-half-full subshell. Second, there is a strong reduction of the PES intensity as the E_B approaches E_F. The decrease of intensity as the E_B approaches E_F has been interpreted as evidence for the opening

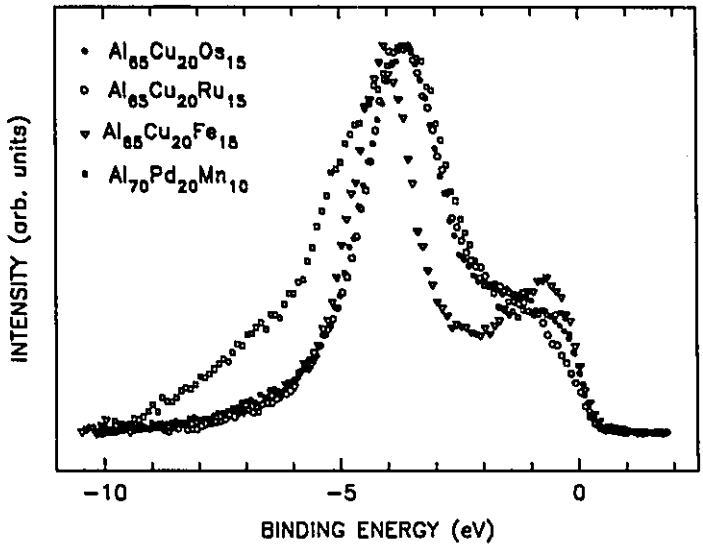

Figure 4.24: **Valence bands of i-alloys $Al_{65}Cu_{20}Os_{15}$ (•),[5] subshell of $Al_{65}Cu_{20}Ru_{15}$ (○),[82] $Al_{65}Cu_{20}Fe_{15}$ (▽),[74] and $Al_{70}Pd_{20}Mn_{10}$ (□)[10] measured respectively at $h\nu$=80, 90, 100 and 100 eV. The raw data of $Al_{65}Cu_{20}Fe_{15}$[74] has been corrected for the energy dependence of the electron transmission of the electron-energy analyzer, normalized for the photon flux, and corrected for the secondary-electron background. The spectra were normalized to give a constant height between the maximum and minimum recorded count.**

of a theoretically-predicted[57–59] pseudogap at E_F. A discussion of the critical issues of the physics of QC's, which is associated with a pseudogap, spikiness, and the high

resistivity behavior, is presented in the following subsections.

4.4.3 Instrumental resolution and a pseudogap

As mentioned before, the decrease of intensity is indicative of a possible opening of a pseudogap at E_F. Such an interpretation of the medium resolution spectroscopic measurements, however, is open to criticism because, as noted earlier,[10, 68, 82] there is an alternate interpretation which would lead to the intensity decrease as the energy approaches E_F. It invokes a simple Fermi cut-off, which would be especially important for the QC's with TM elements whose d-states, as was demonstrated before, contribute to the measured intensity around E_F. In the case of the studied alloys, the d-derived states do contribute to the measured intensity at E_F (Figs. 4.17, 4.18, and 4.24). It can be only concluded that the medium resolution PES results presented so far in the literature are indicative of a possible opening of a pseudogap at E_F, but they do not prove its existence.

The PES experiments performed so far on QC's had an energy resolution, which is dependent on the $h\nu$ used,[5] between 0.3 and 0.7 eV, with the exception of one PES study conducted with the energy resolution 0.233 eV.[67] The only IPES study reported so far had an energy resolution of 0.7 eV.[68] The SXE and SXA studies previously reported had an energy resolution, which is dependent on the element considered, in the range 0.2-0.7 eV, and a relatively high uncertainty of 0.1-0.3 eV associated with the determination of the position of E_F. It was suggested[5] that these energy resolutions are not high enough, and in the case of the SXE/SXA studies, the uncertainty in determining the location of E_F was too large and the lifetime broadening effects too severe, to warrant the claims of a definite spectroscopic verification of the existence of a pseudogap at E_F. Therefore the high energy-resolution PES/IPES and/or SXE/SXA experiments are essential for obtaining convincing experimental evidence for the possible existence of

such a pseudogap.

The interpretation of the low energy-resolution spectroscopic data[49, 66–70, 72, 73, 75–78] almost exclusively in terms of the Hume-Rothery mechanism is unfounded.[5] Only the high energy-resolution PES experiments, as shown in §4.3 and in Refs. [61, 84], can verify unambiguously the possible existence of a pseudogap around E_F in QC's. It can be added here that high energy-resolution PES measurements were instrumental in the *direct* observation of the superconducting gap in high-T_c superconductors,[120, 121] the pseudogap in the charge-density-wave systems,[120, 121] the structure-induced pseudogap in liquid and amorphous alloys,[79] the pseudogap in some fullerens,[145] and the metal-insulator transitions in some inorganic compounds.[121] Naturally, the most credible evidence for the possible existence of a pseudogap at E_F in QC's could be obtained by combining the high energy-resolution of PES with that of IPES.[5]

As shown in §4.3, the ultrahigh energy-resolution UPS experiments[84, 146] provide a direct experimental proof that there is a wide pseudogap from the d-electrons in the vicinity of E_F, which must be then partially responsible for the observed high values of ρ.[61] All known QC's, except the i-Al-Pd-Re system, are metallic as evidenced by a clearly developed Fermi edge. The lack of the Fermi edge in the i-Al-Pd-Re system is consistent with its insulator behavior at low temperatures.[21–23, 61] The possible reasons for the absence of the predicted spikiness of DOS are discussed in §4.4.4.

4.4.4 Broadening effects and spikiness

It was mentioned in Chapter 1 that the predicted pseudogap around E_F in QC's is a generic, but not a specific property distinguishing QC's from the periodic or aperiodic materials.[5] The property which seems to be specific only to QC's is the spikiness of their DOS (Figs. 4.10 and 4.25).[5, 53, 57–60] This spikiness is associated with a large number of non-degenerated flat bands in QC's and the presence of TM elements in QC's

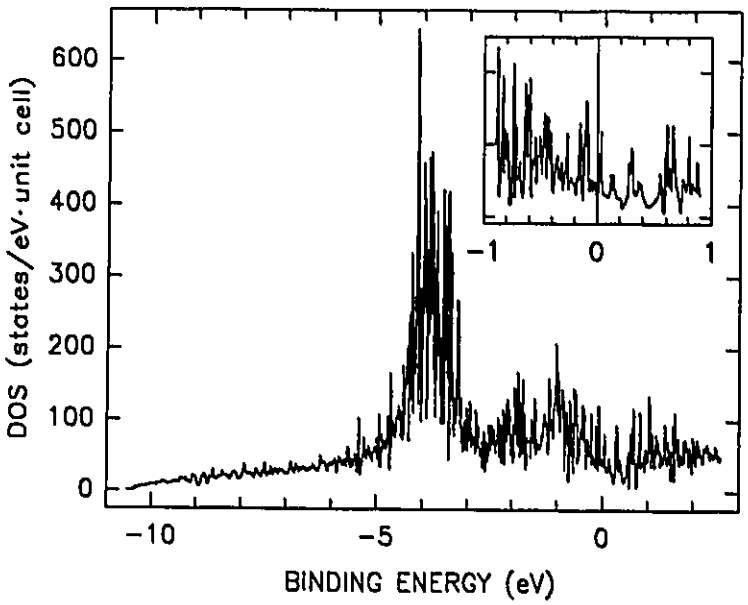

Figure 4.25: **Theoretical $h\nu$=100 eV PES valence band of an *i*-Al-Cu-Fe alloy obtained by summing the theoretical Al, Cu, and Fe PDOS's associated with different angular momenta from Ref. [53] weighted by the corresponding σ values and by the composition and the numbers of the electrons.**

results in its amplification.[5, 53] The width of a spiky peak is of the order of 0.01-0.02 eV (Figs. 4.10 and 4.25).[53, 57–60] The valence bands of *i*-alloys presented here, including the UPS bands measured with an energy resolution of 10 meV, show no evidence for the presence of such spikes. These spikes have also not been detected in the PES, IPES, SXE, or SXA experiments performed so far.[10, 49, 63–70, 72–74, 76–78, 82, 138] There are at least two possible explanations for the failure to detect those spikes experimentally:[5] the lifetime broadening effects associated with the experimental techniques and disorder in QC's.

As discussed in §3.6, the spikiness is smeared out completely for typical PES/IPES and SXE/SXA energy resolutions. This spikiness is expected to be preserved, but only in the vicinity of E_F, for energy resolutions better than 0.1 eV (§3.6). Near E_F, PES and IPES are certainly the only experimental techniques with a resolution not affected

by lifetime broadening which can detect such spikiness.

The second explanation invokes the possibility of chemical and topological disorder in QC's of high structural quality, which will be discussed in the next section. Such a disorder can wash out the spikiness of DOS induced by quasiperiodicity.

It can be concluded that high energy-resolution(<0.1 eV) spectroscopic experiments are indispensable for the direct and unambiguous detection of the theoretically predicted pseudogap around E_F and the spikiness of DOS in QC's. The high resolution UPS spectra in the close-E_F region performed so far do not give any evidence for the existence of the spikiness. One can wonder whether such spikiness does exist at all; perhaps, the spikiness is an artifact resulting from calculations carried out for small clusters of atoms.

4.4.5 Disorder and electronic structure

As mentioned in Chapter 1, there seems to be a contradiction between the fact that stable, "perfect"(no phason strain) QC's have a high degree of structural perfection and the apparent relevance of the quantum interference theories in explaining the temperature and field dependence of ρ.[5] A plausible explanation of this apparent contradiction was suggested,[5] which may also be relevant to the problem of the experimental observation of DOS spikiness. This suggestion deals with two kinds of disorder in QC's: chemical disorder and topological disorder.[5]

The chemical disorder is related to the chemical composition of the QC's. There are at present 22 known stable QC's:[5] 14 *i*-systems Al-Cu-Li, Mg-Ga-Zn, Al-Cu-(Fe,Ru,Os), Al-Pd-(Mn,Re), and the recently discovered Al-Pd-Mg[147] and Zn-Mg-RE (RE=Y, Gd, Tb, Dy, Ho and Er),[148] and 8 decagonal systems Al-Co-(Cu,Ni), Al-Pd-Mn, Al-Rh-(Cu,Ni), and Al-Pd-(Fe,Ru,Os). They are all ternary alloys and 15 of them are based on aluminum. If one envisages that their structure consists of an *sp*-electron-type sublattice and a *d*-electron-type sublattice, then clearly one expects the presence of chemical

disorder in these sublattices (for example, in the CuFe, CuRu, ZCuOs, PdMn, PdRe sublattice).[5]

The topological disorder results from the nature of QC's. The concept of quasiperiodicity implies that no two crystallographic positions of a given atom are exactly the same.[149] This can be viewed as a sort of topological disorder.[5]

Although these two types of disorder are not seen in the diffraction and electron microscopy experiments on stable QC's, they are clearly detected, but not separated, in other experiments which are more sensitive to the presence of such disorder.[5] For example, local probes such as Mössbauer spectroscopy[150] and NMR[151] clearly detect the presence of a distribution of quadrupole splittings in high-quality stable *i*-alloys.[5] Such a distribution can only exist if there is a chemical and/or topological disorder in the investigated samples.[5] Also the NMR parameters, the Knight shift and the spin-lattice relaxation rate, indicate the presence of some disorder modes.[5, 151] A recent study on the propagation of acoustic shear waves in a single-grain *i*-Al-Pd-Mn alloy shows the similarity of the acoustic properties of this alloy to those of amorphous metals.[152] The results of these experiments[150–152] demonstrate that chemical and/or topological disorder is present also in the high-quality, phason-free, stable *i*-alloys and therefore the disorder must be taken into account in attempts to understand the physical properties of QC's. In particular, this disorder may explain why quantum interference theories are successful in explaining some of the electronic transport properties of stable QC's.[5] This disorder may also wash out the DOS spikiness predicted by the calculations which are performed for ideal, disorder-free systems.[5]

4.4.6 Resistivity of quasicrystals

As discussed before, one of the most unusual properties in the QC's is that they have the unexpected high ρ values in comparison to their component metals. There are

experimental arguments which indicate that the Hume-Rothery mechanism alone is not sufficient to explain the high values of ρ.[61] The dramatic changes of ρ (up to two orders of magnitude) with composition[13, 14, 18, 20–23, 153, 154] and structural quality[4, 13, 14, 21–23, 155] have been observed for the i-samples whose values of γ differ only by up to about 10%. For example, the values of ρ (at 2 K) and γ for i-$Al_{69}Pd_{19}Re_{12}$ are respectively 0.1 Ωcm and 0.28 mJ/molK^2 (Ref. [154]). The corresponding values for i-$Al_{67}Pd_{23}Re_{10}$ are 1 Ωcm and 0.25 mJ/molK^2 (Ref. [154]). As both $1/\rho$ in the Einstein equation and γ are proportional to $N(E_F)$, the above experimental fact indicates that the big values of ρ cannot be associated only with the minimum of $DOS(E_F)$. Additionally, the Einstein equation assumes that $1/\rho$ is proportional to the electron scattering time, which implies that ρ should decrease by removing the defects. The opposite is observed for i-alloys.[3, 4, 20–23, 155] This proportionality also predicts that ρ should increase with increasing temperature, which is contrary to the observed steep decrease of ρ with temperature well above the Debye temperature.[13, 14, 21–23] Since $1/\rho$ in the Einstein equation is proportional to the product $DN(F_E)$, the unusually large values of ρ may also originate from the reduced D.[61]

The arguments presented above suggest that a simple interpretation based on the Einstein equation is not applicable to i-alloys and therefore alternative approaches are required to explain the unusual properties of these alloys. These new approaches are based on the concepts of tunneling, localization, and critical states.[61] One of the first of such approaches, which is very qualitative and which claims to give a good explanation of the electronic properties of i-alloys, is based on an internal structural model.[55] It assumes the presence of the conductive i-blocks which are enveloped by an insulating layered-structure network.[55] For this structural model the electrical conduction should occur via tunneling. Such tunneling, however, should lead to deviations from Ohm's law which was shown to be perfectly obeyed in the i-Al-Cu-Fe film for bias voltages varying by seven orders of magnitude.[156] Another approach invokes the concept

of localization.[24] Inherent to this concept is the notion of disorder which causes the electrons to become localized, i.e., spatially confined to some region of an i-alloy.[24, 61] Conduction then occurs via thermal activation between the localized states (hopping). Consequently, the very large values of ρ can occur for the finite values of DOS(E_F). The use of this localization approach to explain the electronic transport properties of i-alloys was suggested by Kimura et al.[157] and was later invoked and elaborated in the following works.[21-23, 158] The third approach is based upon the idea of the new type of the electronic states, the so-called critical states, which are intermediate between the extended electronic states in metals and the localized electronic states in insulators.[61] Such states were shown theoretically to exist in one- and two-dimensional quasiperiodic systems.[159] Although it is not clear whether the critical states can occur in realistic three-dimensional quasiperiodic systems, they may have profound consequences on the electronic transport properties of QC's.[13, 14, 160, 161] It can be concluded that there is no generally accepted explanation of the unusual transport properties of QC's and that it is still unclear to what extent can these properties be associated with the quasiperiodicity.

Chapter 5

CONCLUSIONS

Methodologies of XRD pattern indexing and PES data analysis, as one of the two major parts of the thesis, were developed. Three programs were written for the most-often-used schemes for indexing the *i*- and *d*-structures. The XRD indexing results showed that the studied samples are predominantly single phases. After the corrections for the experimental parameters and background, the PES spectra can be compared not only with respect to their shapes but also in terms of their intensities. This is especially important in analyzing the synchrotron-radiation-based PES data. Study of the electronic structure of QC's is the other major part and constitutes the main purpose of this thesis. Three topics were studied: PDOS and total DOS, pseudogap, and spikiness.

Resonance photoemission effect was employed in establishing the features originated from the *d*-states in the nearly-half-full subshell in the PES valence bands. The positions of the maximum suppression due to the resonance for *i*-Al-Pd-Mn, *d*-Al-Co-Cu, *i*-Al-Cu-Ru, and *i*-Al-Cu-Os alloys were found to be at $E_B \approx -0.64$, -0.8, -1.3, and -1.7 eV, respectively. Because these features are very close to the E_F, they must be, at least partially, responsible to the stability and the unusual resistivity behavior of the studied

QC's. The d electrons in the full subshells (Cu-3d and Pd-4d) were found to be shifted farther away from the E_F. This arrangement must favor the hybridization between the Al sp, TM s electrons and the d electrons of these nearly-half-full subshells. By taking advantage of the synchrotron-radiation-based PES technique, the experimental PDOS's and total DOS of the d-electrons in some cases have been obtained. The PDOS's and the theoretical results were thus compared, whenever the latter were available, and relatively good agreement was observed.

It was shown that the spectroscopic measurements (XPS, PES, SXE, SXA, IPES) performed so far by various groups did not have sufficiently-high-energy resolution to unambiguously solve the problem of the possible pseudogap in the DOS near the E_F. It was demonstrated in this thesis that by using the low-temperature and ultrahigh resolution UPS technique on the sample of i-$Al_{65}Cu_{20}Fe_{7.5}Ru_{7.5}$ alloy, the pseudogap can be ambiguously observed. Fitting of the gap to a Lorentzian dip centered at E_F gives its FWHM=0.33 eV and the depth C=45%. This spectrum also shows that this i-alloy is metallic, as evidenced by a clearly developed Fermi edge. The same conclusion could be reached for all other QC's studied by the UPS technique, except the i-Al-Pd-Re system which does not have a clear Fermi edge and its DOS(E_F) is nearly zero, which is consistent with its insulating behavior at low temperatures.

These UPS experiments also conclusively showed that there are no spikes in the DOS of QC's predicted by theory, although the spikiness is believed to be a *specific* property of QC's in distinguishing the quasiperiodic from the periodic or aperiodic phases. It was suggested that disorder, which is not included in theoretical calculations, may be responsible for the absence of the spikiness. The predicted spikiness may be an artifact resulting from the fact that the numbers of atoms used in the calculations were too small.

It was argued that the low DOS(E_F) is only one of several factors responsible for the high values of ρ. Another one, which may be more important, is the structural nature

of the QC's. This can likely be interpreted using two models which are associated with the localization effects whose relevance confirms the importance of disorder in QC's and with the critical states. The knowledge and understanding of the electronic structure of QC's is indispensable to explain the unusual behavior of ρ and other properties of QC's and it deserves further investigations both theoretically and experimentally.

Appendix A

HUME–ROTHERY THEORY

This appendix presents the basic Hume-Rothery theory with regard to the stability of solids[41] and its theoretical prediction of the minimum of the density of states at the Fermi level.[42]

According to Hume-Rothery's observation, three factors are important in determining the formation of a solid solution and the equilibrium diagram of phases: the atomic size-factor, the electronegative effect, and the relative valence effect. The first factor states that where the atomic diameters of solvent and solute differ by more than about 15% of that of the solvent, the "*size-factor*" is unfavourable and the solid solution is very restricted. When the atomic diameters are within this limit, the size-factor is favourable and a considerable range of solid solutions may be formed. The second factor indicates that the more electronegative the solute element, and the more electropositive the solvent (or *vice versa*), the greater is the tendency for the formation of stable intermediate compounds. The last factor states that when other things are equal, a metal of lower valency is regarded as more likely to dissolve one of higher valency than *vice versa*.

Hume-Rothery suggested that certain electron-atom ratios (e/a) tend to be characteristic of the $\beta, \gamma,$ and ϵ phases in many related systems. The ratio e/a is defined as

the sum over valences weighted by the composition and divided by the total number of atoms. For example, Table A.1 shows the e/a and the chemical formulas for the Cu-Zn system.[162]

Table A.1: **e/a and chemical formula of the Cu-Zn system.**

Phase	β	γ	ϵ
Suggested chemical formula	CuZn	Cu_5Zn_8	$CuZn_3$
e/a	3/2	21/13	7/4

Very often the valences are assumed to be the number of electrons in excess of the last completed shell, as shown in Table A.2.[162] These phases are sometimes called electron phases or Hume-Rothery compounds.

Table A.2: **Valences of the elements in the Hume-Rothery model.**

Valence	Element	Group
1	Cu, Ag, Au	I
2	Be, Mg, Zn, Cd, Hg	II
3	Ga, Al, In	III
4	Si, Ge, Sn, Pb	IV
5	P, AS, Sb Bi V)	V
0	Fe, Co, Ni, Ru, Rh, Pb, Pt, Ir, Os	VIII

Mott and Jones demonstrated[42] that at these critical e/a ratios, the Fermi sphere just touches a Brillouin zone plane, i.e. one has $2k_F=|\mathbf{Q}|$, where $\mathbf{Q}$ is a vector of the reciprocal lattice corresponding to the strongest Bragg peak. In this case an energy gap opens at the Fermi surface, giving rise to a minimum in the DOS and to a lowering of the total electronic energy.[163]

Bibliography

[1] C. Janot, *Quasicrystals: A Primer* (Oxford Univ., New York, 1992).

[2] *Aperiodic '94, Proc. Int. Conf. Aperiodic Crystals*, edited by G. Chapuis and W. Paciorek (World Scientific, Singapore, 1995).

[3] S. Takeuchi, Mater. Sci. Forum **150-151**, 35 (1994), and references therein.

[4] S.J. Poon, Adv. Phys. **41**, 303 (1992), and references therein.

[5] G.W. Zhang, Z.M. Stadnik, A.-P. Tsai, A. Inoue, and T. Miyazaki, Z. Phys. B **97**, 439 (1995), and references therein; Z.M. Stadnik, G.W. Zhang, A.-P. Tsai, and A. Inoue, in Ref. [2], p. 249.

[6] R.C. O'Handley, R.A. Dunlap, and M.E. McHenry, in *Handbook of Magnetic Materials*, edited by K.H.J. Buschow (Elsevier, Amsterdam, 1991), Vol. 6, p. 453.

[7] Z.M. Stadnik and G. Stroink, Phys. Rev. B **43**, 894 (1991); **44**, 4255 (1991).

[8] *Quasicrystals*, edited by T. Fujiwara and T. Ogawa (Springer-Verlag, Berlin, 1990).

[9] *Quasicrystals, The State of the Art*, edited by D.P. DiVincenzo and P.J. Steinhardt (World Scientific, Singapore, 1991).

[10] G.W. Zhang, Z.M. Stadnik, A.-P. Tsai, and A. Inoue, Phys. Rev. B **50**, 6696 (1994), and references therein; Phys. Lett. A **186**, 345 (1994).

[11] T. Klein, C. Berger, G. Fourcaudot, J.C. Grieco, and F. Cyrot-Lackmann, J. Non-Cryst. Solids **156-158**, 901 (1993).

[12] P. Lindqvist, C. Berger, T. Klein, P. Lanco, F. Cyrot-Lackmann, and Y. Calvayrac, Phys. Rev. B **48**, 630 (1993).

[13] F.S. Pierce, P.A. Bancel, B.D. Biggs, Q. Guo, and S.J. Poon, Phys. Rev. **47**, 5670 (1993).

[14] D. Mayou, C. Berger, F. Cyrot-Lackmann, T. Klein, and P. Lanco, Phys. Rev. Lett. **70**, 3915 (1993).

[15] M.A. Chernikov, A. Bernasconi, C. Beeli, and H.R. Ott, Europhys. Lett. **21**, 767 (1993).

[16] H. Akiyama, T. Hashimoto, T. Shibuya, K. Edagawa, and S. Takeuchi, J. Phys. Soc. Jpn. **62**, 639 (1993).

[17] P. Lanco, T. Klein, C. Berger, F. Cyroy-Lackmann, G. Fourcaudot, and A. Sulpice, Europhys. Lett. **18**, 227 (1992); P. Lanco, C. Berger, F. Cyroy-Lackmann, G. Fourcaudot, and A. Sulpice, J. Non-Cryst. Solids **153-154**, 325 (1993).

[18] B.D. Biggs, S.J. Poon, and N.R. Munirathnam, Phys. Rev. Lett. **65**, 2700 (1990).

[19] H. Akiyama, Y. Honda, T. Hashimoto, K. Edagawa, and A. Takeuchi, Jpn. J. Appl. Phys. B **7**, L1003 (1993).

[20] Y. Honda, K. Edagawa, A. Yoshika, T. Hashimoto, and S. Takeuchi, Jpn. J. Appl. Phys. A **9**, 4929 (1994).

[21] F.S. Pierce, S.J. Poon, and Q. Guo, Science **261**, 737 (1993).

[22] C. Berger, T. Grenet, P. Lindqvist, P. Lanco, J.C. Grieco, G. Fourcaudot and F. Cyrot-Lackmann, Solid State Commun. **87**, 977 (1993).

[23] F.S. Pierce, Q. Guo, and S.J. Poon, Phys. Rev. Lett. **73**, 2220 (1994).

[24] N. Mott, *Conduction in Non-Crystalline Materials* (Clarendon, Oxford, 1993).

[25] S. Matsuo, T. Ishimasa, H. Nakano, and Y. Fukano, J. Phys. F **18**, L175 (1988); Z.M. Stadnik, G. Stroink, H. Ma, and G. Williams, Phys. Rev. B **39**, 9797 (1989).

[26] T. Klein, C. Berger, D. Mayou, and F. Cyrot-Lackmann, Phys. Rev. Lett. **66**, 2907 (1991).

[27] L.X. He, Y.K. Wu, and K.H. Kuo, J. Mater. Sci. Lett. **7**, 1284 (1988).

[28] A.-P. Tsai, A. Inoue, and T. Masumoto, Mater. Trans. Jpn. Inst. Met. **30**, 300 (1989); *ibid.* **30**, 463 (1989); A.R. Kortan, F.A. Thiel, H.S. Chen, A.P. Tsai, A. Inoue, and T. Masumoto, Phys. Rev. B **40**, 9397 (1989).

[29] W. Steurer, Mater. Sci. Forum **150-151**, 15 (1994), and references therein.

[30] L. Shu-yuan, W. Xue-mei, L. Li, Z. Dian-lin, L.X. He, and K.X. Kuo, Phys. Rev. B **41**, 9625 (1990).

[31] T. Shibuya, T. Hashimoto, and S. Takeuchi, J. Phys. Soc. Jpn. **59**, 1917 (1990).

[32] S. Martin, A.F. Hebard, A.R. Kortan, and F.A. Thiel, Phys. Rev. Lett. **67**, 719 (1991).

[33] S. Takeuchi, H. Akiyama, N. Naito, T. Shibuya, T. Hashimoto, K. Edagawa, and K. Kimura, J. Non-Cryst. Solids **153-154**, 353 (1993).

[34] W. Yun-ping, L. Li, and Z. Dian-Lin, J. Non-Cryst. Solids **153-154**, 361 (1993).

[35] W. Yun-ping and Z. Dian-lin, Phys. Rev. B 49, 13204 (1994).

[36] Z. Dian-lin, L. Li, W. Xue-mei, L. Shu-yuan, L.X. He, and K.H. Kuo, Phys. Rev. B 41, 8557 (1990).

[37] W. Yun-ping, Z. Dian-lin, and L.F. Chen, Phys. Rev. B 48, 10542 (1993).

[38] Z. Dian-lin, C. Shao-chun, W. Yun-ping, L. Li, W. Xue-mei, X.L. Ma, and K.H. Kuo, Phys. Rev. Lett. 66, 2778 (1991).

[39] D.N. Basov, T. Timusk, F. Barakat, J. Greedan, and B. Gruschko, Phys. Rev. Lett. 72, 1937 (1994).

[40] R. Lück and S. Kek, J. Non-Cryst. Solids 153-154, 329 (1993).

[41] W. Hume-Rothery, J. Inst. Metals 35, 295 (1926); W. Hume-Rothery and G.V.Raynor, *The Structure of Metals and Alloys, Institute of Metals: Monograph and Report Series No. 1* (Richard Clary and Company, London, 1956).

[42] N.F. Mott and H. Jones, *The Theory of the Properties of Metals and Alloys* (Oxford University, Glasgow, 1958).

[43] A.P. Bancel and P.A. Heiney, Phys. Rev. B 33, 7917 (1986);.

[44] A.-P. Tsai, A. Inoue, and T. Nasumoto, Mater. Trans. Jpn. Inst. Metals 30, 666 (1989).

[45] J. Friedel and F. Dénoyer, C. R. Acad. Sci. (Paris) 305, 171 (1987); J. Friedel, Helv. Phys. Acta 61, 538 (1988).

[46] K. Kimura, H. Iwahashi, T. Hashimoto, S. Takeuchi, U. Mizutani, S. Ohashi, and G. Itoh, J. Phys. Soc. Jpn. 58, 2472 (1989); J.L. Wagner, B.D. Biggs, and B. Dubost, Phys. Rev. Lett. 65, 203 (1990).

[47] F. Hippert, L. Kandel, Y. Calvayrac, and B. Dubost, Phys. Rev. Lett. 69, 2086 (1992).

[48] S.E. Burkov, T. Timusk, and N.W. Ashcroft, J. Phys.: Condens. Matter 4, 9447 (1992); L. Degiorgi, M.A. Chernikov, C. Beeli, and H.R. Ott, Solid State Commun. 87, 721 (1993).

[49] E. Belin, Z. Dankházi, and A. Sadoc, Mater. Sci. Eng. A 181-182, 717 (1994), and references therein.

[50] T. Klein, O.G. Symko, D.N. Davydov, and A.G.M. Jansen, Phys. Rev. Lett. 74, 3656 (1995).

[51] M.A. Fradkin, J. Phys.: Condens. Matter 4, 10497 (1992).

[52] M. Windisch, M. Krajčí, and J. Hafner, J. Phys.: Condens. Matter 6, 6977 (1994), and references therein.

[53] G. Trambly De Laissardière and T. Fujiwara, Phys. Rev. B **50**, 5999 (1994), and references therein.

[54] M. Krajčí, M. Windisch, and J. Hafner, J. Non-Cryst. Solids, in press.

[55] J.C. Phillips, Phys. Rev. B **47**, 7747 (1993).

[56] V. Heine, D. Weaire, in *Solid State Physics. Advances in Research and Applications*, edited by H. Ehrenreich, F. Seitz, and D. Turnbull (Academic, New York, London, 1970), Vol. 24, p. 249; A. Cottrell, *Introduction to the Modern theory of Metals* (The Institute of Metals, London, 1988).

[57] J. Hafner and M. Krajčí, Phys. Rev. B **47**, 1179 (1993).

[58] T. Fujiwara, Phys. Rev. B **40**, 942 (1989); J. Non-Cryst. Solids **117-118**, 844 (1990); T. Fujiwara and Tsunetsugu, in Ref. [9], p. 343; T. Fujiwara and T. Yokokawa, Phys. Rev. Lett. **66**, 333 (1991); T. Fujiwara, J. Non-Cryst. Solids **156-158**, 865 (1993).

[59] J. Hafner and M. Krajčí, *ibid.* **68**, 2321 (1992); Europhys. Lett. **17**, 145 (1992); J. Nin-Cryst. Solids **150**, 337 (1992).

[60] T. Fujiwara, S. Yamamoto, and G. Trambly De Laissardière, Phys. Rev. Lett. **71**, 4166 (1993); T. Fujiwara, Mater. Sci. Eng. B **19**, 77 (1993).

[61] Z.M. Stadnik, in *Mössbauer Spectroscopy Applied to Magnetism and Materials Science*, edited by G.J. Long and F. Grandjean, (Plenum, New York), Vol. 2, to appear.

[62] J.C. Phillips and K.M. Rabe, Phys. Rev. Lett. **66**, 923 (1991); J.C. Phillips, Solid State Commun. **83**, 379 (1992); Phys. Rev. B **47**, 2522 (1993).

[63] P.A. Bruhwiler, Y. Shen, S.E. Schnatterly, and S.J. Poon, Phys. Rev. **36**, 7347 (1987); P.A. Bruhwiler, J.L. Wabner, B.D. Biggs, Y. Shen, K.M. Wong, S.E. Schnatterly, and S.J. Poon, Phys. Rev. **37**, 6529 (1988).

[64] D.L. Ederer, R. Schaefer, K.-L. Tsang, C.H. Zhang, T.A. Caliicott, and E.T. Arakawa, Phys. Rev. B **37**, 8594 (1988).

[65] A. Traverse, L. Dumoulin, and E. Belin in *Quasicrystalline Materials*, edited by Ch. Janot and J.M. Dubois (World Scientific, Singapore, 1988), p. 399.

[66] E. Belin and A. Traverse, J. Phys.: Condens. Matter **3**, 2157 (1991).

[67] M. Mori, S. Matsuo, T. Ishimasa, T. Matsuura, K. Kamiya, K. Kimura, H. Inohuchi, and T. Matsukawa, J. Phys.: Condens. Matter **3**, 767 (1991).

[68] H. Matsubara, S. Ogawa, T. Kinoshita, K. Kishi, S. Takeuchi, K. Kimura, and S. Suga, Jpn. J. Appl. Phys. A **30**, L389 (1991).

[69] E. Belin, J. Kojnok, A. Sadoc, A. Traverse, M. Harmelin, C. Berger, and J.M. Bubois, J. Phys.: Condens. Matter **4**, 1057 (1992).

[70] E. Belin, Z. Dankházi, A. Sadoc, Y. Calvayrac, T. Klein, and J.M. Bubois, J. Phys.: Condens. Matter **4**, 4459 (1992).

[71] E. Belin, in *Physics and Chemistry of Finite Systems*, edited by P. Jena, S.N. Khanna, and B.K. Rao (Kluwer, Amsterdam, 1992), Vol. II, p. 829.

[72] E. Belin, Z. Dankházi, A. Sadoc, and J.M. Bubois, J. Phys.: Condens. Matter **6**, 8771 (1994).

[73] E. Belin and Z. Dankházi, J. Non-Cryst. Solids **153-154**, 298 (1993).

[74] Z.M. Stadnik and G. Stroink, Phys. Rev. B **47**, 100 (1993).

[75] U. Mizutani, T. Matsuda, Y. Itoh, K. Tanaka, H. Domae, T. Mizuno, S. Murasaki, Y. Miyoshi, K. Hashimoto, and Y. Yamada, J. Non-Cryst. Solids **156-158**, 882 (1993).

[76] E. Belin, Y. Miyoshi, Y. Ishikawa, T. Matsuda, and U. Mizutani, Mater. Sci. Eng. A **181-182**, 730 (1994).

[77] Y. Nakamura, U. Mizutani, Mater. Sci. Eng. A **181-182**, 790 (1994).

[78] K. Hashimoto, Y. Yamada, T. Yamauchi, T. Tanaka, T. Matsuda, and U. Mizutani, Mater. Sci. Eng. **181-182**, 785 (1994).

[79] P. Häussler, Phys. Rep. **222**, 65 (1992).

[80] M.E. McHenry, M.E. Eberhart, R.C. O'Handley, and K.H. Johnson, Phys. Rev. Lett. **56**, 81 (1992).

[81] V. De Coulon, F.A. Reuse, and S.N. Khanna, Phys. Rev. B **48**, 814 (1993); F. Liu, S.N. Khanna, L. Magaud, P. Jena, V. De Coulon, X.-G. He, and F. Cyrot-Lackmann, Phys. Rev. B **48**, 1295 (1993).

[82] Z.M. Stadnik, G.W. Zhang, A.-P. Tsai, and A. Inoue, Phys. Rev. B **51**, 4023 (1995), and references wherein; J. Phys.: Condens. Matter **6**, 6885 (1994).

[83] Z.M. Stadnik, G.W. Zhang, A.-P. Tsai, and A. Inoue, Phys. Rev. B **51**, 11358 (1995); Phys. Lett. A **198**, 237, (1995); in Ref. [2], p. 254.

[84] Z.M. Stadnik, G.W. Zhang, D. Purdy, M. Garnier, Y. Baer, A.-P. Tsai, and A. Inoue, unpublished results.

[85] Z.M. Stadnik and G.W. Zhang, Int. J. Mod. Phys., in press.

[86] G.W. Zhang and Z.M. Stadnik, Int. J. Mod. Phys., in press.

[87] Z.M. Stadnik and F. Müller, Philos. Mag. B **71**, 221 (1995).

[88] A.-P. Tsai, A. Inoue, and T. Masumoto, Jpn. J. Appl. Phys. **26**, L1505 (1987); **27**, L1587 (1988).

[89] R. Jenkins and W.N. Schreiner, Powder Diffr. **4**, 74 (1989).

[90] Standard Reference Material 640b, Silicon Powder 2Θ/d-Spacing for X-Ray Diffraction, Natl. Bur. Stand. (U.S.), edited by S.D. Rasberry (U.S. GPO, Gaithersburg, 1987).

[91] W.N. Schreiner and R. Jenkins, Adv. X-ray Anal. **26**, 141 (1983).

[92] W. Wong-Ng and C.R. Hubbard, Powder Diffr. **2**, 242 (1987).

[93] G.W. Zhang, Index.for, D1index.for, and D2index.for in *Three Fortran Programs for Indexing XRD Patterns of the QC's* (University of Ottawa, Ottawa, 1994).

[94] C. Kittel, *Introduction to Solid State Physics* (John Wiley & Sons, New York, 1986).

[95] V. Elser, Acta Cryst., A **42**, 36 (1986).

[96] P.A. Bancel, P.A. Heiney, P.W. Stephens, A.I. Goldman, and P.M. Horn, Phys. Rev. Lett. **54**, 2422 (1985).

[97] J.W. Cahn, D. Shechtman, and D. Gratias, J. Mater. Res. **1**, 13 (1986).

[98] A. Yamamoto and K.N. Ishihara, Acta Cryst. A **44**, 707 (1988).

[99] S. Takeuchi and K. Kimura, J. Phys. Soc. Japan **56**, 982 (1987).

[100] J. Devaud-Rzepski, A. Quivy, Y. Calvayrac, M. Cornier-Quiquandon and D. Gratias, Philos. Mag. B **60**, 855 (1989).

[101] C. Dong, J.M. Dubois, M. De Boissieu and C. Janot, J. Phys.: Condens. Matter **3**, 1665 (1991).

[102] M. Grioni, Photoelectron Spectroscopies for Beginners: a Brief Introduction (Institut de Physique, Université de Neuchâtel, Neuchâtel, 1995).

[103] C. Kunz, in *Photoemission in Solids II*, edited by L. Ley and M. Cardona (Springer-Verlag, Berlin, 1979), p. 299.

[104] J.C. Helmer and N.H. Weichert, Appl. Phys. Lett. **13**, 266 (1968).

[105] D.A. Shirley, Phys. Rev. B **5**, 4709 (1972).

[106] M.L. Shek, U14A Survival Guide, in *Operation Notes for Beamline U14A* (Brookhaven Natl. Lab., Yew York, 1993).

[107] L.C. Davis, J. Appl. Phys. **59**, R25 (1986).

[108] J.C. Fuggle and N. Mårtensson, J. Electron Spectr. Rel. Phenom. **21**, 275 (1980).

[109] D.E. Eastman and W.D. Grobman, Phys. Rev. Lett. **28**, 1327 (1972); J. Freeouf, M. Erbudak, and D.E. Eastman, Solid State Commun. **13**, 771 (1973); D.E. Eastman, J. Freeouf, and M. Erbudak, J. Phys. (Paris) Colloq. **34**, C6-37 (1973); P.J. Feibelman and D.E. Eastman, Phys. Rev. B **10**, 4932 (1974).

[110] J.W. Allen, S.J. Oh, O. Gunnarsson, K. Schönhammer, M.B. Maple, M.S. Torikachvili, and I. Lindau, Adv. Phys. **35**, 275 (1986).

[111] G. Trambly De Laissardière and T. Fujiwara, Mater. Sci. Eng. A **181-182**, 722 (1994); Phys. Rev. B **50**, 9843 (1994).

[112] H. Höchst, P. Steiner, G. Reiter, and S. Hüfner, Z. Phys. B **42**, 199 (1981).

[113] D. Pines and P. Noziers, *The Quantum Theory of Liquids* (W.A. Benjamin, New York, 1966), pp. 63 and 309; N.W. Ashcroft and N.D. Mermin, *Solid State Physics* (Saunders College, Philadelphia, 1976), p. 347.

[114] J.-J. Yeh, *Atomic Calculation of Photoionization Cross-Sections and Asymmetry Parameters* (Gordon and Breach, New York, 1993).

[115] A. Goldmann, J. Tejada, N.J. Shevchik, and M. Cardona, Phys. Rev. B **10**, 4388 (1974); J. Tejada, N.J. Shevchik, W. Braun, A. Goldmann, and M. Cardona, *ibid.* **12**, 1557 (1975).

[116] Y. Baer and G. Busch, Phys. Rev. Lett. **30**, 280 (1973).

[117] M.F. López, C. Laubschat, A. Gutiérrez, A. Höhr, M. Domke, G. Kaindl, and M. Abbate, Z. Phys. B **95**, 9 (1994).

[118] R.F. Sabiryanov and S.K. Bose, J. Phys.: Condens. Matter **6**, 6197 (1994).

[119] P. Häussler, in *Glassy Metals III*, edited by H. Beck and H.-J. Güntherodt (Springer-Verlag, Berlin, 1994), p. 163.

[120] Y. Baer and H.P. Myers, Solid State Commun. **21**, 833 (1977); J.-M. Imer, F. Patthey, B. Dardel, W.-D. Schneider, Y. Baer, Y. Petroff, and A. Zettl, Phys. Rev. Lett. **62**, 336 (1989); B. Dardel, M. Grioni, D. Malterre, P. Weibel, Y. Baer, and F. Lévy, J. Phys.: Condens. Matter **5**, 6111 (1993); M. Nakamura, A. Sekiyama, H. Namatame, H. Kino, A. Fujimori, A. Misu, H. Ikoma, M. Matoba, and S. Anzai, Phys. Rev. Lett. **73**, 2891 (1994).

[121] K.E. Smith and V.E. Henrich, Phys. Rev. B **50**, 1382 (1994).

[122] S. Doniach and M. Šunjić, J. Phys. C **3**, 285 (1970).

[123] G.K. Wertheim and P.H. Citrin, in *Photoemission in Solids I*, edited by M. Cardona and L. Ley (Springer-Verlag, Berlin, 1978), p. 197.

[124] Y. Baer, G. Busch, and P. Cohn, Rev. Sci. Instrum. **46**, 466 (1975); S.A. Flodstrom, R.Z. Bachrach, R.S. Bauer, and S.B. Hagström, Phys. Rev. Lett. **37**, 1282 (1976); S.B.M. Hagström, R.Z. Bachrach, R.S. Bauer, and S.A. Flodström, Phys. Scripta **16**, 414 (1977).

[125] F.U. Hillebrecht, J.C. Fuggle, P.A. Bennett, Z. Zolnierek, and Ch. Freiburg, Phys. Rev. B **27**, 2179 (1983).

[126] Z.M. Stadnik and G. Stroink, J. Non-Cryst. Solids **99**, 233 (1988), and references therein.

[127] A.-P. Tsai, A. Inoue, Y. Yokoyama, and T. Masumoto, Mater. Trans. Jpn. Inst. Met. **31**, 98 (1990).

[128] A.-P. Tsai, A. Inoue, and T. Masumoto, Philos. Mag. Lett. **62**, 95 (1990).

[129] A.-P. Tsai, Y. Yokoyama, A. Inoue, and T. Masumoto, J. Mater. Res. **6**, 2646 (1991).

[130] A. Sadoc and J.M. Dubois, J. Non-Cryst. Solids **153-154**, 83 (1993).

[131] C. Beeli, H.-U. Nissen, and J. Robadey, Phil. Mag. Lett. **63**, 87 (1991); M. Audier, M. Durand-Charre, and M. De Boissieu, Philos. Mag. B **68**, 607 (1993).

[132] C. Dong, J.M. Dubois, M. De Boissieu, M. boudard, and C. Janot, J. Mater. Res. **6**, 2637 (1991).

[133] R.J. Lad and V.E. Henrich, Phys. Rev. B **38**, 10860 (1988).

[134] G. Rossi, I. Lindau, L. Braicovich, and I. Abbati, Phys. Rev. B **28**, 3031 (1983), and references therein.

[135] H. Wright, P. Weightman, P.T. Andrews, W. Folkerts, C.F.J. Flipse, G. Sawatzky, D. Norman, and H. Padmore, Phys. Rev. B **35**, 519 (1987).

[136] P. Weightman, M. Davis, and P.T. Andrews, Phys. Rev. B **30**, 5586 (1984).

[137] J.W. Allen, in *Synchrotron Radiation Research: Advances in Surface and Interface Science*, edited by R.Z. Bachrach (Plenum, New York, London, 1992), Vol. 1, p. 253.

[138] E. Belin, Z. Dankházi, and A. Sadoc, J. Non-Cryst. Solids **156-158**, 896 (1993).

[139] J.C. Fuggle, F.U. Hillebrecht, R. Zeller, Z. Zolnierek, P.A. Bennett, and Ch. Freiburg, Phys. Rev. B **27**, 2145 (1983).

[140] C.S. Fadley and D.A. Shirley, in *Electronic Density of States*, Natl. Bur. Stand. (U.S.) Spec. Publ. No. 323, edited by L.H. Bennett (U.S. GPO, Washington, D.C., 1971), p. 163; N.V. Smith, G.K. Wertheim, S. Hüfner, and M.M. Traum, Phys. Rev. B **10**, 3197 (1974); N. Mårtensson, R. Nyholm, H. Calén, J. Hedman, and B. Johansson, *ibid.* **24**, 1725 (1981).

[141] L. Ley, O.B. Dabbousi, S.P. Kowalczyk, F.R. McFeely, and D.A. Shirley, Phys. Rev. B **16**, 5372 (1977); A. Kakizaki, h. Sugawara, I. Nagakura, and T. Ishii, J. Phys. Soc. Jpn. **49**, 2183 (1980); S. Raaen and V. Murgai, Phys. Rev. B **36**, 887 (1987).

[142] A. Sadoc, E. Belin, Z. Dankházi, and A.M. Flank, J. Non-Cryst. Solids **153-154**, 338 (1993).

[143] A.P. Smith and N.W. Ashcroft, Phys. Rev. Lett. **59**, 1365 (1987).

[144] V.G. Vaks, V.V. Kamyshenko, and G.D. Samolyuk, Phys. Lett. A **132**, 131 (1988).

[145] T. Takahashi, Comments Cond. Mat. Phys. **16**, 113 (1992).

[146] Z.M. Stadnik, D. Purdy, M. Garnier, Y. Baer, A.-P. Tsai, and A. Inoue, unpublished results.

[147] N. Koshikawa, S. Sakamoto, K. Edagawa, and S. Takeuchi, Jpn. J. Appl. Phys. **31**, L966 (1992); N. Koshikawa, K. Edagawa, and S. Takeuchi, Mater. Trans. Jpn. Inst. Metals **34**, 188 (1993).

[148] A. Niikura, A.P. Tsai, A. Inoue, and T. Masumoto, Philos. Mag. Lett. **69**, 351 (1994); A.P. Tsai, A. Niikura, A. Inoue, T. Masumoto, Y. Nishida, K. Tsuda and M. Tanaka, Philos. Mag. Lett. **70**, 169 (1994).

[149] Ch. Janot and J.M. Dubois, J. Phys. F **18**, 2303 (1988).

[150] Z.M. Stadnik, Hyperfine Interact. **90**, 215 (1994).

[151] A. Shastri, F. Borsa, A.I. Goldman, J.E. Shield, an dD.R. Torgeson, J. Non-Cryst. Solids **153-154**, 347 (1993).

[152] N. Vernier, G. Bellessa, B. Perrin, A. Zarembovitch, and M. De Boissieu, Europhys. Lett. **22**, 187 (1993).

[153] U. Mizutani, Y. Sakabe, T. Shibuya, K. Kishi, K. Kimura, and S. Takeuchi, J. Phys.: Condens. Matter **2**, 6169 (1990).

[154] T. Takeuchi, Y. Yamada, U. Mizutani, Y. Honda, K. Edagawa, and S. Takeuchi, Int. J. Mod. Phys., in press.

[155] K. Wang, C. Scheidt, P. Garoche, and Y. Calvayrac, J. Phys. I (Paris) **2**, 1553 (1992).

[156] T. Klein and O.G. Symko, Phys. Rev. Lett. **73**, 2248 (1994).

[157] K. Kimura, S. Takeuchi, in Ref.[9], p. 313; K. Kimura, K. Kishi, T. Hashimoto, and S. Takeuchi, in Ref. [8], p. 233.

[158] D.N. Basov, F.S. Pierce, P. Volkov, S.J.Poon, and T. Timusk, Phys. Rev. Lett. **73**, 1865 (1994).

[159] H. Tsunetsugu, T. Fujiwara, K. Ueda, and T. Tokihiro, Phys. Rev. B **43**, 8879 (1991); B. Passaro, C. Sire, and V.G. Benza, *ibid.* **46**, 13751 (1992).

[160] S.J. Poon, F.S. Pierce, and Q. Guo, Phys. Rev. B **51**, 2777 (1995).

[161] N.P. Lalla, R.S. Tiwari, and O.N. Srivastava, J. Phys.: Condens. Matter **7**, 2409 (1995).

[162] C.S. Barrett and T.B. Massalski, *Structure of Metals* (McGraw Hill, New York, 1966).

[163] J. Hafner, S.S. Jaswal, M. Tegze, A. Pflugi, J. Krieg, P. Oelhafen, and H.-J. Güntherodt, J. Phys. F **18**, 2583 (1988).